Development of advanced solar cells - Contribution to the HCSC on InP and to the III-V onto Si monolithic tandem cells

Fei Fan

To cite this version:

Fei Fan. Development of advanced solar cells - Contribution to the HCSC on InP and to the III-V onto Si monolithic tandem cells. Optics / Photonic. INSA de Rennes, 2022. English. NNT : 2022ISAR0008 . tel-04475482

HAL Id: tel-04475482
https://theses.hal.science/tel-04475482

Submitted on 23 Feb 2024

DOCTORAT MATIERE
BRETAGNE MOLECULES
LOIRE ET MATERIAUX

INSA
RENNES

THESE DE DOCTORAT DE

L'INSTITUT NATIONAL DES SCIENCES
APPLIQUEES RENNES

ECOLE DOCTORALE N° 596
Matière, Molécules, Matériaux
Spécialité : « *Photonique* »

Par
Fei FAN

Développement de cellules solaires avancées - Contribution aux cellules à porteurs chauds sur InP et aux cellules tandem monolithiques III-V sur Si

Thèse présentée et soutenue à Rennes, le 21/12/2022
Unité de recherche : Institut FOTON – UMR 6082
Thèse N° : 22ISAR 44 / D22 - 44

Rapporteurs avant soutenance :

Zakaria Djebbour	MCF-HDR GeePs (UMR 8507), Univ. Paris-Saclay, France
Negar Naghavi	Directrice de recherche IPVF-UMR, Palaiseau, France

Composition du Jury :

Président :	**Stéphane Collin**	Directeur de recherche C2N, Palaiseau, France
Examinateurs :	**Zakaria Djebbour**	MCF-HDR GeePs (UMR 8507), Univ. Paris-Saclay, France / Rapporteur
	Negar Naghavi	Directrice de recherche IPVF-UMR, Palaiseau, France / Rapportrice
	Nicolas Barreau	MCF-HDR IMN, Université de Nantes, France

Dir. de thèse :	**Olivier Durand**	Professeur Institut FOTON, INSA-Rennes, France
Co- encadrante. de thèse		
	Soline Boyer-Richard	MCF Institut FOTON, INSA-Rennes, France

Intitulé de la thèse :

Développement de cellules solaires avancées - Contribution aux cellules à porteurs chauds sur InP et aux cellules tandem monolithiques III-V sur Si

Fei FAN

En partenariat avec :

Acknowledgement

This four-year journey as a PhD student in France was quite a special period of my life with enriching experiences. Time flows like water, and the unforgettable journey is about to reach the end. Among all the complex feelings, I would like to express my gratitude to a lot of people. I could not have finished this thesis without their contribution.

First, I would like to express my sincere gratitude to my supervisors, Olivier DURAND and Soline BOYER. I appreciate that they have entrusted me with this thesis. Thanks to their knowledge and expertise, I have always learned something new from them and finally finished my thesis. I would also like to thank them for their kindness and help when I first arrived in France, which allowed me to adapt quickly to this new environment. I'm very grateful for their support, advice, and guidance during the last four years.

I would also like to express my gratitude to the jury members, Zakaria DJEBBOUR, Negar NAGHAVI, Stéphane COLLIN and Nicolas BARREAU, for their constructive remarks and valuable suggestions to improve the quality of the manuscript.

What's more, I would like to thank the ANR (Agence Nationale de La Recherche) for the funding of this project and CSC (China Scholarship Council) for the scholarship.

Besides, I would like to express my appreciation to all my colleagues at FOTON , especially Karine. Thank you for the special birthday cake you made for me personally, and thanks for your son's painting, it's cute!

I also want to thank all my other friends for relieving my stress and bringing joy to my life.

Last but not least, I would like to thank my family for their love and support in my life. I am very grateful that they have always understood and respected my decisions at each period of my study. I feel very lucky to have them as my family.

致谢

春生夏长，秋收冬藏。树终将成树，花终将成花。而我四年的海外求学生涯也即将画满句号。留学法国读博的这四年，将是我毕生难忘的四年。时光如水流泻，旅程即将到达终点，难免感慨良多，而这其中最多的，还是感谢。

桃李不言下自成蹊，感谢我的大导师 Olivier DURAND 教授。幸得教授，受益终生。您对待学术的严谨，对待工作的认真负责，对生活的热爱，对学生和同事的亲切友爱，都将在未来的每一天激励着我。我也要感谢我的小导师 Soline BOYER，感谢您对于我实验与论文的指导，感谢您在这几年的关心与照拂。感谢所有帮助过我的同事和同学，特别是 Karine，谢谢你亲手为我做的生日蛋糕，也谢谢您儿子的画！祝您们平安顺遂，科研顺利。

也要感谢一路陪伴的朋友，感谢陪我快乐、渡我忧伤。此去一别，山水迢迢，路遥马急。愿此去前程似锦，万事胜意，再相逢依旧如故。

我永远臣服于清澈洁白的人格与炽热真诚的灵魂。感谢你，我的人生理想。

特别感谢我的父母和家人，春晖寸草，难以为报。只愿平安康乐，岁月无忧。

最后，我想要感谢不怕困苦、克服万难，依旧不折不挠的自己。

虽无雄才大志，亦愿不负韶华。让我们，鲜衣怒马，前路再相逢！

Table of Content

Introduction 5
Chapter 1 Advanced concepts of solar cells: Tandem Cells and Hot Carrier Solar Cells 9
1.1. Operating principle of a solar cell 9
1.1.1. PN junction 9
1.1.2.Photovoltaic conversion 11
1.1.3. Electrical parameters and quantum efficiency 12
1.1.4. Shockley-Queisser efficiency limit 13
1.2. Multi-junction solar cells 16
1.2.1. Architecture of multi-junction solar cells 16
1.2.2. State of the art of MJSC: efficiency conversion records 17
1.2.3. Tandem cells based on Si bottom cells 19
1.2.3.2. Methods of manufacturing tandem cells on silicon 22
1.2.3.2.a. Wafer bonding 22
1.2.3.2.b. Metamorphic growth 23
1.2.3.2.c. Pseudomorphic growth 23
1.2.4. GaP/Si-based cells (with state of the art of FOTON lab: GaP/Si interface) 24
1.2.4.1. GaP/Si interface 24
1.2.4.2. GaP and GaP/Si-based solar cells 26
1.2.4.2.a. Mono-junction cells 26
1.2.4.2.b. Tandem cells 27
1.2.4.3. Pseudomorphic growth based on Ga(As)PN on GaP/Si 27
1.3. Hot Carrier Solar Cells 31
1.3.1. Principles of the HCSC 31
1.3.2. Thermalisation process 33
1.3.3 State of the art of HCSC 34
References: 37
Chapter 2 Manufacturing, characterization and modeling of solar cells 45
2.1. Manufacturing of GaAsPN/Si tandem solar cells at Institut FOTON 45
2.1.1. MBE growth of GaP-based heterostructures on silicon substrates 45
2.1.1.1. UHV-CVD growth cluster 46

2.1.1.2. MBE frame 47
2.1.2. Manufacture of cell-architectures 49
2.1.2.1. Technological processes for the manufacture of the GaP/Si-based solar cells 49
2.1.2.1.a. Top-Bottom contacts 51
2.1.2.1.b. Top-Top contacts 51
2.2. Manufacturing of Hot carrier Solar Cells on InP substrates at Institut FOTON 53
2.2.1. MBE growth of HCSC on InP substrates 53
2.2.2. Technological processes for the manufacture of the hot carrier solar cells 55
2.3. Structural characterizations 59
2.3.1. X-Ray diffraction 59
2.3.1.1. X-ray diffraction measurement 60
2.3.1.2. Scan ω/2θ 61
2.3.2. Optical characterization: Photoluminescence 62
2.4. Characterization of solar cells: 64
2.4.1. Quantum efficiency IQE/EQE 64
2.4.2. Dark I-V 66
2.4.3. Light I-V 67
2.5. Modeling of hot carrier solar cells with SimWindows 69
2.6. Modeling of I-V curves with a two-diode equivalent circuit model 72
References: 74
Chapter 3 Towards the III-V/Si tandem solar cell through a monolithic approach 77
3.1. Context of the study 77
3.2. Architecture of the targeted tandem cell 78
3.3. Ohmic contacts on GaP 80
3.3.1. Physics of contacts on semiconductors 80
3.3.2. Contacts on GaP: n+ 82
3.3.3. Contacts on GaP: p+ 83
3.3.4. Contact on Si: n+ 84
3.4. GaP-based absorbers 85
3.4.1. Structural analysis (XRD) 86
3.4.2. Previous results 86
3.5. p-i-n cells with top-top electrical contacts 88

3.5.1. Architecture description 88
3.5.2. Quantum efficiency measurements 88
3.5.3. L-I-V analysis 91
3.6. p-i-n cells with top-bottom electrical contacts 95
3.6.1. Architecture description 95
3.6.2. Quantum efficiency measurements 95
3.6.3. L-I-V analysis 98
3.7. Comparison between both cells 102
3.8. First attempt to develop a tandem cell 104
3.9. Conclusion 107
References: 108
Chapter 4 Towards hot carrier solar cells – Design of selective contacts 111
4.1. Principles of selective contacts 111
4.1.1. Objectives and context of the study 111
4.1.2. Physical principles 112
4.2. Design and simulation 114
4.2.1. Design of the samples 114
4.2.2. Device simulation results 115
4.3. Device presentation and structural characteristics 121
4.3.1. Device presentation 121
4.3.2. Structural characteristics 122
4.3.3. Photoluminescence results 126
4.4. Opto-electrical results 127
4.4.1. Electrical characteristics 127
4.4.3. Photocurrent results 130
4.5. Conclusion 138
References: 139
General conclusions and future works 141
Résumé 143

Introduction

After two great industrial revolutions, fossil fuels such as coal, oil, natural gas have been widely used in human production and life. With the progress of human society and the sustainable development of social economy, the consumption of energy is increasing day by day. And the demand for energy will be greater as the global population increases. However, in the current energy structure of human society, this kind of non-renewable energy still holds a large proportion of the use, while its storage is limited. And the fact is, there is no limitation for human needs. In addition, a large amount of carbon dioxide and some toxic gases will be produced by the combustion of fossil fuels such as coal, oil, natural gas causing the greenhouse effect. The gradual warming of the global climate has brought a very serious impact on the living environment of animals and plants on the earth. Due to the large-scale use of these non-renewable energy sources, a series of serious problems such as ecological destruction, environmental pollution, and energy crisis have arisen. Therefore, developing a kind of renewable energy with huge reserves, clean and pollution-free has become the common goal of today’s society. In result, the development and application of solar energy is imminent.

Compared with traditional conventional energy, solar energy has the following three advantages. Firstly, wherever there is sunlight, there is solar energy. Secondly, according to relevant reports, only 2% of solar energy has been consumed in a billion years. At this rate, for human beings, solar energy can be described as inexhaustible. Solar energy is arguably the most abundant resource available to mankind. Thirdly, in the process of developing and using solar energy, there will not be any production of polluting gases, liquids and other toxic substance, that is to say, solar energy is quite an environmental friendly clean and renewable energy.

The first photovoltaic effect was first experimentally demonstrated by French physicist Edmond Becquerel in 1839. And in 1954, the p-n junction diode potential was discovered at Bells laboratory with the efficiency of 6% using silicon material. Depending on the key materials used and level of commercial maturity of the technology, photovoltaic technologies are classified into three generations. The first generation of solar cells comprises of single crystal and multi-crystalline silicon cells. They are well-matured in terms of their technology, and fabrication process. This type of solar cell is the most widely used and manufactured in the world, almost 90% of the photovoltaic solar cell industry is based on silicon-based materials. While silicon solar cells are expensive to produce, so research led the next generation of solar cells away from silicon. Second generation solar cells are called thin film solar cells that includes amorphous silicon based thin-film solar cells, cadmium telluride (CdTe)/cadmium sulphide solar cells and copper indium gallium selenide ($CuIn_xGa_{1-x}Se_2$, CIGS) solar cells. They cost lower compared to the silicon cells, but they have environmental issues and their efficiency is lower. Due to high costs of first generation solar cells and limited availability of materials and toxicity for second generation solar cells, the third generation of solar cells emerged. They are inherently different from the previous two generations because they do not rely on the p-n junction design of the others. Third generation cells includes latest and upcoming technologies which look promising. The main objective of the research is to produce most effective solar cells which are inexpensive to produce in the same time toxic-free. Third generation cells include nanocrystal based solar cells, polymer based solar cells, dye sensitizes cells, organic-inorganic halide perovskite cells, multi-junction/ tandem cells and hot carrier solar cells.

This PhD work focuses on the third generation photovoltaics and contributes to the development of two families of advanced solar cells: monolithic tandem cells based on III-V on silicon and hot carrier solar cells on InP.

Dissertation overview:

In Chapter 1: Operating principles of a solar cell are firstly presented in details. PN junctions, Photovoltaic conversion, electrical parameters, quantum efficiency and Shockley-Queisser limit are explained. Secondly, multi-junction solar cells are introduced with the architecture and the state of the art. Tandem cells based on Silicon bottom cells are presented in details giving descriptions of the manufacturing methods. Thirdly, hot carrier solar cells are introduced. Principles and thermalisation process and the state of the art of hot carrier solar cell are given in details.

In Chapter 2: The MBE growth of GaAsPN/Si tandem solar cells and hot carrier solar cells on InP substrates at Institut FOTON is presented. Also the technological processes for the manufacture of both types of advanced solar cells are explained. This chapter also contains introduction of structural characterization (X-Ray diffraction), optical characterization (Photoluminescence), quantum efficiency, Dark-IV and Light IV. The last part in this chapter gives brief introduction of two simulation software: ‘SimWindows’, used for modeling of hot carrier solar cell; ‘zweidiodenmodell’, used for modeling of I-V curves.

In Chapter 3: Chapter 3 is all about III-V/Si tandem cell. It gives descriptions of architecture of p-i-n diodes on silicon and ohmic contacts on GaP. Experimental results of two different kinds of contacts on the same sample (top-top electrical contacts and top-bottom electrical contacts) are presented, to study the impact of the GaP/Si interface on the solar cell properties. Sample structure analysis, electrical characterizations and comparison between both type of electrical contacts are given in details. At the last part of this chapter, a first attempt to develop a tandem cell is presented.

In Chapter 4: Chapter 4 is about study of selective contacts towards the development of hot carrier solar cells on InP. Two types of PIN diodes grown on InP substrate with an intrinsic InGaAs “absorber” are studied. One has a barrier and another has a single quantum well serving as the selective contact. Firstly, I used simulation software “SimWindows” to perform modeling for both cells in order to give a point of view to define the composition of the samples. Then, the devices are manufactured and characterized. Structural characteristics (X-ray diffraction) are done on both the HCSC heterostructures and showed good lattice-matching. Photocurrent measurements presented in the last part of this chapter demonstrate a strong influence of the single quantum well on the opto-electrical characteristics.

Chapter 1 Advanced concepts of solar cells: Tandem Cells and Hot Carrier Solar Cells

1.1. Operating principle of a solar cell

1.1.1. PN junction

P-N junctions are of great importance both in modern electronic applications and in understanding other semiconductor devices. The theory of p-n junction serves as the foundation of the physics of semiconductor devices.

Figure 1-1 schematically shows the p-n junction. It is important to realize that the entire semiconductor is a single-crystal material in which one region is doped with acceptor impurity atoms to form the p region and the adjacent region is doped with donor atoms to form the n region. In this configuration, the charge carriers (electrons and holes) of each side will migrate from the region where they are in the majority towards the region where they are in the minority by diffusion. The majority carrier electrons in the n region will begin diffusing into the p region and the majority carrier holes in the p region will begin diffusing into the n region. As we know without external connections to the semiconductor this diffusion process cannot continue indefinitely. As electrons diffuse from the n region, positively charged donor atoms are left behind. Similarly, as holes diffuse from the p region, negatively charged acceptor atoms are left behind. The net positive and negative charges in the n and p regions induce an electric field in the direction from the positive to the negative charge which is from the n to the p region. This electric field region is referred to as the space charge region (SCR). Since the space charge region is depleted of any mobile charge, this region is also referred to as the depletion area.

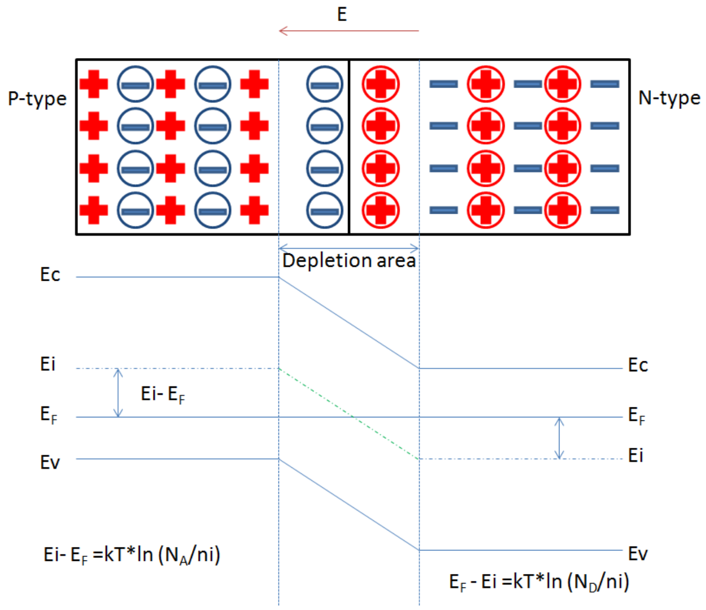

Fig. 1-1: Schematic of a P-N junction

In thermal equilibrium (the Fermi energy level is constant throughout the entire system) the diffusion force and the E-field force exactly balance each other. This results in zero current in the junction. A voltage can be applied across the p-n junction to disturb this balance.

Figure 1-2 (a) schematically shows the energy band diagram of a p-n junction in thermal equilibrium. Figure 1-2 (b) schematically shows a reverse-biased p-n junction. The potential of the n region is positive with respect to the p region so the Fermi energy in the n region is lower than that in the p region. The total potential barrier is now larger than for the zero-bias case. Figure 1-2 (c) schematically shows the case when a positive voltage is applied to the p region with respect to the n region. The Fermi level in the p region is now lower than that in the n region. The total potential barrier is now reduced.

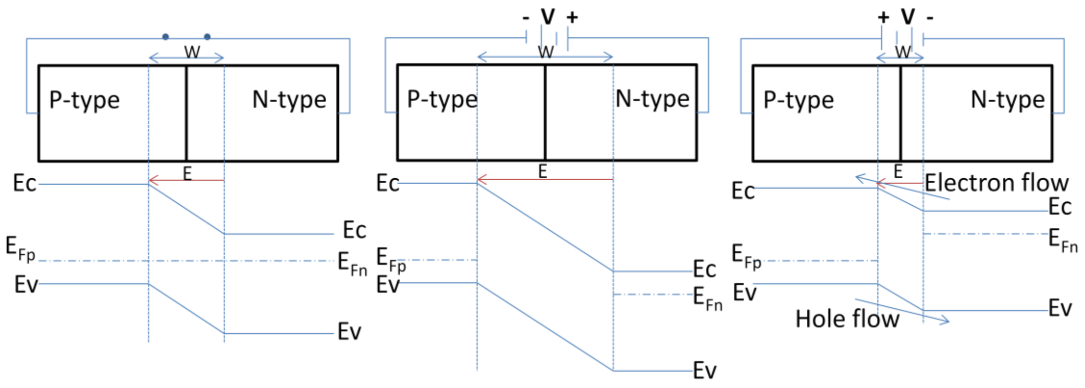

(a) (b) (c)

Fig. 1-2: A p-n junction and its associated energy band diagram for (a) zero bias, (b) reverse bias, and (c) forward bias.

1.1.2. Photovoltaic conversion

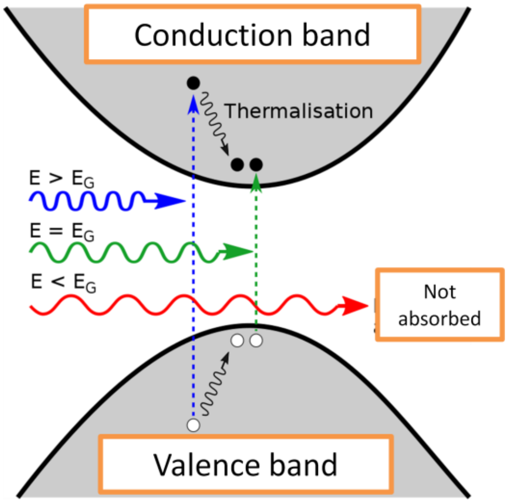

Fig. 1-3: Generation of electron-hole pairs by absorption in a direct bandgap semiconductor with a band gap of Eg.

The photovoltaic (PV) conversion is based on the PV effect, which occurs in a solar cell when photons are absorbed inside the material to generate electron-hole pairs (Fig.1-3). This has the effect of increasing the number of minority carriers in the junction which will then participate in the conduction in the SCR: the intensity of the (reverse) conduction current will increase, so the current-voltage characteristic of the diode will change into negative (Fig. 1-4). In thermodynamic equilibrium, the photo-generated minority carriers will migrate to the region where they are the majority by conduction in the SCR. By short-circuiting the junction, a current will be generated to allow the recombination of these carriers via the external circuit. And this current is called as the short-circuit current (I_{SC}). Under open-circuit conditions, these carriers will not have the possibility of recombination but only accumulate, which will reduce the intensity of the electric field in the SCR and lower the barrier for carrier diffusion. And a new equilibrium will be established when the voltage reaches the open-circuit voltage (V_{OC}). Under these conditions, the diffusion current of the majority carriers is opposite and equal to the photo-current of the minority carriers, and the total current is therefore zero. Please note that the minority carriers are likely to be lost through recombination. Because the efficiency of the cell is proportional to the photo-current (PC), so the lifetime of the minority carriers must be long enough to reach the SCR and thus contribute to the PC.

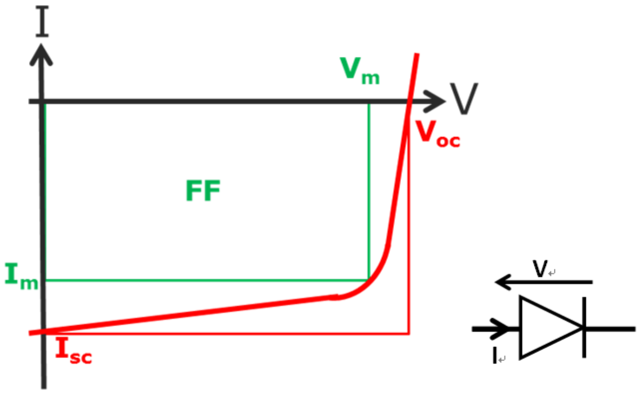

Fig. 1-4: Characteristic I (V) of a solar cell under illumination.

1.1.3. Electrical parameters and quantum efficiency

The efficiency of a solar cell, that is, the ratio between the maximum electric power it can provide and the incident light power, which can be calculated from its current-voltage characteristic under illumination. This characteristic corresponds to the characteristic of a PN diode that converts into negative current by photo-current which is opposite to diffusion current (see Fig. 1-4).

We can see from Figure 1-4 that the maximum electrical energy delivered by the cell (at point (Vm, Im)) can be expressed as a function of the open-circuit voltage (V_{OC}) and the short-circuit current (I_{SC}) by defining the fill factor (FF). The FF is defined as the ratio of the maximum power from the solar cell to the product of V_{OC} and I_{SC}:

$$\mathrm{FF} = \frac{\mathrm{Vm} \cdot \mathrm{Im}}{\mathrm{Voc} \cdot \mathrm{Isc}} \tag{1.1}$$

The efficiency of the cell is then given by:

$$\eta = \frac{P_{max}}{P_{lum}} = \frac{\mathrm{FF} \cdot \mathrm{Voc} \cdot \mathrm{Isc}}{P_{lum}} \tag{1.2}$$

With P_{lum}: the incident light power under the standard testing conditions (STC) AM1.5. In the case of a simple cell, the efficiency will be the maximum if we manage to maximize the parameters V_{OC}, I_{SC} and FF (which depend on the material) through its structural and optoelectronic properties, and also through the architecture of the cell and the quality of the used ohmic contacts. However, the maximum efficiency of a cell is always limited by the phenomena of loss (thermalization processes, transparency, contact losses, etc…). Finding strategies to reduce these losses is therefore crucial to develop sufficiently efficient photovoltaic devices. For instance, the FF can be reduced due to either series resistance (bulk resistance, metallic contacts, carriers transport through the top diffused layer, etc…), or shunt resistances (p-n junction non-ideality, partial shorting of the junction, short-circuits at the cell edges, etc…), or both.

1.1.4. Shockley-Queisser efficiency limit

The Shockley-Queisser efficiency limit (SQ limit) is the maximum theoretical efficiency of a solar cell referring to a single p-n junction to generate power from the cell where the only loss mechanism is radiative recombination.

The main losses in single-junction solar cells are due to the band gap energy of the absorber material. Indeed, the solar cells are "powered" by the polychromatic light of the Sun, the spectra of which is presented in Fig. 1-5.

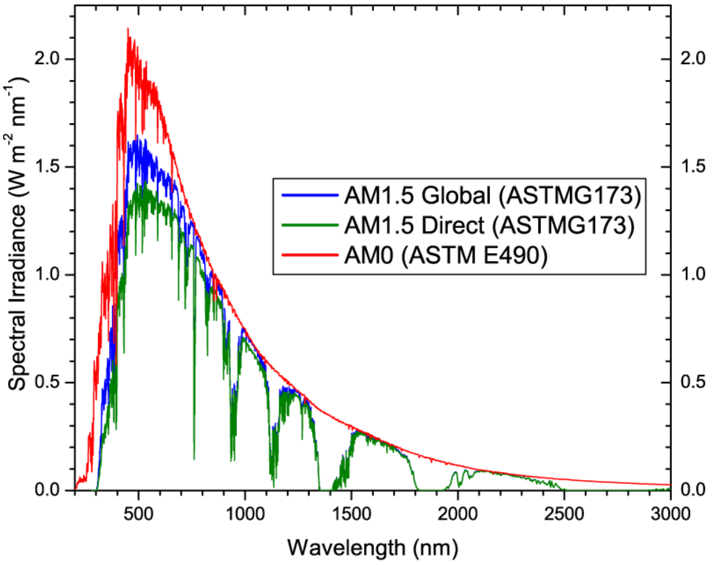

Fig. 1-5: Corrected solar radiation spectrum according to atmospheric filtering for different photovoltaic applications: spatial (AM0, unfiltered), classical modules (AM1.5G) and modules under concentration (AM1.5D) ("PVEducation" n.d.)

In a typical semiconductor, photons with energy lower than the band gap energy of the absorbing material are lost through transmission and therefore, can't generate any carriers (transparency losses). Photons with energy higher than the band gap are absorbed and therefore, can generate electron-hole pairs by the transition between the valence band and the conduction band. However, the part of the energy which is higher than the required energy to make this transition is lost as heat through thermalization by interacting with phonons in the area (thermalization losses).

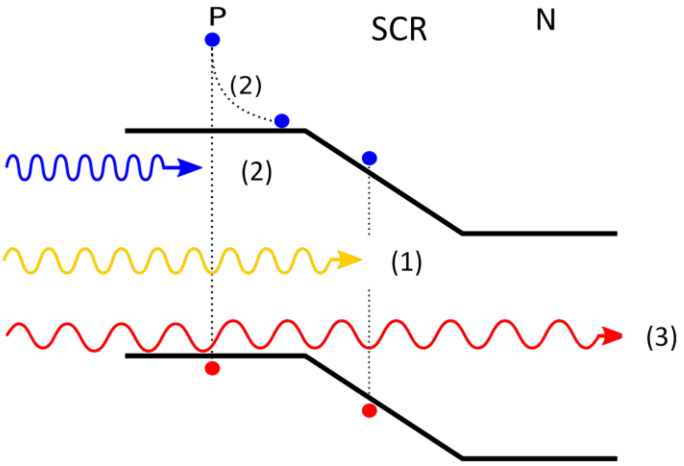

Fig. 1-6: Schematic diagram of a single junction solar cell: (1) Generation of an electron-hole pair by absorbing a photon with the energy equal to the band gap of the absorber. (2) Thermalization of carriers with an energy higher than the band gap of the material. (3) Energy losing when the energy is less than the band gap the material.

In 1961, Shockley and Queisser developed a model to calculate the maximum theoretical efficiency as a function of the absorber's bandgap of an ideal solar cell. Indeed, when the only recombination mechanism is radiative, each absorbed photon will generate an electron-hole pair. In addition, the mobility is assumed to be infinite so all the generated carriers will be collected. Therefore, the short-circuit current increases when the bandgap of the absorber material decreases. And the separation of the quasi-Fermi levels in the p and n regions increases when the bandgap increases. Greater separation of the quasi-Fermi levels results in a higher V_{OC} (this tendency is not verified for very large band gaps, because the number of photo-generated carriers is reduced to zero by the transparency of the material). Ultimately, the maximum theoretical efficiency is proportional to V_{OC} and I_{SC} of an ideal single junction solar cell, resulting from a compromise between the minimization of losses by transparency and the maximization of the separation of the Fermi levels which limits the thermalization losses [1]. In Fig. 1-7, the maximum efficiency is represented as a function of the bandgap energy according to the Shockley and Queisser model. As can be seen, the absorbers around 1.3eV are preferred to obtain the best efficiency (>30%).

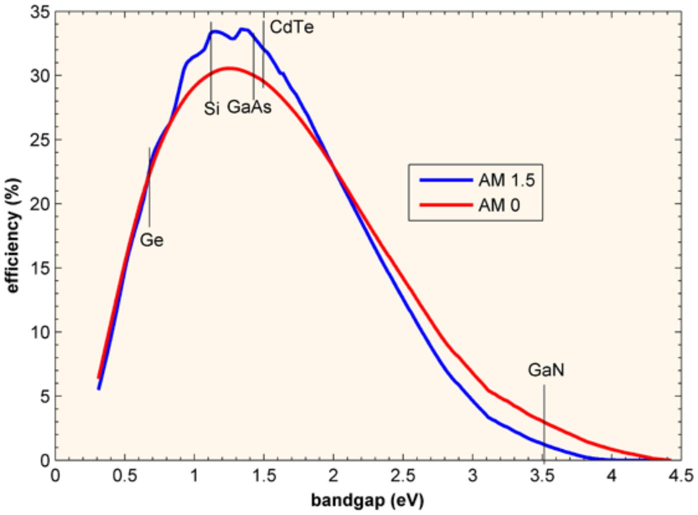

Fig. 1-7: The maximum theoretical efficiency of a single-junction cell as a function of the band gap energy according to Shockley and Queisser's approach [1]

Besides the losses from thermalization and transparency, there is also some losses from the reflection on the cell. Adding a thick anti-reflective layer, having adequate refractive index and texturing the surface allow to change the reflection coefficients and help to limit the refraction phenomena in order to greatly reduce these losses. There are also losses from non-radiative recombination. In fact, when the carriers are generated near a recombination center (non-passivated surfaces, crystal defect, etc.) the length of their scattering decreases, therefore the possibility for them to reach the junction is reduced. The current delivered by the diode will then be less. Moreover, these recombination are the origin of the direct current. This so-called saturation current is the opposite of the photo-current which has been reduced by the recombination mechanism. And this results in a decrease of V_{OC} of the cell. Finally, the Joule effect also causes losses due to the parasitic resistance in series (poor ohmic contact) and parallel to the cell (alternative paths for the carriers that short-circuit the cell).

If the losses from reflection, recombination and Joule effect are due to manufacturing defects of the cell and then they can be reduced by developing suitable technological processes (passivation and anti-reflection layers, better ohmic contacts) and the quality of the material, while the losses from transparency and thermalization are intrinsically linked to the band gap of the material which are physically unavoidable. Noting this, several innovative concepts have been proposed, especially hot carriers and intermediate band solar cells. Multi-junction solar cells which are discussed in the next section are the most mature concept [2]–[4].

1.2. Multi-junction solar cells

1.2.1. Architecture of multi-junction solar cells

The principle of multi-junction solar cell (MJSC) is to stack multiple single-junction solar cells in sequence, from the largest band gap of the upper cell to the smallest band gap of the lower cell. This is a way to limit the thermalization loss as much as possible, the short wavelengths are absorbed by the upper cells, and the long wavelengths lost by transparency are absorbed by the lower cells when they are transmitted throughout the structure [5].

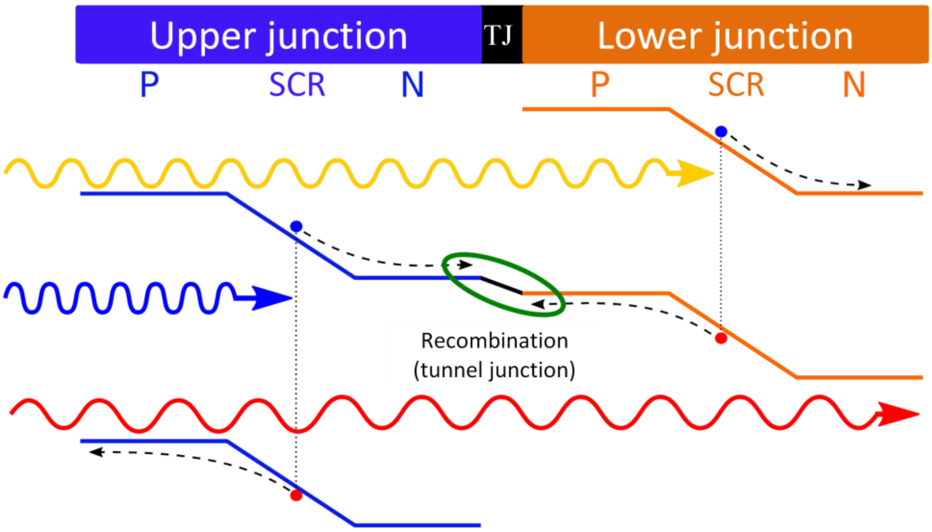

Fig. 1-8: Schematic diagram of a tandem cell: thermalization losses are reduced by using a larger bandgap cell on the top of the structure.

To maximize the absorption of energy radiation between the gap of the lower junction and the gap of the upper junction the thickness of each junction needs to be determined. Generally, the direct gap material with a high absorption coefficient is preferred. In theory, the use of sufficient thickness guarantees a satisfactory absorption. However, carriers generated during absorption must have diffusion lengths long enough to allow themselves to reach the limits of the MJSC. This limits the thickness of the absorbers. Ultimately, the thicknesses must be calculated to achieve an optimal compromise between absorption probability and current collection probability.

Besides these considerations, the MJSC is a series of PN junctions successively crossed through by the carriers. For example, in the case of a tandem cell, the carriers must cross a P-N-P-N sequence which forms a set of two diodes with opposite directions, which would definitely block the current. Therefore, achieving high efficiency MJSC requires the development of high quality tunnel junctions (see Chapter 3 for details) to ensure the electrical conduction between each cell of the structure.

1.2.2. State of the art of MJSC: efficiency conversion records

Today, the MJSC is the most efficient photovoltaic device with double, triple,… or even sextuple junctions' structures that achieve photovoltaic conversion efficiency greater than 35% or even 47% under concentration.

As early as 1984, the National Renewable Energy Laboratory (NREL, Colorado, USA) worked on the development of GaInP/GaAs double-junction which became the first marketable agreement for tandem cells. Since then, they have reported efficiency of more than 27% [6]–[9]. These cells subsequently drew the attention of the aerospace industry.

Research quickly turned to adding a third Ge junction for its lattice match with GaAs and the efficiency is over 47% according to the theory[10]. The lattice matched triple junction GaInP(1.86eV)/Ga(In)As(1.38eV)/Ge(0.67eV) can't guarantee the current the agreement of the current no matter how much photo-current is delivered by the Ge cell. In addition, it is quite complex to obtain Ga(In)As/Ge interface with good quality. In fact, the differences in crystallinity and polarity between Ge substrate and the GaAs layer are the reason for many structural defects. Today, such triple junctions have obtained the efficiency more than 40% and are standard in space and ground application under concentration. The efficiency record has reached 41.6% under 364 suns by Spectrolab in 2009 [11]–[13].

In order to satisfy the condition of current matching, it is moved towards a combination of gaps of [1.75eV/1.18eV/0.70eV] by incorporating more indium in the top and middle junctions. This approach, metamorphic this time, requires growing buffer layers of gradual compositions and to deal with the presence of dislocations which leave room for doubt during the evolution of cells' aging process. However, Spectrolab once again succeeded in improving the efficiency up to 41.6% under 484 suns with a GaInP/GaInAs/Ge lattice-matched cell this time.

In order to reduce the density of dislocations in the upper junctions while at the same time guaranteeing a better current match, the NREL has developed a concept of an inverted lattice-mismatched solar cell, which consists in growing the layers in

increasing order of lattice-mismatching with the substrate, the latter being removed after growth [14]. This approach allowed Sharp to obtain an efficiency record of 44.4% under 302 suns with a InGaP(1.88eV)/GaAs(1.43eV)/InGaAs(0.98eV) on GaAs [15].
The realization of the quadruple junction by wafer boding is: two tandem cells previously epitaxied on two different substrates are then associated by creating atomic bonds at the interface [16]–[18]. This method enabled Soitec and Fraunhofer ISE to announce in 2014 the absolute record for photovoltaic components at 46.0% under 508 suns for a quadruple-junction of very good structural quality made up of a GaInP/GaAs tandem cell bonded to a GaInAsP/GaInAs tandem cell [19].

The latest innovation in MJSC is the realization of sextuple junctions, reaching 47.1% solar conversion efficiency using a monolithic series-connected, six-junction inverted metamorphic structure operated under the direct spectrum at 143 Suns concentration.[20].

Cell	Description	Efficiency
GalnP/GaAs (NREL)	2 junctions pseudomorphic	30.2% (140-180)
GalnP/Ga(In)As/Ge (Spectrolab)	3 junctions pseudomorphic	41.6% (364)
GalnP/Ga(In)As/Ge (Spectrolab)	3 junctions metamorphic	41.6% (484)
InGap/GaAs/InGaAs (Sharp)	3 junctions “inverted lattice-mismatched”	44.4% (302)
GalnP/GaAs/GalnAsP/GalnAs (Soitec)	4 junctions Wafer-bounded	46.0% (508)
AlGaInP/AlGaAs/GaAs/GaInAs/ GaInAs/GaInAs (NREL)	6 junctions “inverted metamorphic”	47.1% (143)

Table 1.1: Efficiency records for multi-junction solar cells. The results obtained are under concentration of light intensity indicated in parentheses.

We can see that systematically performing MJSC leads to making a choice between current tuning and lattice tuning, and also compromising on the involving defaults (current losses, dislocations). From this perspective, the diluted nitrogen has attracted their attention. In fact, the incorporation of even a small percentage of nitrogen in III-V materials makes it possible to reduce their lattice parameter while greatly reducing the width of the forbidden band by a so-call “giant” band curvature effect.[21]. For example, a GaInAs alloy perhaps lattice-matched with Ge or GaAs with a band gap varying between 0.8 and 1.4 eV [22]. However, the growth of diluted nitrogen comes with specific problems because of the metastability of these materials and the behaviors of nitrogen during its incorporation. Therefore, obtaining a homogeneous material with few localized energy states is quite complex. A record of Solar Junction with 43.5% efficiency under AM 1.5D with a triple GaInP (1.89eV)/GaAs (1.41eV)/GaInAsN (Sb) junction (1.0eV) is still obtained in 2012[23].

We can notice that the main disadvantage of MJSC is still the use of expensive GaAs or Ge substrates, which restricts these cells to space applications or solar power plants under concentrator, particularly in manufacturing the wafer bonding which requires two different substrates. The fabrication of MJSC on Si substrates is about ten times cheaper than the most commonly used III-V substrates, which will make it possible to have competitive photovoltaic devices in the market.

1.2.3. Tandem cells based on Si bottom cells

Nowadays, the photovoltaic market is dominated by thick silicon absorber cells. The best silicon-based cells show the photovoltaic conversion efficiency larger than 25%, which is very close to the maximum theoretical limit of Shockley and Queisser [1]. These efficiency records are obtained from monocrystalline silicon cells and Si heterostructures, particularly with an efficiency record of 26.7% obtained in 2017 by the Japanese company Kaneka[24].

Silicon, compared with other materials used in photovoltaics, is such an abundant material, and therefore very cheap. It also occupies a dominant position in the semiconductor market for benefiting from the maturity and strong production capacities of the electronic industry. However, since the present cell records are very close to the limit, it will become more and more difficult to increase further the efficiency. Searching for alternative routes to overpass the SQ limitation becomes now a major objective for PV R&D worldwide. A straight forward strategy is to shift from single to tandem junctions which can reach 43% theoretically by combining 2 sub-cells: a bottom and a top cell collecting respectively the visible/near Infrared and the blue/UV range of the solar spectrum[5]. Reaching 30% in production would be feasible with tandem devices with about 20% efficiency for each junction[25]. This high efficiency technology is currently based on III-V materials grown on expensive GaAs substrates. However, the multi-junction approach is considered to be limited by high production costs for large-scale applications[26]. It is possible to reduce the cost of such device by using the existing silicon technology for the bottom cell. Indeed, the targeted tandem cell architectures rely on a gap stacking of 1.7eV/1.1eV, which provides the maximum theoretical power conversion efficiency with Si as a bottom cell.

The thickness of the top cell is optimized to satisfy the current matching in the structure. It is shown in Fig. 1-9, for the Si bottom cell with a band gap of 1.1eV, the use of a top cell including an absorber with a strong absorption around 1.7eV can theoretically achieve a conversion efficiency more than 43%[5]. Therefore, such a double junction can go beyond the theoretical limit of silicon cells on one hand, and on the other hand, it can compete with MJSC of III-V material from an economic point of view thanks to the small quantities of the III-V material used.

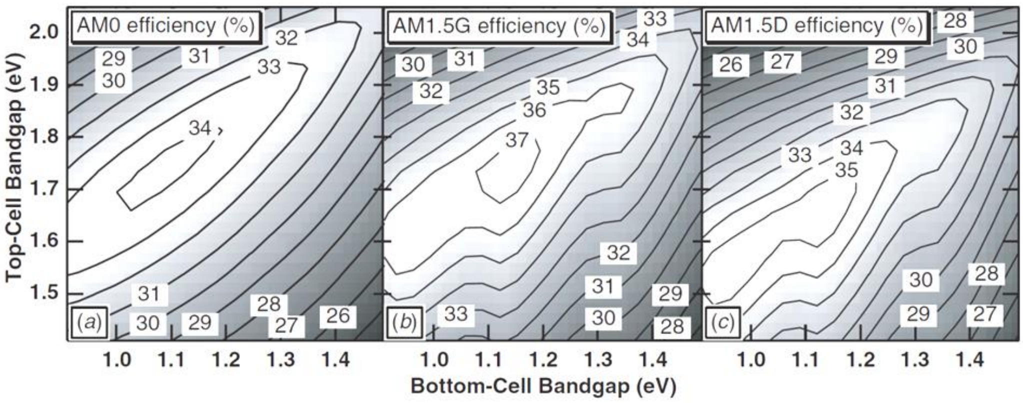

Fig. 1-9: Iso-efficiency contour plots of ideal series-connected two-junction solar cell with an optimized top cell thickness as a function of top-cell and bottom-cell direct band gap using standard spectra: (a) AM0 (space), (b) AM1.5 global (terrestrial) and (c) AM1.5 direct (concentrator terrestrial).

Candidates are either to combine silicon bottom cells with perovskite (PRX) top cells, with an efficiency of 29.8% (HZB), or with wide bandgap Cu(In,Ga)(S,Se) (CIGS), or with III-V (planar or nanowires).

In the state-of-the art, there are several approaches pursued: monolithic growth, monolithic integration (with smart stacking), 3T tandems, and 4T tandems:

Tandem cells made of III-V nanowires on Si substrates

Most direct band-gap III-V compounds are lattice-mismatched with silicon, leading to detrimental dislocation densities. Therefore, the approach of growing nanowire (NW) arrays on top of the silicon avoids the lattice-mismatch issues. Moreover, this approach benefits from a large light trapping effect, a reduction of the reflection losses and a production cost reduction as compared with the planar III-V layers approach.

For instance, proof-of-concept of two-terminal tandem cells made of a top III-V core-shell nanowires cell onto a bottom silicon cell, (111)-oriented, electrically connected through an all-Si tunnel junction have been reported, either using a GaAs homojunction[27], a GaAsP homojunction[28], or a GaAs/GaInP heterojunction, , and epitaxially grown onto a patterned silicon substrate. The NWs core/shell are grown by the VLS method for the core and a VS one for the shell.

Moreover, tandem cells composed of a top cell of GaAs/AlGaAs core/shell nanowires, grown by the VLS method, on a silicon bottom junction have been developed[29][30].

Perovskite/Si Tandem Solar Cells

Hybrid deposition process for Monolithic Two-terminal Halide Perovskite/Si tandem solar cells (PVK/Si) have raised much attention due to the compatibility of the PVK with silicon bottom cells, in particular their compatibility to the textured silicon bottom cell. A record efficiency of a PVK /Si tandem cell of 29.5% was reported by OxfordPV in 2020. A collaboration between IPVF, EDF R&D, and CEA-INES evaluates the scalability of tandem devices fabrication towards industrial mass production, using a mixed halide $MA0_{.3}FA_{0.7}Pb(I_{0.84}Br_{0.16})_3$. In particular, they use slot-die coating as an upscalable technique for the PbI2 conversion into perovskite, these perovskite layers showed conformity on the pyramidal texture present on silicon substrates surface.

Large size four-terminal PVK/Si tandem solar cells are also studied by IPVF, EDF R&D, C2N and LRCS, using first a spin-coating deposition process, then a slot die coating process. As a first step, full-stack devices have been made, based both on functional semitransparent perovskite solar cells and filters that optically replicate the stacks. These final objects allow reaching 23.3% efficiency (16.9% for the perovskite cell and 6.4% for the c-Si cell) with stable encapsulation. the fabrication of a functional 4T tandem device with a potential efficiency beyond 25% is currently in progress[31].

3-terminal tandem solar cells

Three-terminal (3T) photovoltaic tandem solar cells which combines an interdigitated back contacted (IBC) bottom lateral subcell with a heterojunction vertical top cell are also developed. In this 3T architecture the two subcells work independently and there is no need for any current matching between the 2 subcells, so that no tunnel junction is required[32], [33]. It is particularly well suited to silicon back contact subcells and to various types of top cell materials from III-V compounds or perovskites[34]. The 3T concept cell can be realized with less technological steps and at a lower cost compared to the conventional 4T process.

Tandem cells made of III-V planar layers on Si substrates

The lattice-mismatched route of growing planar III-V compound onto silicon leads to a high density of structural defects, mainly misfit and threading dislocations due to both lattice and thermal mismatches. This can be lowered using a metamorphic graded buffer, which necessitates, however, to grow a large thickness for the buffer. Therefore, wafer bonding or mechanical stacking, either in a 4T (4 terminals) or a 2T (2 terminals) configuration, are also employed to overcome this issue. The III-V top junction is first epitaxially grown on a III-V substrate and then reported on a Si bottom cell. These approaches are combined with a substrate reuse strategy in order to lower the costs due to the expensive Ge or III-V substrates. The CEA-LETI in collaboration with the Fraunhofer –ISE institute, own a record value of 23.7±1.7% at 9.68 suns obtained for the 2J-2T Si-based tandem solar cell, which consists of the record efficiency for this kind of solar cells[35]. C2N is developing a 2T architecture made of a thin-film top solar cells bonded on Si. The transparent and conductive bonding layer made of low refractive index materials enable current matching, bonding of rough or even textured cells, with overall maximum efficiencies even higher than enabled by direct bonding thanks to photon recycling effects. It releases many constrains commonly found in the fabrication of 2T tandem solar cells (requirement of flat surfaces, tunnel junction, temperature constrains…). First proof-of-concepts are made of III-V//Si (collaboration with Fraunhofer ISE, IPVF common research program)[36]. This architecture is being extended to other solar cell technologies with UMR IPVF (CIGS//Si, PVK//Si…).

MBE-grown III-V ternary compounds with a bandgap around 1.8-1.9eV are also studied to develop the top-junction sub-cell: A consortium composed of IPVF. Total new energies, C2N and EDF R&D have studied heterojunctions composed of n-GaInP/p-GaAlAs structure, the GaAlAs being the absorbing layer with a gap of 1.73eV. The efficiency of 18.7% at the 1.73 eV bandgap appears suited for Si-based tandem solar cells[37].

The lattice-matched route is also addressed through the epitaxy of GaAsPN/GaP/Si[38]–[42].

In the following, I report on the study of GaP/Si-based cells towards the development of such kinds of tandem solar cells, following the study made during the ANR MENHIRS project (ANR-11-PRCE0007, 2011-2015).

1.2.3.2. Methods of manufacturing tandem cells on silicon

1.2.3.2.a. Wafer bonding

Wafer bonding technology is one of the possible non-epitaxial approaches for the production of solar cells based on III-V materials on Si substrate. It consists of the transfer of epitaxial layers on III-V substrate onto Si substrate. The main drawback of this method lies in the difference of thermal expansion coefficients between III-V semiconductors and silicon which leads to the generation of cracks in solar cells. The use of ion implantation, where hydrogen ions weaken the bonds in a thin layer of the substrate in order to extract it by exfoliation, has already made it possible to obtain a GaInP/GaAs tandem cell transferred onto Si[43]. However, using two substrates instead of one makes bonding methods comparatively expensive compared to epitaxial fabrication methods, even though progress has been made in the field of substrate recycling.

1.2.3.2.b. Metamorphic growth

In the approach of metamorphic, the absorber of the top cell, chosen for its optimal optical properties with regard to the operation of the tandem cell (strong absorption by direct transition in the forbidden band around 1.7 eV), is not lattice matched with the substrate. This lattice mismatch leads to the formation of dislocations throughout the cell. The presence of dislocations is extremely harmful for the collection of all the charge carriers and therefore for the performance of the solar cell, as it induces a loss of part of the photocurrent by non-radiative recombinations. Consequently, this strategy requires the use of dislocation localization methods such as the growth of a buffer of gradual composition prior to the growth of the absorber which ensures the relaxation of the mechanical stresses in the structure. The absorber then contains fewer dislocations, making it possible to partially reduce current losses in this type of cell.

1.2.3.2.c. Pseudomorphic growth

The pseudomorphic approach is the strategy which satisfies both the conditions of current matching and lattice matching between the top and bottom cells. In this approach, the III-V material of the top cell, presenting a good absorption around 1.7 eV, is chosen so as to also lattice match with the silicon bottom cell. Theoretically lattice matching guarantees the absence of dislocations, thus avoids non-radiative recombination and induces longer carrier lifetimes and therefore better photovoltaic conversion efficiencies are obtained.

Pseudomorphic growth is the strategy chosen within the framework of this thesis for the realization of III-V tandem cells on Si which will be detailed after. The choice of the top cell material and its properties will be explained in particular.

1.2.4. GaP/Si-based cells (with state of the art of FOTON lab: GaP/Si interface)

The gallium phosphide GaP is a prime candidate for integration on silicon due to the low lattice mismatch between GaP and Si (0.37% at room temperature). In addition, the large band gap of this material (2.26eV) gives great interest in the production of a tandem cell on silicon to limit losses by thermalization of low wavelength radiation. The particularities of the GaP/Si interface will be discussed here. Then, the state of the art of cells based on the GaP and GaP/Si will be reviewed, focusing particularly on the results obtained within the framework of a pseudomorphic growth approach.

1.2.4.1. GaP/Si interface

The growth of GaP on Si is favored because of the very low lattice mismatch of 0.37% between these two materials. The critical thickness is between 45 and 95nm (below which the GaP remains in compression on the substrate)[44]. However, beyond this thickness, it is necessary either to choose an appropriate alloy for pseudomorphic growth, which is possible by incorporating nitrogen or boron[45], [46], or adopt a metamorphic strategy that requires containing the dislocations in buffer layers.

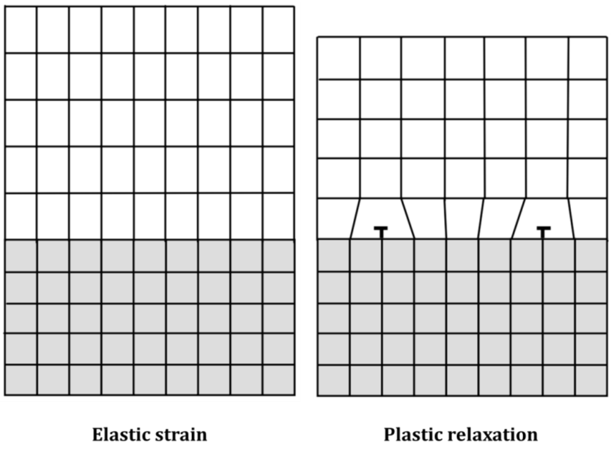

Fig. 1-10: Elastic stress and plastic relaxation at the interface between two lattice mismatched semiconductors. We see two dislocations in the relaxed case (identified by the symbol “T”).

But the main challenge to grow a III-V material such as GaP on Si comes from the differences in symmetries and polarizations between these materials. Indeed, GaP is a zinc-blende type structure with a lattice parameter equal to 5.450 Å, while Si crystallizes in a diamond type lattice with a lattice parameter of 5.431 Å. Moreover, GaP is a polar material because of the difference in electronegativity between Ga and P which does not exist in a crystal containing only Si atoms. As a result, during growth, the GaP atoms do not benefit more from energetically favorable positions for adsorption on the Si substrate.

Under these conditions, sequences of Ga-Ga and P-P bonds will appear and form two-dimensional structural defects called antiphase boundaries ("antiphase boundaries" APB, Fig. 1-11) and its direction follows the reticular planes of the crystal[47]. Stacking faults including in particular micro-twins ("microtwins" MT, Fig. 1-11) can also appear during growth. MTs arise from the rotation of the crystal around the <111> direction[48], [49].

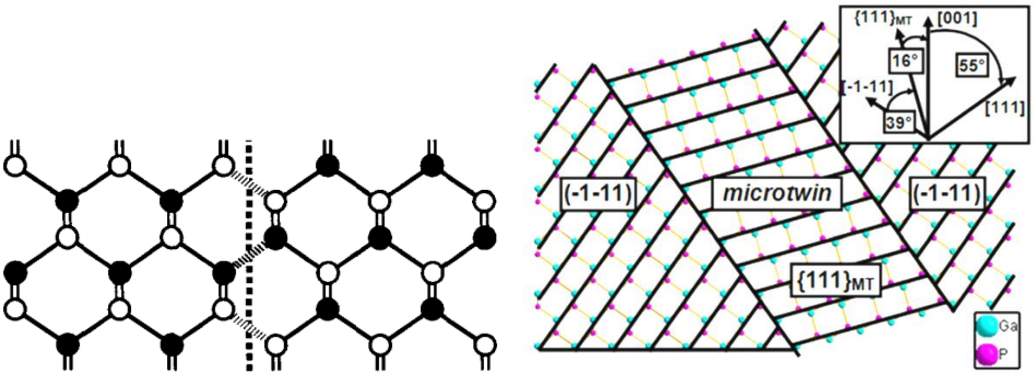

(a) (b)

Fig. 1-11: (a) APB (dotted vertical line) in the zinc-blende structure, including both types of Ga-Ga and P-P bonds[50]. (b) Schematic representation of an MT in the zinc-blende GaP structure[49].

The optical and electrical properties of these defects are still poorly understood, but it is considered that these defects, which propagate throughout the volume of the structure, behave as non-radiative recombination centers, to the detriment of the performance of the components. Moreover, it has been recently demonstrated that GaP antiphase Boundaries act as semimetal singularities able to promote efficiently charge carrier transfer[51]. Some works, mentioned later in this manuscript, have focused carefully on the growth conditions of the first monolayers of III-V materials on Si in order to reduce the densities of these defects.

1.2.4.2. GaP and GaP/Si-based solar cells

1.2.4.2.a. Mono-junction cells

As integration on Si requires removing a number of scientific obstacles regarding the structural, electrical and optical properties of the III-V/Si interface, many studies have initially relied on the development of mono-junction solar cells based on GaP. This work was first motivated by its high gap (2.26 eV) for the production of top cells in MJSCs. The theoretical maximum efficiency for such bandgap energy is about 17%. GaP absorber cells were obtained by MBE by Allen et al. in 2010 with an efficiency of 1.17%. 2.6% were obtained by this same group through incorporating an anti-reflection layer on the cell. These low efficiencies are because of the front face recombination phenomena and the short lifetime of p-type charge carriers[52], [53]. Also by MBE, in 2015, Vaisman et al. demonstrated an efficiency of 2.47% for a GaP cell with an AlGaP window layer and ways to optimize growth conditions and structure design[54]. GaP cells have also been fabricated by liquid phase epitaxy. The low efficiencies obtained are again because of the recombinations on the front face and the low diffusion lengths of the carriers[55].

From an optical point of view, the GaP is disadvantaged because of the strongly indirect character of its gap. Indeed, the absorption coefficient in GaP above 2.26 eV reaches only 10^2-10^3 cm^{-1} [56]. Based on this observation, efforts have been made to develop direct bandgap GaP-based materials with a particular interest for gaps of 1.7 eV which would be optimal for a tandem cell on III-V/Si[6], [38]. It is most often $GaAs_xP_{1-x}$ or $GaIn_xP_{1-x}$ type absorber materials developed as part of a metamorphic approach. As mentioned earlier, the lattice mismatch between the substrate and the absorber requires the use of buffer layers of gradual composition to dissipate the mechanical stresses and limit the propagation of dislocations between the substrate and the absorber. In this approach, in 2006 Geisz et al. demonstrated 9.8% efficiency in a $GaAs_{0.7}P_{0.3}$ absorber p-n junction (bandgap: 1.71 eV) in lattice mismatch on Si. The growth was carried out by MOCVD and a GaAsP buffer of graded composition was used to contain the dislocations [57]. In 2014, Yale researchers obtained 9.3% for a 1.66 eV $GaAs_{0.77}P_{0.23}$ absorber grown by MBE on GaP/Si platforms[58]. In July 2017, they reported an improvement in the efficiency to a record of 15.3% for this type of cell thanks to a drastic reduction in the density of dislocations and a very efficient anti-reflection treatment[59]. The same group has also developed a higher bandgap (2.1-2.2 eV) $In_{0.30}Ga_{0.70}P$ cell intended for operation as the top cell of an MJSC with an efficiency of 3.9% and optimization pathways for growth conditions[60]. In 2015, another cell obtained by MOCVD on Si with a gradual SiGe buffer demonstrated 11.5% thanks to a

$GaAs_{0.76}P_{0.24}$ absorber at 1.71 eV [61].

1.2.4.2.b. Tandem cells

Very few GaP-based tandem photovoltaic devices on silicon have been reported because of the difficulty of obtaining both high-efficiency GaP-based cells and low defect density at the GaP/Si interface. However, a few laboratories have obtained promising results. The first reported prototype is a $GaAs_{0.7}P_{0.3}$(1.77 eV)/Si(1.1 eV) tandem cell grown by MOCVD on Si in Japan in 1994. This metamorphic tandem cell delivered an efficiency of 12.5% under AM0 [62]. Another GaAsP/SiGe tandem cell was done by MOCVD on Si substrate in 2014 and showed 18.9% efficiency with surface anti-reflection treatment[63]. GaP/Si tandem cells are also the subject of a patent by Landis in 2006. Another type of tandem photovoltaic cell integrated on a silicon substrate was obtained by the Fraunhofer ISE in 2015. They are two GaInP(1.9 eV)/GaAs(1.4 eV) tandem cells. The first was obtained by metamorphic MOVPE via the use of a GaAsP buffer on Si substrate and the second was obtained by growth on GaAs followed by a transfer on Si through wafer bounding. Reported efficiencies for these cells are 16.4% and 26.0% respectively[64].

1.2.4.3. Pseudomorphic growth based on Ga(As)PN on GaP/Si

The pseudomorphic approach for the realization of a tandem photovoltaic cell on silicon consists in finding a strategy to correct the two main drawbacks related to the use of GaP-based absorbers. First of all, it is necessary to manage to modify the band structure of the material to lower its gap towards the optimal value of 1.7 eV while giving it a pseudo-direct character and thus favoring optical absorption. Then, in order to reduce the efficiency losses reported previously and which are linked to the presence of dislocations, it is necessary to guarantee the perfect lattice match with Si. Thus, we could achieve a cell with both reasonable costs and high efficiencies.

GaP-based dilute nitrides are the most suitable materials for a pseudomorphic approach. Indeed, the lattice mismatch between GaP and Si is already very low (0.37% at room temperature) and can be reduced by incorporating nitrogen atoms into the GaP lattice. Since the bending factor is high between GaP and GaN, the corresponding GaNP alloys also exhibit a remarkably lower gap than GaP and strong absorption for energies above 1.9-2.0 eV[65]–[69].

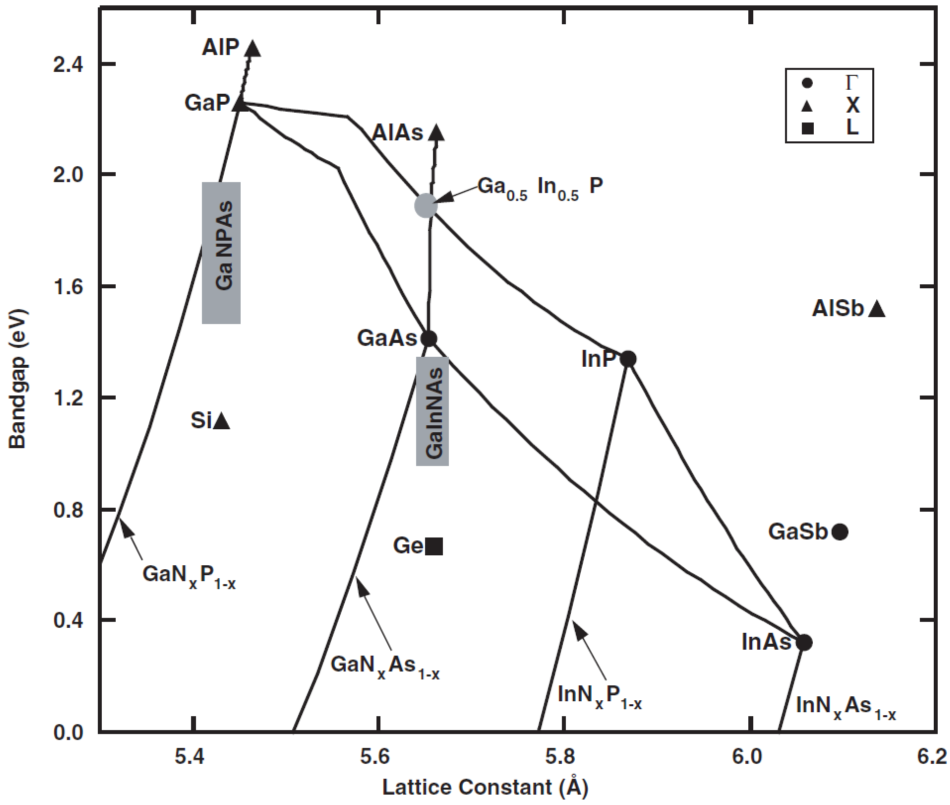

Fig. 1-12: Bandgap energy as a function of the lattice parameter of some semiconductor materials[38].

We clearly see the advantage of GaP-based alloys for pseudomorphic integration on Si.

This decrease in the width of the forbidden band is explained by the hybridization of the localized states of the nitrogen atom with the Γ band of GaP which results in the appearance of two conduction bands Γ- and Γ+ (see Fig. 1-13 (a)). In 2015, a GaP/GaNP/GaP solar cell obtained by Tu et al. in San Diego achieved the extremely promising efficiency of 7.9% with a 2 µm thick GaNP absorber and an anti-reflection layer [70].

For a better current agreement with Si cell, it is possible to further lower the gap to the value of 1.7eV while preserving the lattice match by incorporating Al, As, In or Sb. For example, work has been carried out on the GaAsPN quaternary alloy. As shown in Fig. 1-13, theoretically an alloy of GaAsPN composition containing about 12.5% arsenic and 4.7% nitrogen is needed to obtain the lattice match on Si and a gap of 1.7eV. Experimentally, it was concluded that the pseudo-direct character of its gap was suitable for the functioning of the top cell of a tandem cell on Si thanks to a strong absorption around 1.7eV [38], [42].

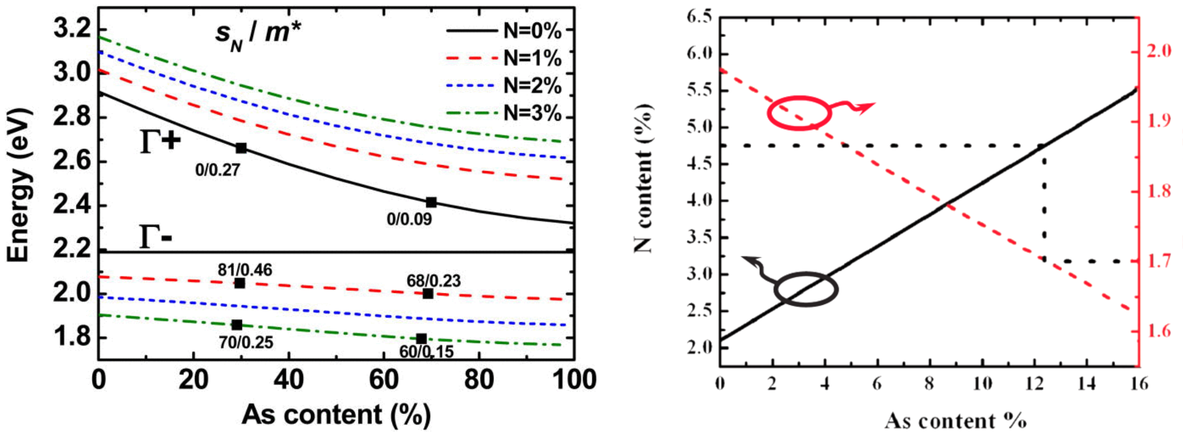

(a) (b)

Fig. 1-13: (a) Γ+ and Γ- conduction bands for bulk GaAsPN biaxially strained at 0K for different compositions according to the tight-binding model [71]. (b) Evolution of the nitrogen content in the GaAsPN alloys as a function of As for an exact lattice matching (black line). Bandgap energy for the corresponding GaAsPN alloys, determined with sp3d5s*sN tight-binding calculations (red line) [42].

The pseudomorphic approach for the realization of a tandem cell on Si from GaAsPN has been exploited by a team from NREL in Colorado and in our laboratory. In 2002, NREL produced, by MOCVD, a mono-junction solar cell of GaP/GaAsPN/GaP which showed 3.8% efficiency for a 640 nm thick absorber. This cell was first integrated in the tandem architecture on silicon in 2005. They achieved 5.2% efficiency via both a 1.0 µm GaAsPN absorber for the top cell and a Zn and Se doped GaP/GaNP tunnel junction [72]–[74]. At FOTON, mono-junction cells on GaP precursors of the work presented in this manuscript were also obtained by MBE. The laboratory record stands at 2.3% efficiency with a 300 nm GaAsPN absorber[42].

These last experimental results are very far from the theoretical efficiency predictions. A GaAsPN junction with a direct gap absorber of 1.7eV promises efficiencies of up to 30% under AM1.5G according to Shockley and Queisser limit. And, as explained before, simulations predict up to 37% for the corresponding tandems on Si.

This poor performance is explained by the difficulty of growing dilute nitrogen of satisfactory structural quality. Indeed, these materials are known to be metastable and are subject to specific processes during growth[75], [76]. The incorporation of nitrogen is in particular a crucial problem. Nitrogen atoms can be incorporated into the crystal by substitution but also in interstitial sites and tend to generate point defects or to group together in packets (clusters), specifically during growth at too low temperatures [77]. The growths carried out at excessively high temperatures lead to nitrogen desorption phenomena and to inhomogeneities by phase separation [78]. All these defects are harmful for the lifetime of minority carriers in the solar cells and must be eliminated as much as possible, which requires substantial work to optimize the growth conditions of the materials. From this point of view, MBE has an advantage over gas phase epitaxy methods because it makes it possible to avoid the problems associated with carbon and hydrogen pollution, to better control the quantity of nitrogen incorporated and to grow at lower temperature. These issues related to dilute nitrogens have been raised in several studies[79]–[81].

The realization of a quality tunnel junction is also a central point which will be discussed later. In the case of the NREL tandem cell, they report that the dopants (Zn and Se) used are sensitive to diffusion, hence a very likely degradation of the tunnel junction during the manufacturing process. In our case, an efficient tunnel junction, all silicon made, has been developed by INL, during the ANR MENHIRS project.
Finally, the behavior of III-V/Si interfaces with its specific defects (APD, MT) remains poorly understood and raises questions about the transport of electrical charges.

1.3. Hot Carrier Solar Cells

1.3.1. Principles of the HCSC

The Hot carrier solar cell (HCSC) was first introduced by Ross and Nozik in 1982[4]. Unlike conventional solar cell devices, the HCSC maintains the hot carrier population by inhibiting the ultra-fast cooling processes. An ideal HCSC absorb a wide range of photon energies and extract 'hot' carriers before they thermalize to the band edge. So it is important to slow down the carrier cooling rate to have the hot carriers collected whilst they are still hot, which means higher voltage achieved , which also means higher efficiency achieved. The other important thing about HCSC is to have energy selective contacts (ESCs) which only allow extraction of carriers through a very narrow range of energies of the device contacts. Fig. 1-14 shows a schematic band diagram of a HCSC [82].

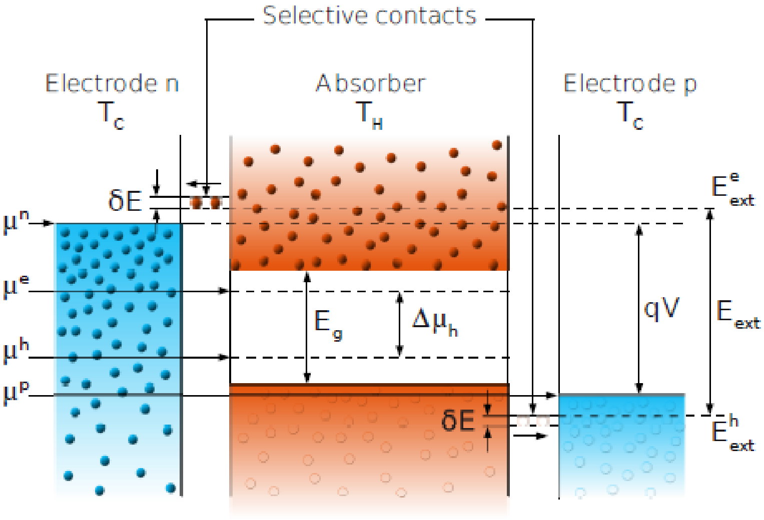

Fig. 1-14: Band diagram of the hot carrier solar cell.

The difference between the extraction energy of holes E^h_{ext} and electrons E^e_{ext} is the extraction energy E_{ext}. δE is the energy width of selective contact. μ_n and μ_p are the 'cold' quasi-Fermi level of electron and hole, the difference between them is the electrical difference of potential qV. The electrical difference potential is written as below (equation 1.3) in a classical solar cell, while for the case of HCSC written as equation 1.4.

$$qV = \Delta\mu_l = \mu_n - \mu_p \tag{1.3}$$

$$qV = \Delta\mu_l = \left(1 - \frac{T_l}{T_h}\right) E_{ext} - \Delta\mu_h \frac{T_l}{T_h} \qquad (1.4)$$

with T_l the lattice temperature. If $T_h = T_l$ we can get Eq. (1.3).

In a conventional cell, the photo-generated carriers first go through an ultra-fast elastic scattering, which result in a thermal distribution at high temperature. They lose their energy gradually by colliding with atoms in the material and in the same time producing phonons. And this process occurs on the time scale of picoseconds, after that the carriers have energies close to the band edges. These thermalized carriers are then extracted from the contacts to contribute to the current. Certainly, there are recombination of electrons and holes during the process.

The dynamics of the carrier after a pulsed monochromatic excitation is described in Figure.1-15 from Green [2].

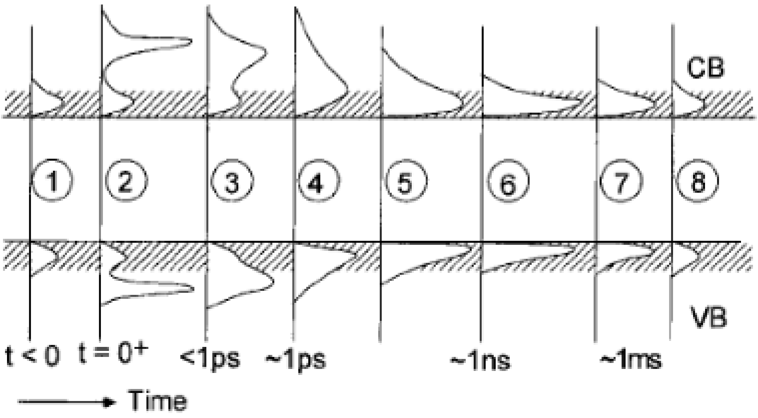

Fig. 1-15: Time evolution of electron and hole distribution in a semiconductor after a laser excitation[2].

① thermal equilibrium before laser excitation;

② immediately after absorption at t = 0, carriers are generated in a narrow energy range;

③ carrier-carrier scattering;

④ thermalisation of 'hot carriers';

⑤ carrier cooling towards the lattice temperature because of interaction with phonons;

⑥ lattice thermalised carriers;

⑦ recombination of carriers with a nanosecond to sub-microsecond time constant or extraction through the contacts;

⑧ return to thermal equilibrium.

1.3.2. Thermalisation process

The carriers thermalize with the environment mainly because of its interactions with the lattice vibration modes, which occurs in few picoseconds, which is much faster than the carrier extraction time in classical solar cells. To have a population of hot carriers, the carriers have to be extracted before thermalisation, which means the thermalisation rate has to be controlled and reduced.

Immediately after absorption, the photo-generated electron-hole plasma distribution is not an equilibrium Fermi-Dirac distribution. In the case of carriers excited by a laser, electrons and holes are generated in a very narrow area in the energy-momentum space. In chemical and thermal disequilibrium with the environment, the population of carriers is subject to different scattering processes that could bring it to equilibrium.

Intraband Scattering

The intraband scattering is from Coulomb elastic interaction between free carriers[83]. Electron-electron, electron-hole and hole-hole scattering occur with exchange of energy and momentum to more uniformly distribute the excess kinetic energy amongst carries. Here the carriers stay in their respective energy band (no recombination), and this interaction is called intraband scattering.

It is a very fast two-particles process that depends quadratically on the carrier density. Its typical time scale is in femtoseconds.

Considering this process, the free carrier population naturally evolves to a Fermi-Dirac distribution defined by a temperature that is common to electrons and holes (thermal equilibrium), which can be much higher than the environment temperature, since no interaction with the lattice has occurred. With different time constant for electron-hole interaction and electron-electron or hole-hole interaction, different temperature for electrons and holes can be obtained.

Interband Scattering

The collisions between carriers can also result in electron-hole pair generation or recombination in non-radiative processes. Two cases are possible:

- Auger recombination: an electron and a hole recombine, and give their energy to a third free carrier (electron or hole).
- Impact ionization: a high energy free electron (or hole) donates a part of it energy to produce an exciton.

The total energy of the free carrier plasma is conserved, while the number of particles not. It is a three-particle process, therefore the probability is less than the intraband scattering. The typical time constant is 100 ps (table 1.2). It also depends on the band gap, and can become quiet efficient in small band gap materials. The exchange between electrons and holes results in an equilibration of chemical potentials of electrons and holes. In the limit of very fast Auger recombination and impact ionization, electrons and holes can be considered in chemical equilibrium with quasi-Fermi level splitting approaching zero[84].

Model	Ω_s	η_{max}	$E_{G_{opt}}$	T_H
Conventional single junction	6.8×10^{-5} 2π	31% 41%	1.4 eV 1.1 eV	300 K 300 K
Particle Conservation	6.8×10^{-5} 2π	66% 86%	0 eV 0 eV	3600 K 4200 K
Impact ionization	6.8×10^{-5} 2π	53% 85%	0.9 eV 0 eV	348 K 2470 K

Table 1.2: Comparison of limits of efficiency (η_{max}), optimal band gap ($E_{G_{opt}}$), and carrier temperature in optimal operating conditions (T_H) for conventional single junction and different hot carrier models under non-concentrated (Ω_s=6.8 x 10^{-5}) and fully concentrated ($\Omega_s = 2\pi$) 6000K black-body spectrum.

1.3.3 State of the art of HCSC

The physical concept of hot carrier solar cell was first introduced in 1982 by Ross and Nozik[4]. And immediately after, simulating their performances was of main interest, in order to understand their concept potential. Nowadays, even after three decades, there is not only a lack of hot carrier solar cell experimental characterization but also the requirement of the use of relevant conditions for operating this kind of solar cells. Ross and Nozik extracted a theoretical maximum conversion efficiency of 66% under AM1.5 approaching the infinite stack of cells.

In 1997, P. Würfel introduced the impact ionization dominating Auger recombination and inelastic phonons scattering in the absorber, he explained the establishment of a hot distribution, which must not be in contact with metallic electrodes, where the phonon scattering prevails[84]. Consequently, hot carriers must be isolated and their extraction should be isentropic to minimize their thermalization towards ambient temperature. The energy selective contacts (ESC) would satisfy these conditions, I will talk more about ESC in chapter 4. In 2003, Chen et al studied the carrier relaxation dynamics in w-InN with free carrier density of 1.3 x 10^{18} cm^{-3}, where a substantially long 20 ps hot carrier relaxation time was extracted from the fast decay component of carrier cooling trend due to phonon bottleneck effects (PBE). This study implies that the dominant energy relaxation in w-InN is LO phonon scattering and a strong hot phonon effect takes place due to the high carrier density because of high illumination and large phononic bandgap[85].

In 2007, Jang et al explored w-InN with different thickness under identical excitation laser power, which indicated that the effective phonon emission time decreases with reducing carrier density and the trend of phonon emission time is attributed to the PBE [86]. In 2013, Collier et al found a significantly extended carrier relaxation in GaP, providing another perspective on the relationship between phonon bottleneck effects and intervalley scattering [87]. In this work, a power-dependent carrier relaxation in GaP wasobserved over 30 to 52 ps for 2.3 to 72 µJ/cm^2 attributed to the wide phononic bandgap and to population of a low-energy side valley at low fluences and to screening effects at high fluencies.

Bulk III-V semiconductors are in general not appropriate candidates for hot carrier absorber due to their picoseconds timescale hot carrier lifetimes compared to the required several nanoseconds. However, their relatively simple electronic/phononic structures provide an insight into the mechanisms underlying the PBE.

Strong interest was shown on the study of carrier cooling rates in GaAs quantum well structures. The most commonly studied structures were GaAs/AlGaAs multi-quantum wells and super-lattices. In 1984, an experimental study by Xu and Tang using picoseconds photoluminescence showed that the carrier energy loss rate is much more carrier-density dependant in quantum wells than in bulk material. As a result, the carrier cooling rate is strongly reduced in quantum wells and becomes significantly lower than in bulk when the carrier density is higher than 10^{18} cm^{-3}. They also found that higher temperatures were reached in QWs than in bulk under high excitation [88]. In 1990, Nozik et al calculated the time-averaged T_C in GaAs/AlGaAs SLs and MQWs with constant well widths and varying barrier thickness by fitting the tail of time-integrated PL spectra at 77 K to a Boltzmann distribution [89]. In addition to a slower hot electron cooling rate for MQWs rather than bulk GaAs at high excitation (carrier) density, this also demonstrates that T_C of SLs with strongly coupled mini-bands is significantly lower than that of MQWs under similar carrier density.

More recently, a study on the carrier relaxation in GaAs/AlAs MQWs with either varying barrier thickness or varying well thickness through TRPL at 300 K was carried out [90]. At high photoexcitation density, the carrier relaxation rate appears to be more closely related to the thickness of the barrier rather than to that of the well, with the longest carrier lifetimes reaching nanoseconds for the thinnest (2nm) barriers. This study concludes that the hot carrier diffusion rate, reflection, and localization of phonons could influence the strength of PBE in such MQWs. A series of studies on the carrier relaxation in InGaAs-based MQWs was carried out by Hirst et al. With increasing well width, higher indium fraction, and deeper QW, a reduction in the carrier cooling rate, that is, a lower carrier thermalization coefficient (Q) value, was observed.

In 1998, Zhang et al first studied the carrier relaxation in $In_{0.15}Ga_{0.85}N$/GaN SQW through time-resolved cathodoluminescence (TRCL) at 93 K [91]. The carrier lifetimes derived from bright center and dark boundary regions were found to be 2.3 and 1.4 ns respectively. On the other hand, the temperature effect on carrier relaxation in $In_xGa_{(1-x)}N$/GaN (i.e., x = 11%, 16%, and 21%) MQWs was also studied via TRPL at 12 K and room temperature, where a biexponential carrier decay with fast and slow components was observed [92]. Recently, in 2020, a study on the mechanisms underlying the enhanced PBE in InN/$In_xGa_{(1-x)}N$ (i.e., x = 20%, 40%, 60% and 75%) MQWs was carried out using TRPL at 300 K with high carrier density [93]. An obvious extension of carrier thermalization with the longest relaxation time of 4.75 ns due to an enhanced PBE was observed. It was found that a stronger quantum confinement could effectively reduce the carrier relaxation rate by improving the elastic carrier-carrier scattering, while a larger phonon mismatch may give a higher initial carrier temperature due to the reflection of optical phonons and probably confinement of quasi-optical phonons.

In 2012, Bris et al investigated the thermalization properties in GaSb-based MQW through the Q value using intensity-dependent SSPL at different temperatures [82]. In this study, five repeated potential wells of $Ga_{0.86}In_{0.14}As_{0.12}Sb_{0.88}$ are sandwiched by lattice-matched $Al_{0.25}Ga_{0.75}As_{0.03}Sb_{0.97}$ potential barriers. A non-equilibrium hot carrier population was observed at high carrier density (i.e., above 10^{18} to 10^{19} cm^{-3}) in the MQWs. The reduced thermalization rate is attributed to the enhanced PBE, which probably depends on the carrier density, the electron-phonon interaction probability, and the phonon lifetime. The theoretical efficiency limit of HCSC using GaSb MQWs for HCA was calculated, implying that the efficiency limit can reach 50% with a Q value of 10 W K^{-1} cm^{-2} . Furthermore, the experimentally determined thermalization properties would enable an absolute efficiency improvement of 7% over p-n junctions of the same bandgap and of 1 % over the S-Q limit.

References:

[1] W. Shockley and H. J. Queisser, “Detailed Balance Limit of Efficiency of p-n Junction Solar Cells,” *J. Appl. Phys.*, vol. 32, no. 3, pp. 510–519, Mar. 1961, doi: 10.1063/1.1736034.

[2] M. A. Green, “Third generation photovoltaics: Ultra-high conversion efficiency at low cost,” *Prog. Photovoltaics Res. Appl.*, vol. 9, no. 2, pp. 123–135, Mar. 2001, doi: 10.1002/pip.360.

[3] A. Luque and A. Martí, “Increasing the Efficiency of Ideal Solar Cells by Photon Induced Transitions at Intermediate Levels,” *Phys. Rev. Lett.*, vol. 78, no. 26, pp. 5014–5017, Jun. 1997, doi: 10.1103/PhysRevLett.78.5014.

[4] R. T. Ross and A. J. Nozik, “Efficiency of hot-carrier solar energy converters,” *J. Appl. Phys.*, vol. 53, no. 5, pp. 3813–3818, May 1982, doi: 10.1063/1.331124.

[5] A. Martí and G. L. Araújo, “Limiting efficiencies for photovoltaic energy conversion in multigap systems,” *Sol. Energy Mater. Sol. Cells*, vol. 43, no. 2, pp. 203–222, Sep. 1996, doi: 10.1016/0927-0248(96)00015-3.

[6] S. R. Kurtz, P. Faine, and J. M. Olson, “Modeling of two-junction, series-connected tandem solar cells using top-cell thickness as an adjustable parameter,” *J. Appl. Phys.*, vol. 68, no. 4, pp. 1890–1895, Aug. 1990, doi: 10.1063/1.347177.

[7] K. A. Bertness, S. R. Kurtz, D. J. Friedman, A. E. Kibbler, C. Kramer, and J. M. Olson, “High-efficiency GaInP/GaAs tandem solar cells for space and terrestrial applications,” in *Proceedings of 1994 IEEE 1st World Conference on Photovoltaic Energy Conversion - WCPEC (A Joint Conference of PVSC, PVSEC and PSEC)*, 1994, vol. 2, pp. 1671–1678, doi: 10.1109/WCPEC.1994.520540.

[8] S. R. K. and J. M. O. P.K. Chiang, D.D. Krut and B.T. Cavicch, K.A. Bertness, “LARGE AREA GalnPJGaAslGe MULTIJUNCTION SOLAR CELLS,” *Renew. Energy*, pp. 2120–2123, 1994.

[9] D. J. Friedman *et al.*, “30.2% efficient GaInP/GaAs monolithic two-terminal tandem concentrator cell,” *Prog. Photovoltaics Res. Appl.*, vol. 3, no. 1, pp. 47–50, 1995, doi: 10.1002/pip.4670030105.

[10] J. G. and M. S. N. Sarah Kurtz*, y, Daryl Myers, W. E. McMahon, “A Comparison of Theoretical Efficiencies of Multi-junction Concentrator Solar Cells,” *Prog. Photovoltaics Res. Appl.*, pp. 537–546, 2008, doi: 10.1002/pip.

[11] R. R. King *et al.*, “Band-Gap-Engineered Architectures for High-Efficiencymultijunction Concentrator Solar Cells,” *24th Eur. Photovolt. Sol. Energy Conf. Exhib.*, pp. 1–7, 2009, [Online]. Available: http://scholar.googleusercontent.com/scholar?q=cache:u-8MLbxtHYUJ:scholar.google.com/+Band-gap-engineered+architectures+for+high-efficiency+multijunction+concentrator+solar+cells&hl=en&as_sdt=0,14.

[12] R. R. King *et al.*, “Band gap-voltage offset and energy production in

next-generation multijunction solar cells," *Prog. Photovoltaics Res. Appl.*, vol. 19, no. 7, pp. 797–812, Nov. 2011, doi: 10.1002/pip.1044.

[13] R. R. King *et al.*, "Solar cell generations over 40% efficiency," *Prog. Photovoltaics Res. Appl.*, vol. 20, no. 6, pp. 801–815, Sep. 2012, doi: 10.1002/pip.1255.

[14] J. F. Geisz, A. X. Levander, A. G. Norman, K. M. Jones, and M. J. Romero, "In situ stress measurement for MOVPE growth of high efficiency lattice-mismatched solar cells," *J. Cryst. Growth*, vol. 310, no. 7–9, pp. 2339–2344, Apr. 2008, doi: 10.1016/j.jcrysgro.2007.11.048.

[15] T. Takamoto, H. Washio, and H. Huso, "Application of InGaP / GaAs / InGaAs Triple Junction Solar cells to :Space Use and Concentrator Photovoltaic.," *Proc. 40 th IEEE PVSC*, pp. 5–9, 2014.

[16] Q. Y. T. U. Gosele, "Semiconductor Wafer Bonding," *Annu. Rev. Mater. Sci*, vol. 28, pp. 215–241, 1998.

[17] H. Moriceau *et al.*, "Direct Wafer Bonding Surface Conditioning," in *Handbook of Cleaning in Semiconductor Manufacturing*, Hoboken, NJ, USA: John Wiley & Sons, Inc., 2011, pp. 501–541.

[18] M. Reiche, "Semiconductor wafer bonding," *Phys. status solidi*, vol. 203, no. 4, pp. 747–759, Mar. 2006, doi: 10.1002/pssa.200564509.

[19] F. Dimroth, "New world record for solar cell efficiency at 46%.," *Presseinformation*, 2014. https://www.ise.fraunhofer.de/en/press-media/press-releases/2014/new-world-record-for-solar-cell-efficiency-at-46-percent.html#:~:text=A new world record for,Solar Energy Systems ISE%2C Germany.

[20] J. F. Geisz *et al.*, "Six-junction III–V solar cells with 47.1% conversion efficiency under 143 Suns concentration," *Nat. Energy*, vol. 5, no. 4, pp. 326–335, Apr. 2020, doi: 10.1038/s41560-020-0598-5.

[21] S.-H. Wei and A. Zunger, "Giant and Composition-Dependent Optical Bowing Coefficient in GaAsN Alloys," *Phys. Rev. Lett.*, vol. 76, no. 4, pp. 664–667, Jan. 1996, doi: 10.1103/PhysRevLett.76.664.

[22] D. B. Jackrel *et al.*, "Dilute nitride GaInNAs and GaInNAsSb solar cells by molecular beam epitaxy," *J. Appl. Phys.*, vol. 101, no. 11, p. 114916, Jun. 2007, doi: 10.1063/1.2744490.

[23] D. Derkacs, R. Jones-Albertus, F. Suarez, and O. Fidaner, "Lattice-matched multijunction solar cells employing a 1 eV GaInNAsSb bottom cell," *J. Photonics Energy*, vol. 2, no. 1, pp. 021805–1, Oct. 2012, doi: 10.1117/1.JPE.2.021805.

[24] K. Yoshikawa *et al.*, "Silicon heterojunction solar cell with interdigitated back contacts for a photoconversion efficiency over 26%," *Nat. Energy*, vol. 2, no. 5, p. 17032, May 2017, doi: 10.1038/nenergy.2017.32.

[25] T. P. White, N. N. Lal, and K. R. Catchpole, "Tandem Solar Cells Based on High-Efficiency c-Si Bottom Cells: Top Cell Requirements for >30%

Efficiency," *IEEE J. Photovoltaics*, vol. 4, no. 1, pp. 208–214, Jan. 2014, doi: 10.1109/JPHOTOV.2013.2283342.

[26] D. C. Bobela, L. Gedvilas, M. Woodhouse, K. A. W. Horowitz, and P. A. Basore, "Economic competitiveness of III–V on silicon tandem one-sun photovoltaic solar modules in favorable future scenarios," *Prog. Photovoltaics Res. Appl.*, vol. 25, no. 1, pp. 41–48, Jan. 2017, doi: 10.1002/pip.2808.

[27] R. de Lepinau *et al.*, "Direct growth of III-V nanowire-based top cell for tandem on Silicon," in *2020 47th IEEE Photovoltaic Specialists Conference (PVSC)*, Jun. 2020, vol. 2020-June, no. 111, pp. 1842–1845, doi: 10.1109/PVSC45281.2020.9300864.

[28] R. de Lépinau *et al.*, "Evidence and control of unintentional As-rich shells in GaAs 1– x P x nanowires," *Nanotechnology*, vol. 30, no. 29, p. 294003, Jul. 2019, doi: 10.1088/1361-6528/ab14c1.

[29] M. Vettori *et al.*, "Growth optimization and characterization of regular arrays of GaAs/AlGaAs core/shell nanowires for tandem solar cells on silicon," *Nanotechnology*, vol. 30, no. 8, p. 084005, Feb. 2019, doi: 10.1088/1361-6528/aaf3fe.

[30] X. Li, A. Fave, and M. Lemiti, "Si tunnel junctions obtained by proximity rapid thermal diffusion for tandem photovoltaic cells," *Semicond. Sci. Technol.*, vol. 36, no. 12, p. 125004, Dec. 2021, doi: 10.1088/1361-6641/ac2aef.

[31] E. Raoult *et al.*, "Toward a highly efficient large surface Perovskite Silicon 4-Terminal tandem module," in *2021 IEEE 48th Photovoltaic Specialists Conference (PVSC)*, Jun. 2021, pp. 0290–0293, doi: 10.1109/PVSC43889.2021.9518929.

[32] T. Nagashima, K. Okumura, K. Murata, and Y. Kimura, "Three-terminal tandem solar cells with a back-contact type bottom cell," in *Conference Record of the Twenty-Eighth IEEE Photovoltaic Specialists Conference - 2000 (Cat. No.00CH37036)*, 2000, vol. 2000-Janua, pp. 1193–1196, doi: 10.1109/PVSC.2000.916102.

[33] J.-P. Kleider *et al.*, "Summary for Policymakers," in *Climate Change 2013 – The Physical Science Basis*, Intergovernmental Panel on Climate Change, Ed. Cambridge: Cambridge University Press, 2014, pp. 1–30.

[34] P. Tockhorn *et al.*, "Three-Terminal Perovskite/Silicon Tandem Solar Cells with Top and Interdigitated Rear Contacts," *ACS Appl. Energy Mater.*, vol. 3, no. 2, pp. 1381–1392, Feb. 2020, doi: 10.1021/acsaem.9b01800.

[35] E. Veinberg-Vidal *et al.*, "Characterization of dual-junction III-V on Si tandem solar cells with 23.7% efficiency under low concentration," *Prog. Photovoltaics Res. Appl.*, vol. 27, no. 7, p. pip.3128, Apr. 2019, doi: 10.1002/pip.3128.

[36] P.-L. Nguyen *et al.*, "New Architecture and Bonding Process for III-V//Si Tandem Solar Cells," in *OSA Advanced Photonics Congress 2021*, 2021, p. PvW1E.4, doi: 10.1364/PVLED.2021.PvW1E.4.

[37] A. Ben Slimane *et al.*, "1.73 eV AlGaAs/InGaP heterojunction solar cell grown

by MBE with 18.7% efficiency," *Prog. Photovoltaics Res. Appl.*, vol. 28, no. 5, pp. 393–402, May 2020, doi: 10.1002/pip.3249.

[38] J. F. Geisz and D. J. Friedman, "III N V semiconductors for solar photovoltaic applications," *Semicond. Sci. Technol.*, vol. 17, no. 8, pp. 769–777, Aug. 2002, doi: 10.1088/0268-1242/17/8/305.

[39] C. Ratcliff, T. J. Grassman, J. A. Carlin, D. J. Chmielewski, and S. A. Ringel, "Ga-rich Ga x In 1-x P solar cells on Si with 1.95 eV bandgap for ideal III-V/Si photovoltaics," in *Physics, Simulation, and Photonic Engineering of Photovoltaic Devices III*, Mar. 2014, vol. 8981, p. 898118, doi: 10.1117/12.2042017.

[40] S. Almosni *et al.*, "Correlations between electrical and optical properties in lattice-matched GaAsPN/GaP solar cells," *Sol. Energy Mater. Sol. Cells*, vol. 147, pp. 53–60, Apr. 2016, doi: 10.1016/j.solmat.2015.11.036.

[41] Y. Ping Wang *et al.*, "Abrupt GaP/Si hetero-interface using bistepped Si buffer," *Appl. Phys. Lett.*, vol. 107, no. 19, p. 191603, Nov. 2015, doi: 10.1063/1.4935494.

[42] O. Durand *et al.*, "Monolithic Integration of Diluted-Nitride III–V-N Compounds on Silicon Substrates: Toward the III–V/Si Concentrated Photovoltaics," *Energy Harvest. Syst.*, vol. 1, no. 3–4, pp. 147–156, Jan. 2014, doi: 10.1515/ehs-2014-0008.

[43] M. J. Archer *et al.*, "GaInP⁄GaAs dual junction solar cells on Ge⁄Si epitaxial templates," *Appl. Phys. Lett.*, vol. 92, no. 10, p. 103503, Mar. 2008, doi: 10.1063/1.2887904.

[44] Y. Takagi, Y. Furukawa, A. Wakahara, and H. Kan, "Lattice relaxation process and crystallographic tilt in GaP layers grown on misoriented Si(001) substrates by metalorganic vapor phase epitaxy," *J. Appl. Phys.*, vol. 107, no. 6, p. 063506, Mar. 2010, doi: 10.1063/1.3310479.

[45] Y. Furukawa *et al.*, "Control of N Content of GaPN Grown by Molecular Beam Epitaxy and Growth of GaPN Lattice Matched to Si(100) Substrate," *Jpn. J. Appl. Phys.*, vol. 41, no. Part 1, No. 2A, pp. 528–532, Feb. 2002, doi: 10.1143/JJAP.41.528.

[46] N. Sommer *et al.*, "Growth of (BGa)As, (BGa)P, (BGa)(AsP) and (BGaIn)P by MOVPE," *J. Cryst. Growth*, vol. 370, pp. 191–196, 2013, doi: 10.1016/j.jcrysgro.2012.07.035.

[47] I. Németh, B. Kunert, W. Stolz, and K. Volz, "Heteroepitaxy of GaP on Si: Correlation of morphology, anti-phase-domain structure and MOVPE growth conditions," *J. Cryst. Growth*, vol. 310, no. 7–9, pp. 1595–1601, 2008, doi: 10.1016/j.jcrysgro.2007.11.127.

[48] B. Kunert, I. Németh, S. Reinhard, K. Volz, and W. Stolz, "Si (001) surface preparation for the antiphase domain free heteroepitaxial growth of GaP on Si substrate," *Thin Solid Films*, vol. 517, no. 1, pp. 140–143, Nov. 2008, doi: 10.1016/j.tsf.2008.08.077.

[49] O. Skibitzki *et al.*, “GaP collector development for SiGe heterojunction bipolar transistor performance increase: A heterostructure growth study,” *J. Appl. Phys.*, vol. 111, no. 7, p. 073515, Apr. 2012, doi: 10.1063/1.3701583.

[50] H. Kroemer, “POLAR-ON-NONPOLAR EPITAXY,” *J. Cryst. Growth*, vol. 81, no. 1–4, pp. 193–204, 1987, [Online]. Available: https://doi.org/10.1016/0022-0248(87)90391-5.

[51] L. Chen *et al.*, “Epitaxial III–V/Si Vertical Heterostructures with Hybrid 2D-Semimetal/Semiconductor Ambipolar and Photoactive Properties,” *Adv. Sci.*, vol. 9, no. 2, p. 2101661, Jan. 2022, doi: 10.1002/advs.202101661.

[52] C. R. Allen, J.-H. Jeon, and J. M. Woodall, “Simulation assisted design of a gallium phosphide n–p photovoltaic junction,” *Sol. Energy Mater. Sol. Cells*, vol. 94, no. 5, pp. 865–868, May 2010, doi: 10.1016/j.solmat.2010.01.009.

[53] C. R. Allen, J. M. Woodall, and J.-H. Jeon, “Results of a gallium phosphide photovoltaic junction with an AR coating under concentration of natural sunlight,” *Sol. Energy Mater. Sol. Cells*, vol. 95, no. 9, pp. 2655–2658, Sep. 2011, doi: 10.1016/j.solmat.2011.05.034.

[54] M. Vaisman, S. Tomasulo, T. Masuda, J. R. Lang, J. Faucher, and M. L. Lee, “Effects of growth temperature and device structure on GaP solar cells grown by molecular beam epitaxy,” *Appl. Phys. Lett.*, vol. 106, no. 6, p. 063903, Feb. 2015, doi: 10.1063/1.4908181.

[55] X. Lu *et al.*, “Wide Band Gap Gallium Phosphide Solar Cells,” *IEEE J. Photovoltaics*, vol. 2, no. 2, pp. 214–220, Apr. 2012, doi: 10.1109/JPHOTOV.2011.2182180.

[56] P. J. Dean, G. Kaminsky, and R. B. Zetterstrom, “Intrinsic Optical Absorption of Gallium Phosphide between 2.33 and 3.12 eV,” *J. Appl. Phys.*, vol. 38, no. 9, pp. 3551–3556, Aug. 1967, doi: 10.1063/1.1710170.

[57] J. F. Geisz, J. M. Olson, M. J. Romero, C. s. Jiang, and A. G. Norman, “Lattice-mismatched GaAsP Solar Cells Grown on Silicon by OMVPE,” in *2006 IEEE 4th World Conference on Photovoltaic Energy Conference*, May 2006, vol. 1, pp. 772–775, doi: 10.1109/WCPEC.2006.279570.

[58] K. N. Yaung, J. R. Lang, and M. L. Lee, “Towards high efficiency GaAsP solar cells on (001) GaP/Si,” *2014 IEEE 40th Photovolt. Spec. Conf. PVSC 2014*, no. 001, pp. 831–835, 2014, doi: 10.1109/PVSC.2014.6925043.

[59] M. Vaisman *et al.*, “15.3%-Efficient GaAsP Solar Cells on GaP/Si Templates,” *ACS Energy Lett.*, vol. 2, no. 8, pp. 1911–1918, Aug. 2017, doi: 10.1021/acsenergylett.7b00538.

[60] S. Tomasulo, K. N. Yaung, and M. L. Lee, “Metamorphic GaAsP and InGaP Solar Cells on GaAs,” *IEEE J. Photovoltaics*, vol. 2, no. 1, pp. 56–61, Jan. 2012, doi: 10.1109/JPHOTOV.2011.2177640.

[61] T. Milakovich, R. Shah, S. Hadi, M. Bulsara, A. Nayfeh, and E. Fitzgerald, “Growth and characterization of GaAsP top cells for high efficiency III–V/Si tandem PV,” in *2015 IEEE 42nd Photovoltaic Specialist Conference (PVSC)*,

Jun. 2015, pp. 1–4, doi: 10.1109/PVSC.2015.7355598.

[62] K. Hayashi, T. Soga, H. Nishikawa, T. Jimbo, and M. Umeno, “MOCVD growth of GaAsP on Si for tandem solar cell application,” in *Proceedings of 1994 IEEE 1st World Conference on Photovoltaic Energy Conversion - WCPEC (A Joint Conference of PVSC, PVSEC and PSEC)*, 1994, vol. 2, pp. 1890–1893, doi: 10.1109/WCPEC.1994.520736.

[63] M. Diaz *et al.*, “Dual-junction GaAsP/SiGe on silicon tandem solar cells,” in *2014 IEEE 40th Photovoltaic Specialist Conference (PVSC)*, Jun. 2014, pp. 0827–0830, doi: 10.1109/PVSC.2014.6925042.

[64] F. Dimroth *et al.*, “Comparison of Direct Growth and Wafer Bonding for the Fabrication of GaInP/GaAs Dual-Junction Solar Cells on Silicon,” *IEEE J. Photovoltaics*, vol. 4, no. 2, pp. 620–625, Mar. 2014, doi: 10.1109/JPHOTOV.2014.2299406.

[65] I. A. Buyanova *et al.*, “Direct experimental evidence for unusual effects of hydrogen on the electronic and vibrational properties of GaNxP1−x alloys: A proof for a general property of dilute nitrides,” *Phys. Rev. B*, vol. 70, no. 24, p. 245215, Dec. 2004, doi: 10.1103/PhysRevB.70.245215.

[66] X. Liu, S. G. Bishop, J. N. Baillargeon, and K. Y. Cheng, “Band gap bowing in GaP 1− x N x alloys,” *Appl. Phys. Lett.*, vol. 63, no. 2, pp. 208–210, Jul. 1993, doi: 10.1063/1.110371.

[67] G. Y. Rudko, I. A. Buyanova, W. M. Chen, H. P. Xin, and C. W. Tu, “Temperature dependence of the GaNxP1−x band gap and effect of band crossover,” *Appl. Phys. Lett.*, vol. 81, no. 21, pp. 3984–3986, Nov. 2002, doi: 10.1063/1.1522496.

[68] H. P. Xin, R. J. Welty, and C. W. Tu, “GaN0.011P0.989 red light-emitting diodes directly grown on GaP substrates,” *Appl. Phys. Lett.*, vol. 77, no. 13, pp. 1946–1948, Sep. 2000, doi: 10.1063/1.1311957.

[69] H. Yaguchi *et al.*, “Photoluminescence excitation spectroscopy of GaP1−N alloys: conduction-band-edge formation by nitrogen incorporation,” *J. Cryst. Growth*, vol. 170, no. 1–4, pp. 353–356, Jan. 1997, doi: 10.1016/S0022-0248(96)00592-1.

[70] S. Sukrittanon *et al.*, “Enhanced conversion efficiency in wide-bandgap GaNP solar cells,” *Appl. Phys. Lett.*, vol. 107, no. 15, p. 153901, Oct. 2015, doi: 10.1063/1.4933317.

[71] C. Robert, M. Perrin, C. Cornet, J. Even, and J. M. Jancu, “Atomistic calculations of Ga(NAsP)/GaP(N) quantum wells on silicon substrate: Band structure and optical gain,” *Appl. Phys. Lett.*, vol. 100, no. 11, p. 111901, Mar. 2012, doi: 10.1063/1.3694028.

[72] J. F. Geisz, D. J. Friedman, and S. Kurtz, “GaNPAs solar cells lattice-matched to GaP,” in *Conference Record of the Twenty-Ninth IEEE Photovoltaic Specialists Conference, 2002.*, 2002, pp. 864–867, doi: 10.1109/PVSC.2002.1190716.

[73] J. Geisz *et al.*, “Growth and Characterization of GaPNAs on Si,” *MRS Proc.*, vol.

799, no. 001, p. Z1.10, Feb. 2003, doi: 10.1557/PROC-799-Z1.10.

[74] J. F. Geisz, J. M. Olson, D. J. Friedman, K. M. Jones, R. C. Reedy, and M. J. Romero, “Lattice-matched GaNPAs-on-silicon tandem solar cells,” in *Conference Record of the Thirty-first IEEE Photovoltaic Specialists Conference, 2005.*, 2005, pp. 695–698, doi: 10.1109/PVSC.2005.1488226.

[75] C. Cornet *et al.*, “Preferential incorporation of substitutional nitrogen near the atomic step edges in diluted nitride alloys,” *Appl. Phys. Lett.*, vol. 101, no. 25, p. 251906, Dec. 2012, doi: 10.1063/1.4772785.

[76] J. Kuyyalil *et al.*, “Nitrogen–phosphorus competition in the molecular beam epitaxy of GaPN,” *J. Cryst. Growth*, vol. 377, pp. 17–21, Aug. 2013, doi: 10.1016/j.jcrysgro.2013.04.052.

[77] H. Jussila *et al.*, “Substitutionality of nitrogen atoms and formation of nitrogen complexes and point defects in GaPN alloys,” *J. Phys. D. Appl. Phys.*, vol. 47, no. 7, p. 075106, Feb. 2014, doi: 10.1088/0022-3727/47/7/075106.

[78] A. Aho *et al.*, “Composition dependent growth dynamics in molecular beam epitaxy of GaInNAs solar cells,” *Sol. Energy Mater. Sol. Cells*, vol. 124, pp. 150–158, May 2014, doi: 10.1016/j.solmat.2014.01.044.

[79] S. Fahy and E. P. O’Reilly, “Intrinsic limits on electron mobility in dilute nitride semiconductors,” *Appl. Phys. Lett.*, vol. 83, no. 18, pp. 3731–3733, Nov. 2003, doi: 10.1063/1.1622444.

[80] K. Jandieri *et al.*, “Nonexponential photoluminescence transients in a Ga(NAsP) lattice matched to a (001) silicon substrate,” *Phys. Rev. B*, vol. 87, no. 3, p. 035303, Jan. 2013, doi: 10.1103/PhysRevB.87.035303.

[81] S. R. Kurtz, A. A. Allerman, C. H. Seager, R. M. Sieg, and E. D. Jones, “Minority carrier diffusion, defects, and localization in InGaAsN, with 2% nitrogen,” *Appl. Phys. Lett.*, vol. 77, no. 3, pp. 400–402, 2000, doi: 10.1063/1.126989.

[82] A. Le Bris, L. Lombez, S. Laribi, G. Boissier, P. Christol, and J.-F. Guillemoles, “Thermalisation rate study of GaSb-based heterostructures by continuous wave photoluminescence and their potential as hot carrier solar cell absorbers,” *Energy Environ. Sci.*, vol. 5, no. 3, p. 6225, 2012, doi: 10.1039/c2ee02843c.

[83] P. Y. Yu and M. Cardona, “Electronic Properties of Defects,” in *Fundamentals of Semiconductors*, Berlin, Heidelberg: Springer Berlin Heidelberg, 1996, pp. 149–192.

[84] P. Würfel, “Solar energy conversion with hot electrons from impact ionisation,” *Sol. Energy Mater. Sol. Cells*, vol. 46, no. 1, pp. 43–52, Apr. 1997, doi: 10.1016/S0927-0248(96)00092-X.

[85] F. Chen, A. N. Cartwright, H. Lu, and W. J. Schaff, “Time-resolved spectroscopy of recombination and relaxation dynamics in InN,” *Appl. Phys. Lett.*, vol. 83, no. 24, pp. 4984–4986, Dec. 2003, doi: 10.1063/1.1633973.

[86] D.-J. Jang, G.-T. Lin, C.-L. Wu, C.-L. Hsiao, L. W. Tu, and M.-E. Lee, “Energy relaxation of InN thin films,” *Appl. Phys. Lett.*, vol. 91, no. 9, p. 092108, Aug.

2007, doi: 10.1063/1.2773947.

[87] C. M. Collier, B. Born, X. Jin, and J. F. Holzman, "Ultrafast charge-carrier and phonon dynamics in GaP," *Appl. Phys. Lett.*, vol. 103, no. 7, p. 072106, Aug. 2013, doi: 10.1063/1.4818664.

[88] Z. Y. Xu and C. L. Tang, "Picosecond relaxation of hot carriers in highly photoexcited bulk GaAs and GaAs-AlGaAs multiple quantum wells," *Appl. Phys. Lett.*, vol. 44, no. 7, pp. 692–694, Apr. 1984, doi: 10.1063/1.94880.

[89] A. J. Nozik, C. A. Parsons, D. J. Dunlavy, B. M. Keyes, and R. K. Ahrenkiel, "Dependence of hot carrier luminescence on barrier thickness in GaAs/AlGaAs superlattices and multiple quantum wells," *Solid State Commun.*, vol. 75, no. 4, pp. 297–301, Jul. 1990, doi: 10.1016/0038-1098(90)90900-V.

[90] G. Conibeer, Y. Zhang, S. P. Bremner, and S. Shrestha, "Towards an understanding of hot carrier cooling mechanisms in multiple quantum wells," *Jpn. J. Appl. Phys.*, vol. 56, no. 9, p. 091201, Sep. 2017, doi: 10.7567/JJAP.56.091201.

[91] X. Zhang, D. H. Rich, J. T. Kobayashi, N. P. Kobayashi, and P. D. Dapkus, "Carrier relaxation and recombination in an InGaN/GaN quantum well probed with time-resolved cathodoluminescence," *Appl. Phys. Lett.*, vol. 73, no. 10, pp. 1430–1432, Sep. 1998, doi: 10.1063/1.121966.

[92] S.-W. Feng *et al.*, "Dynamic carrier relaxation in InGaN/GaN multiple quantum well structures," Jun. 2002, vol. 4643, p. 169, doi: 10.1117/12.470417.

[93] Y. Zhang, L. Tang, B. Zhang, P. Wang, and C. Xu, "Quantitative study on the mechanisms underlying the phonon bottleneck effect in InN/InGaN multiple quantum wells," *Appl. Phys. Lett.*, vol. 116, no. 10, p. 103104, Mar. 2020, doi: 10.1063/5.0003201.

Chapter 2 Manufacturing, characterization and modeling of solar cells

This chapter is a presentation of the manufacturing and characterization work of the solar cells developed at FOTON before and during this thesis. We first describe the MBE frame that is used for solar cell growth, carried out by Tony Rohel, Rozenn Gautheron-Bernard, Maud Jullien, Charles Cornet, Nicolas Bertru and Nicolas Chevalier. We also introduced in detail the technological steps of manufacturing functional solar cells carried out in collaboration with Karine Tavernier and Alexandre Beck. Then, we present different ways to characterize the solar cells and the information that can be extracted from them. These characterizations were made in collaboration with Antoine Létoublon and Julien Lapeyre (X-ray diffraction) and Karine Tavernier (cleanroom). Two molecular beam epitaxy chambers have been used for the heterostructures growth: a solid source MBE (SSMBE) for the epitaxy of GaP-based on silicon substrates (tandem cells development), and a gas source MBE (GSMBE) for the elaboration of the HCSC on InP substrates. The development of the GaAsPN/Si-based tandem cells has been initiated during the thesis of Samy Almosni (2011-2015) and Mickael Da Silva (2014-2018) in FOTON.

2.1. Manufacturing of GaAsPN/Si tandem solar cells at Institut FOTON

2.1.1. MBE growth of GaP-based heterostructures on silicon substrates

Growing the III-V materials on Si should be done in separate chambers to avoid pollution from each other. In fact, Si is a dopant for III-V materials, and vice versa.
The first two-chamber MBE system for integration on Si by pseudomorphic growth was installed at the Toyohashi University of Technology in Japan, and it consists of two MBE chambers connected by an ultra-high vacuum (UHV) transfer chamber. This two-chamber system enabled them to demonstrate a drastic reduction in reciprocal doping between III-V and Si compared with the growth carried out in a single chamber [1].

Later, Philipps Marburg University in Germany proposed a growth cluster combining two MOVPE chambers for Si and III-V with a transfer chamber under controlled atmosphere. The group of James S. Harris at Stanford also developed a cluster made up of two MBE Varian Mod Gen II chambers connected by a transfer tunnel under UHV.

Our laboratory also has a double-chamber connected by a UHV tunnel dedicated to research on silicon photonics. This is a RIBER system combining a MBE chamber for III-V materials with a UHVCVD (ultra-high-vacuum chemical vapor deposition) chamber for Si (see Fig. 2-1).

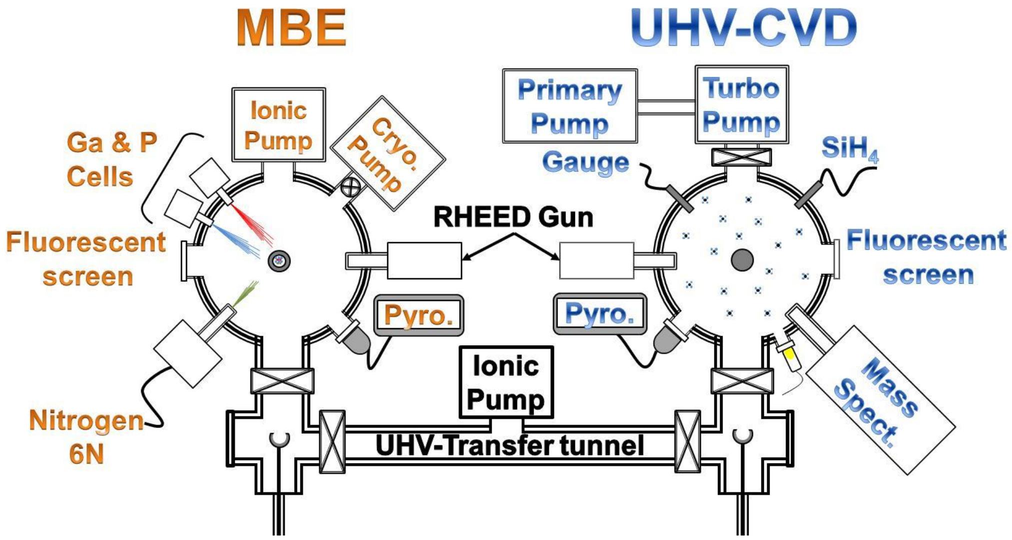

Fig. 2-1: UHVCVD-MBE growth cluster for III-V integration on Si

2.1.1.1. UHV-CVD growth cluster

The UHV-CVD reactor is connected to pumping systems to achieve vacuum values of 10^{-1} to 10^{-10} Torr. The pressure is measured by a filament gauge for pressures between 10^{-10} and 10^{-5} Torr and by a capacitive CTR gauge between 10^{-5} and 10^{-1} Torr. The 2 inch diameter silicon wafers are placed on a molybdenum support after being cleaned ex-situ. The substrate support is heated on the rear face by a graphite resistor coated with pyrolytic boron nitride and supplied by a dedicated Eurotherm 900 generator. The temperature of the substrate is measured by a Eurotherm thermocouple and an infrared fiber pyrometer between 575℃ and 1000℃. A mass spectrometer is connected to the reactor to detect the different substances emitted during the degassing of the substrate. The silane (SiH_4) and the hydrogen are injected by a pressure controller which allows the pressure / flow rate to be adjusted from 0.001 to 10 Torr before entering into the reactor.

There are several reasons for choosing CVD for the silicon growth. First of all, compared to other techniques, CVD allows the growth of thicker layers with well-controlled doping levels, which is an important point in the context of integrated silicon photonics, especially for the possible development of a sub-cell in Si for a tandem cell. In addition, the use of hydrogenated molecules improves the mobility of substances on the surface during growth [2]. Finally, the control of the organization of the moving atoms on the surface during growth is facilitated compared to MBE [3]–[6]. However, it is essential to have a mono-domain silicon presenting diatomic steps in order to then resume the growth of GaP on Si without generating APD (anti-phase domain).

2.1.1.2. MBE frame

In regards to the growth of the III-V compounds, the MBE frame is used. Elements III (Ga, In, Al) are obtained using conventional Knudsen effusion cells containing pure solid metal sources while elements V (P, As, Sb) are provided by valve cracking cells in which these solid elements are heated. Under the heat, phosphorus and arsenic are released in the form of tetramers (P_4, As_4) and cracked to form the P_2 and As_2 dimers which have better adsorption coefficients [7], [8]. The valves at the outlet of the cells are under good flow control. Growth fluxes are in the range of 10^{-7} to 10^{-5} Torr, while the residual pressure in the frame reached 10^{-11} Torr. The growth rate of compound III-V is controlled by the flow of element III.

The choice of a III-V material growth by MBE is explained by the possibility of finely controlling the thicknesses, the interfaces and the compositions and therefore of producing high quality monocrystalline materials. In addition, growth by MBE taking place under conditions very far from thermodynamic equilibrium, it is very suitable for the production of metastable materials such as diluted nitrogen [9], [10]. MBE operates in an ultra-high vacuum environment where the fluxes of atoms and molecules are directed to a crystalline substrate. These atomic/molecular substances are adsorbed to the surface to either form bonds with the epitaxial crystal or be desorbed if the temperature is too high or if there is no space available to form a bond. The flows are generated by evaporation or sublimation of solid sources of very high purity, which limits the residual doping. When growing with MBE, the pressure can reach around 10^{-5} Torr. The distance between the sources and the substrate is of the order of 30 to 50 cm, which remains much less than the average free path of the substances deposited at this pressure. The fluxes of atoms/molecules can be considered as beams because they do not encounter any collisions with other substances on their way to the substrate. Growth rate are low (<1 µm / h) compared to other growth techniques. As a layer grows, sources that do not come into use are mechanically obstructed by a shutter. Thanks to the slow growth rates, the shutter closing time is much shorter than the formation time of a monatomic layer. This guarantees to obtain abrupt interfaces which are essential for making tunnel diodes or for precisely controlling the thicknesses and compositions of nanostructures.

The MBE frame of the FOTON laboratory also includes an ADDON RF plasma source for the growth of diluted nitrides (GaPN, GaAsPN, etc.). Ultra pure nitrogen gas is injected into the cell via a mass flow regulator for precise control of the gas flow. A plasma is generated by a copper antenna which emits a radiofrequency electromagnetic wave (f = 13.7 MHz). Different chemical substances can be generated in the plasma: electrons, atomic nitrogen, metastable N_2^+ ions [11]–[14]. To reduce the impact of high-energy charged particles, which are known to damage epitaxial layers, a movable valve is installed at the outlet of the plasma cavity. This configuration blocks the propagation of these charged substances to the substrate (and thus prevents for example, the appearance of various point defects). A diagram of the plasma cell is shown in Fig. 2-2.

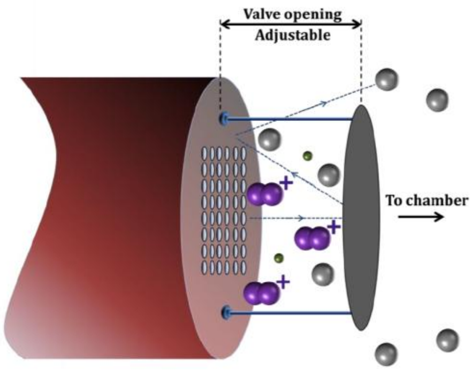

Fig. 2-2: Diagram of the ADDON RF plasma cell.

The opening of the valve is adjustable to increase or decrease the amount of atomic nitrogen sent into the frame. The parameters of the plasma cell which influence the nitrogen incorporation are: the power of the radio frequencies, the nitrogen flux and the opening of the valve. Depending on these parameters, there are two modes of operation of the cell:

- Low brightness mode under medium power (<350W) and strong N flux (>1.5 sccm). This mode produces relatively little monatomic nitrogen.
- High brightness mode under high power (>350W) and low N flux (<0.7 sccm). This mode is preferred for the incorporation of nitrogen because it guarantees a very efficient production of monatomic nitrogen.

A rigorous analysis of the optical emission spectrum of nitrogen plasma was carried out in the laboratory before the start of this thesis to optimize the operating parameters of the plasma cell [15].

2.1.2. Manufacture of cell-architectures

2.1.2.1. Technological processes for the manufacture of the GaP/Si-based solar cells

After the crystal growth of PIN junctions, they must be formed and the ohmic contacts must be made to finalize the component. We present here the technological steps to fabricate our photovoltaic cells in the cleanroom. Firstly, a brief description of each process involved. Then, the fabrication steps are listed for two types of architecture: 5.25 x 5.25 mm^2 cells with comb-shaped contacts on the front face and solid contacts on the back ("top-bottom"); and 365 x 290 μm^2 cells with both contacts on the front face ("top-top").

Technological processes involved:

i. Anneal RTA: Rapid thermal anneal (RTA) in rapid thermal processing is a process used in semiconductor device fabrication which involves heating a single wafer at a time in order to affect its electrical properties. Unique heat treatments are designed for different effects. Wafers can be heated in order to activate dopants, change film-to-film or film-to-wafer substrate interfaces, densify deposited films, change states of grown films, repair damage from ion implantation, move dopants or drive dopants from one film into another or from a film into the wafer substrate. The dilute GaAsP acting as the top cell absorber should exhibit optimal electrical and optical properties. However, dilute nitrides are metastable alloys with large miscibility gaps and they are known for localized defects of various natures generated during their growth, especially at low temperature. For example, element Ga (III) vacancies, AsGa anti-sites and interstitial nitrogen which tends to cluster together in so-called "nitrogen clusters" [16]–[18]. Thermal annealing treatments are often used to reduce the density of these defects in the crystal [19], [20].

Fig. 2-3: Jipelec JETFIRST RTA Furnace.

The rapid thermal annealing (RTA) furnace used at FOTON to improve the properties of GaAsP after growth is a JIPELEC JetFirst apparatus shown in Fig. 2-3. The device is also used to anneal the ohmic contacts of the cells.

ii. Lithography: Lithography is used to define the shape of the metal contacts on the cells. It is also used to define and isolate the cells on the same substrate by chemical etching. It consists of coating the sample with photosensitive resin by centrifugation and annealing the resin. Then the substrate is exposed under UV light through a mask to define the patterns in the resin. This step is performed in a Karl Suss MJB4 aligner. Finally, the resin is developed in a solvent to show the patterns: the areas exposed/unexposed to UV react with the solvent and dissolve in the case of positive/negative resin respectively.

iii. Deposition of the metal contacts: The metal contacts are deposited on the cell in an electron beam evaporator under vacuum. The power of the beam is calibrated to correspond to a deposition rate (of an order of a few angstroms per second) and the deposited thickness is controlled by using a piezoelectric crystal. The Ti/Pt/Au (p contact) and Ni/Au/Ge (n contact) sequences are deposited on the substrate after a deoxidation step in a 5% hydrofluoric acid solution. In the case of p contact (on the front face of the cell in our case), the contact pattern is shown by lift-off by dissolving the resin from the lithography step in a hot acetone bath.

iv. Etching: Etching is essential for photovoltaics and LEDs, because it makes it possible to isolate each cell in the form of a mesa and to avoid strong leakage current in reverse bias. Our large size cells (5.25 x 5.25 mm^2) are compatible with chemical solution etching techniques. The GaP etching is relatively little referenced in the literature. We use a solution of HCl : H_2O : H_2O_2 = 40 : 1 : 2.

2.1.2.1.a. Top-Bottom contacts

The top-bottom contacts, fabricated by the process shown in Fig. 2-4, corresponds to a typical design of photovoltaic cells (area: 5.25 x 5.25 mm^2). This design has been used particularly to characterize mono-junction cells on GaP and complete tandem structures on silicon (more details on the geometry of the contacts are shown in Chapter 3).

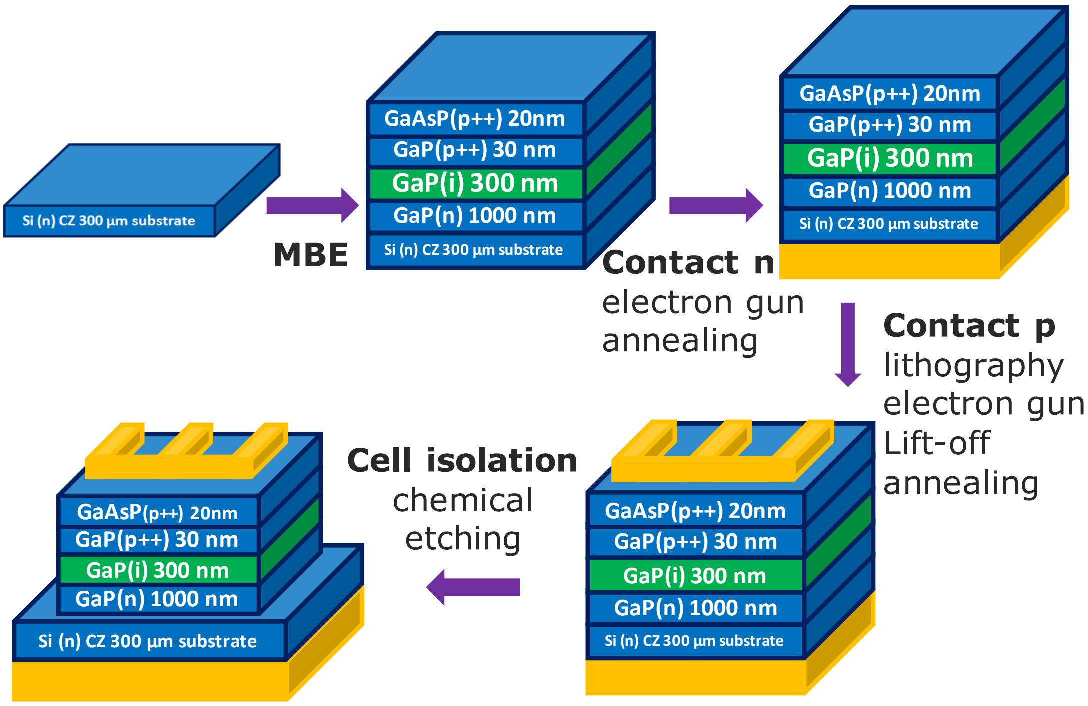

Fig. 2-4: Technological steps at FOTON to manufacture GaP-based cells in the case of “top-bottom” contacts.

2.1.2.1.b. Top-Top contacts

The top-top contacts, fabricated by the process shown in Fig. 2-5, are used to characterize single-junction cells grown on a Si substrate. These structures initially validated the growth of GaP-based cells on Si without suffering from the absence of a tunnel junction and optimize the band lineup between GaP and the Si substrate (more details on the geometry of the contacts are shown in Chapter 3).

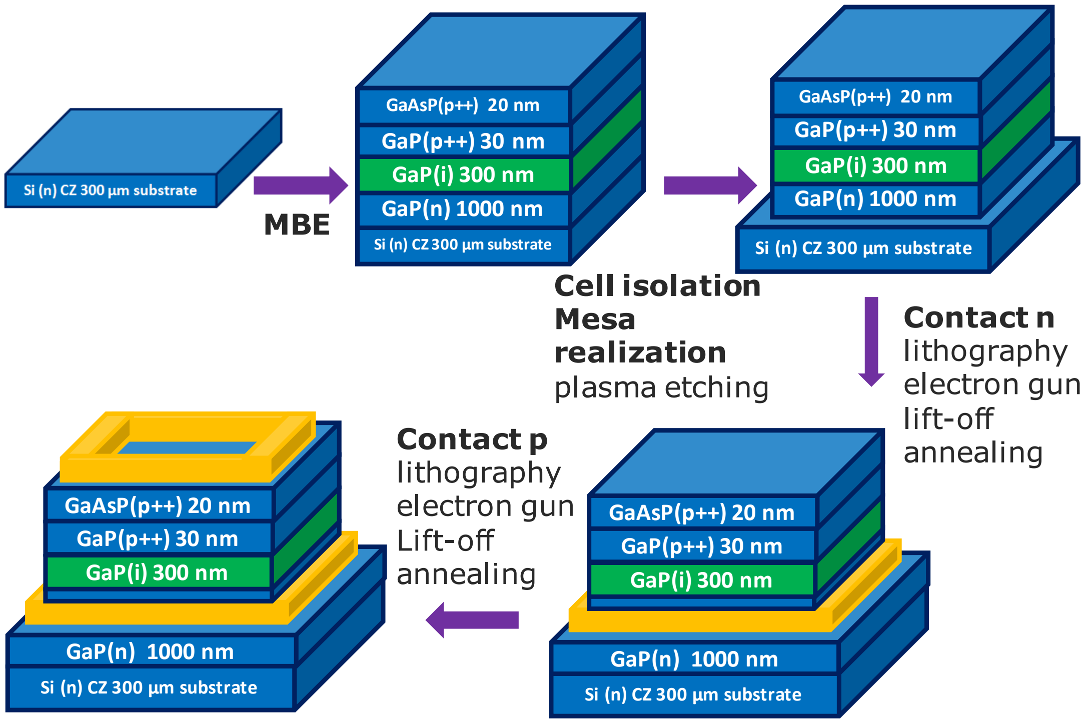

Fig. 2-5: Technological steps at FOTON to manufacture GaP-based cells in the case of "top-top" contacts.

2.2. Manufacturing of Hot carrier Solar Cells on InP substrates at Institut FOTON

2.2.1. MBE growth of HCSC on InP substrates

The growth of the HCSC is carried out by Gas Source molecular beam epitaxy (GSMBE). The equipment used is shown in the following figure 2-6:

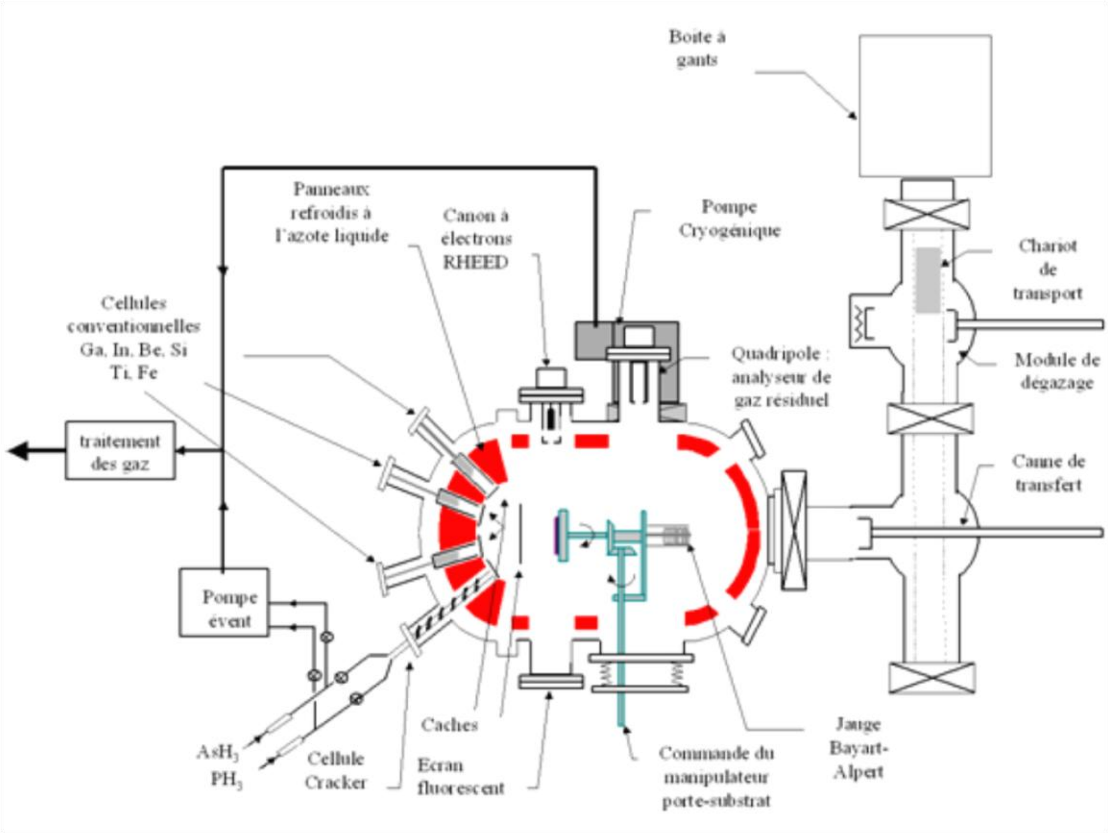

Fig. 2-6: RIBER 2300 GSMBE growth chamber.

The growth is performed in an ultra-high vacuum (UHV) growth chamber which displays a vacuum lower than 10^{-10} Torr. The vacuum is achieved by means of turbo-molecular, ionic and cryogenic pumps. The cooling of the cold panel with a continuous circulation of liquid nitrogen allows to improve the quality of the residual vacuum by condensation of the gas molecules. The epitaxy system includes three chambers allowing, through airlocks, to introduce or remove samples without breaking the vacuum regime in the deposition chamber. Indeed, obtaining a vacuum of 10^{-10} Torr after opening, requires a bake-out during about one week.

The low pressure during growth ($P < 10^{-4}$ Torr) allows to obtain mean free paths of the molecules larger than the source-substrate distance, which is the meaning of the term “molecular beam”.

The GSMBE is well suited for the growth of InP-based [(Ga)In(As)P alloys] heterostructures. It has solid sources of III elements (In, Ga) and dopants such as Si (n-doping) and Be (p-doping), and a gas source for V elements (As, P).

The control of the solid sources heating temperature allows to control the molecular or atomic fluxes of III elements and dopants. The fluxes of V elements (As and P) are obtained from gas sources composed of a cracker which carries out the thermal decomposition (T 900℃) of the AsH_3 and PH_3 molecules into As_2 and P_2 molecules. Dimeric molecules have the advantage of having a higher bonding coefficient than tetrameric molecules. The control of the flow rates and thus of the fluxes of the V elements is ensured by mass flow meters.

The substrate is heated according to the three-temperature method allowing the stoichiometric growth of III-V compounds ($T_{III} > T_{sub} > T_V$). Indeed, the evaporation temperatures of the III elements are significantly higher than those of the substrate and those of the V elements. The III elements therefore condense on the substrate with a bonding coefficient close to unity. The V elements incorporate only in the presence of III elements. The excess flow of V elements is re-evaporated. The normal growth condition corresponds to a “stabilized V surface”. In this case, the growth rate and the III element composition (for an alloy) are controlled by the III element fluxes. The V-element incorporation coefficients are low (<< 1) and depend strongly on the growth conditions. Controlling the V-element composition of an alloy such as GaInAsP requires a systematic calibration for each material. This is done through dedicated calibration samples measured by High-resolution X-ray diffraction.

Finally, in-situ monitoring of the growth surface is allowed through RHEED (Reflection High-Energy Electron Diffraction). The observation of the RHEED pattern allows to follow the deoxidation of the surface before growth or to follow the surface morphology (2D or 3D) and to determine the surface reconstructions, characteristic of the growth mode (stabilized V or stabilized III). The recording of the oscillations of the intensity of the specular spot makes it possible to measure the growth rates and the composition in elements III of the alloys.

2.2.2. Technological processes for the manufacture of the hot carrier solar cells

This part details the fabrication process of HCSCs, each fabrication steps will be presented. As soon as each step is validated, the first set of HCSC samples are characterized and analyzed (see more in chapter 4).

The first structure studied in this chapter (Fig. 2-6) is composed of a 50nm-thick InGaAs absorber sandwiched with two AlInAs barriers on a (001)-oriented InP substrate, with a 300nm thick InGaAs buffer layer surmounted by a 50nm thick InP layer. The top of the heterostructure is composed of a 100nm heavily p-doped InGaAs contact layer on a p+ InGaAs layer. Therefore, the selective contact for the electrons in this first structure is an AlInAs barrier, acting as a high-pass filter.

The second structure studied in this chapter (Fig. 2-7) has the same structure as the first one but with a selective contact for the electrons composed of a single quantum well (SQW) (13nm thick AlInAs/4nm thick InGaAs/13nm thick AlInAs).
(AlInAs/InGaAs/AlInAs) and the 50nm InGaAs absorber.

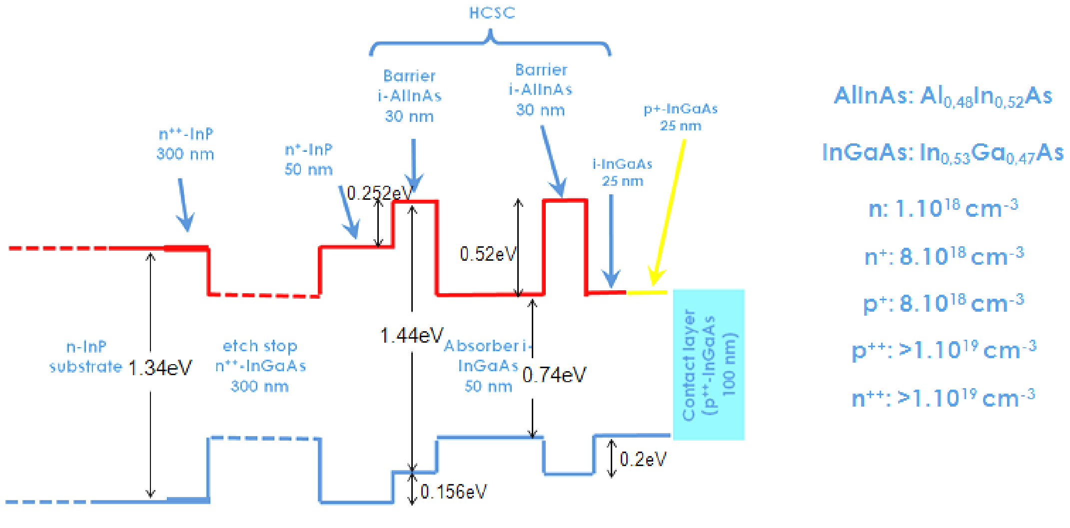

Fig. 2-6: Very simplified structure and energy diagram (at 300K) of HCSC (selective Barrier contact). AlInAs: $Al_{0,48}In_{0,52}As$; InGaAs: $In_{0,53}Ga_{0,47}As$; n: 1.10^{18} cm^{-3}; n^{+}: 8.10^{18} cm^{-3}; p^{+}: 8.10^{18} cm^{-3}; p^{++}: $>1.10^{19}$ cm^{-3}; n^{++}: $>1.10^{19}$ cm^{-3}.

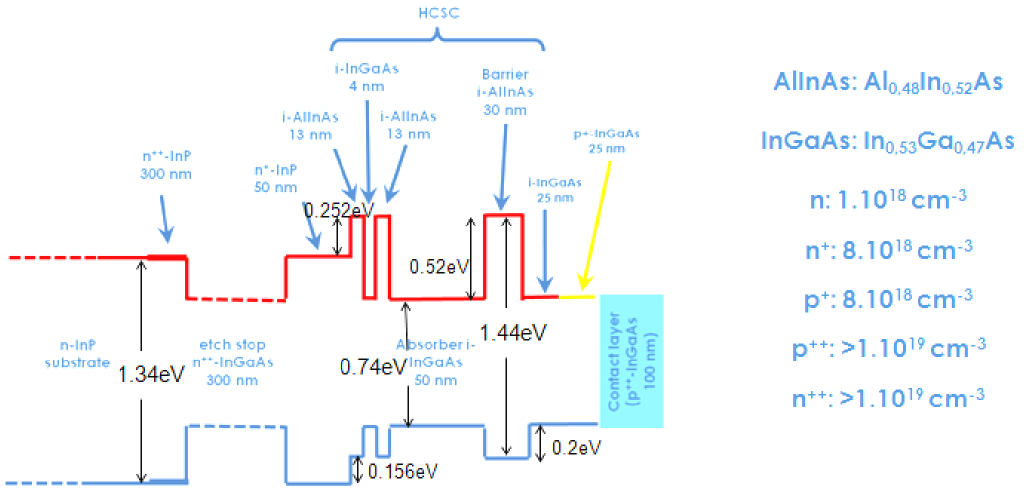

Fig. 2-7: Very simplified structure and energy diagram (at 300K) of HCSC (selective SQW contact). AlInAs: $Al_{0,48}In_{0,52}As$; InGaAs: $In_{0,53}Ga_{0,47}As$; n: 1.10^{18} cm^{-3}; n^{+}: 8.10^{18} cm^{-3}; p^{+}: 8.10^{18} cm^{-3}; p^{++}: $>1.10^{19}$ cm^{-3}; n^{++}: $>1.10^{19}$ cm^{-3}.

Technological processes involved:

i. Lithography
ii. Electron beam evaporation
iii. Reactive ion etching (RIE)
iv. PECVD

These fabrication steps in the clean-room consist of widely used processes in the microelectronic domain. In our case, four masks are used to define the front contact of the cell. And with metallization on the back side of the cell, we define the other back contact.

General process flow:

1. deposition of the negative resist and lithography 1 (mask 1)
2. first metallization with electron beam evaporation (Ti/Au:20nm/300nm)
3. reactive ion etching (RIE) of the p+ heavily doped InGaAs (Ar/H2/CH4, flow: 8.3/50/16.6)
4. deposition of the positive resist and lithography 2 (mask 2)
5. chemical etching ($H_3PO_4/H_2O_2/H_2O$: 25ml/5ml/200ml) of mesa
   As-layer etching;
   Interface etching;
   Deoxidation.

6. dielectric (Si_3N_4) depositon by PECVD;
7. deposition of the positive resist and lithography 3 (mask 3) and RIE in the centre
8. deposition of the negative resist and lithography 4 (mask 4)
9. second metallization with electron beam evaporation (Ti/Au:20nm/300nm)
10. third metallization (on the back side)with electron beam evaporation (Ti/Au:20nm/300nm)

See Fig. 2-8.

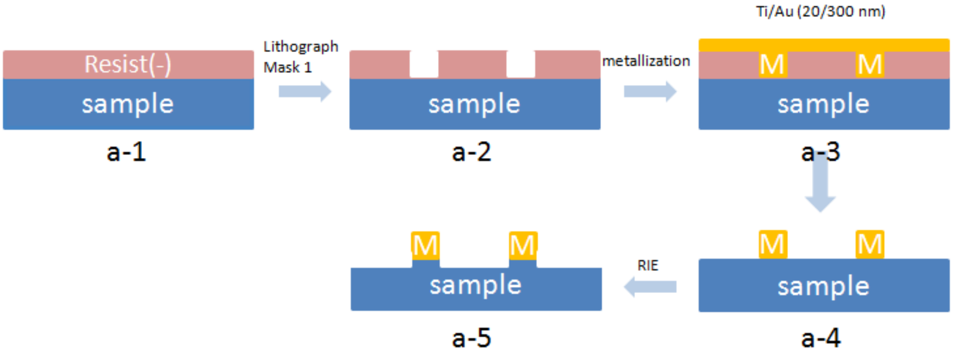

(a). annular metallization, electron beam evaporation, etching InGaAs (p++)

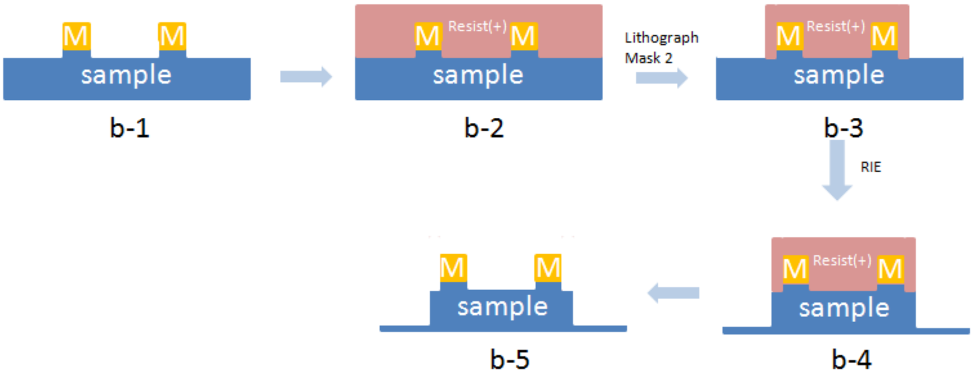

(b). reactive ion etching (RIE) of mesa

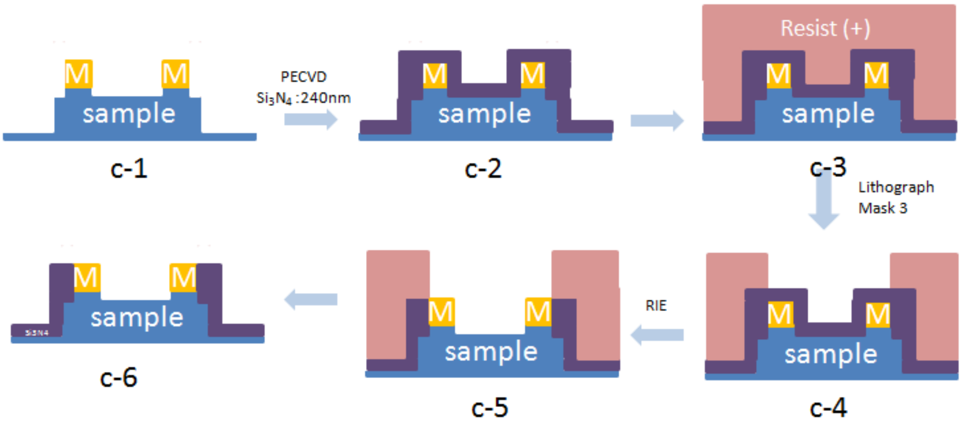

(c). dielectric (Si_3N_4) deposition by PECVD, RIE in the centre

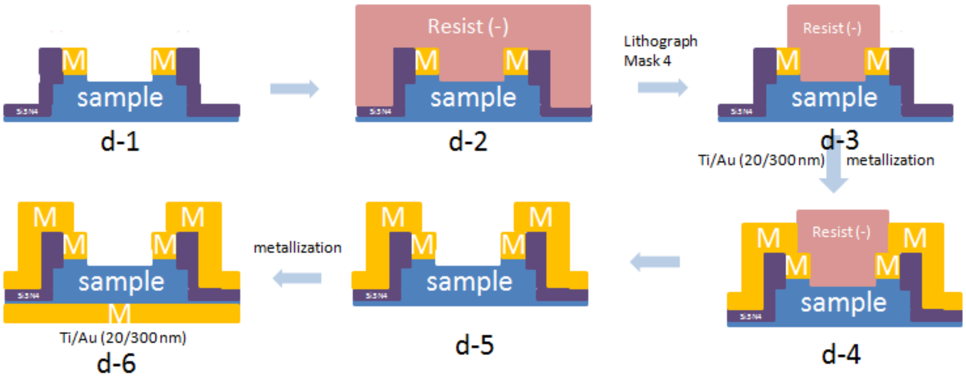

(d) metallization on both sides of the sample: Ti/Au (20/300 nm)

Fig. 2-8: General process flow of HCSC: step (a) – step (d).

2.3. Structural characterizations

2.3.1. X-Ray diffraction

X-ray diffraction (XRD) provides qualitative and quantitative information about the thin layers studied. The positions of the lines on the diffractogram are directly linked to the interatomic distances and correspond to constructive interference between the rays reflected by the reticular planes parallel to each other. These positions are given by Bragg's law:

$$2d \sin \theta = n \lambda \tag{2.1}$$

With:

- d, the distance between the reticular planes
- θ, the angle between the incident beam and the reticular plane
- n, the order of interference, integer, positive
- λ, the wavelength of the incident beam

Bragg’s law is satisfied when the scattering vector Q, which is equal to the difference between the wave vector of the incident beam k_i and that of the reflected beam k_r, is a vector of the reciprocal lattice of the layers studied.

$$Q = k_r - k_i \tag{2.2}$$

$$|Q| = \frac{4\pi \sin \theta}{\lambda} \tag{2.3}$$

It is possible to obtain the information on the stress, the thickness, the relaxation of the layers and the phase separation. The XRD can therefore provide an estimation of the composition of the samples studied through a non-destructive way.

The techniques presented here are those used in this thesis.

2.3.1.1. X-ray diffraction measurement

At FOTON laboratory, XRD is performed using a Philips diffractometer. A general schematic of the system is shown in Fig. 2-9 (top). The X-ray tube uses a copper anode to produce the X-rays. The power supply is set at 35 kV, 40 mA. The asymmetric Ge (002) monochromator with four reflections is used to select the Kα1 line at a wavelength of 1.54056 Å with a low angular divergence of 12 arc seconds from the incident beam. The 4-circle goniometer allows basic translations in direct space (X, Y, Z) and rotations along the four axes ω, 2θ, φ and χ (see Fig. 2-9 (bottom)). ω is the angle of incidence of the beam relative to the sample surface. 2θ is the angle between the direction of the incident beam and the position of the detector. And a 1 mm anti-scattering slit is placed at the entrance of the detector.

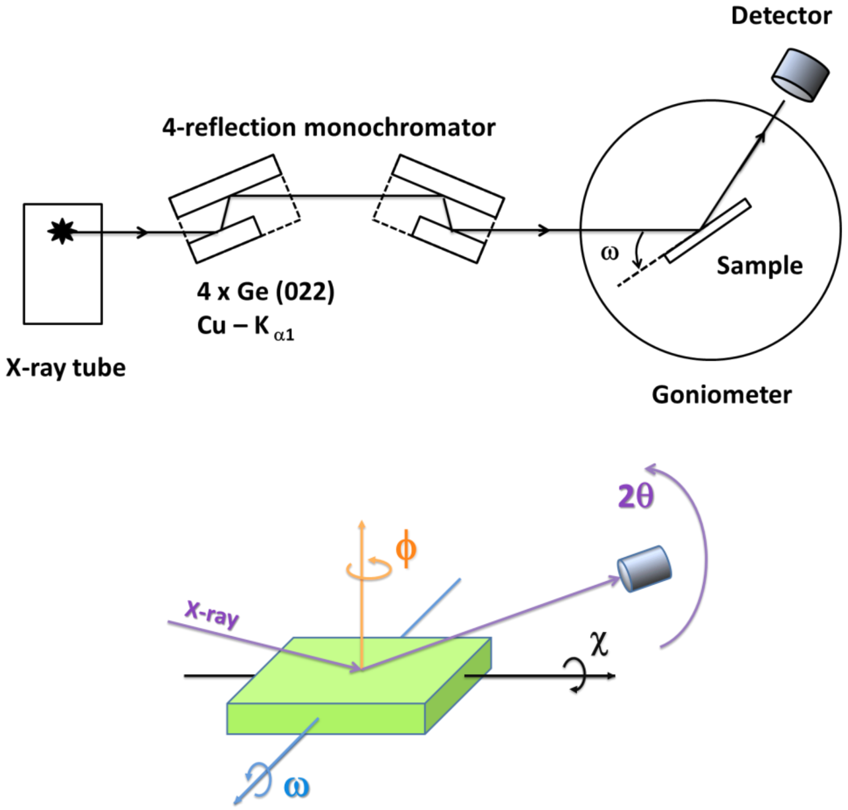

Fig. 2-9: Schematic of the double crystal X-ray diffractometer (top); Diagram of the Philips four-axis goniometer.

Moreover, some XRD measurements were performed at Osirix, the platform of SCANMAT (UAR 2025) dedicated to high-resolution X-ray diffraction and texture measurements at the University of Rennes 1. The Osirix platform is equipped with a Smartlab Rigaku 5-circle diffractometer. We have used the diffractometer, equipped with a HyPix-3000 detector, in a high resolution mode using a front asymmetric Ge (002) monochromator with four reflections.

2.3.1.2. Scan ω/2θ

The scan ω/2θ of the (004) plane is a very common method in XRD to characterize semiconductors grown through epitaxy. During the scan ω/2θ, the sample rotation angle Δω is accompanied by a rotation of the detector Δ2θ=2Δω. This movement keeps the diffusion vector Q always perpendicular to the studied reticular planes. The positions of the peaks according to the diffraction angle follow the Bragg's law, in which one can introduce the expression of the distance d_{hkl} between the planes (hkl) according to the grid parameters. In the case of a cubic crystal with lattice parameter 'a', this distance is :

$$d_{hkl} = \frac{a}{\sqrt{h^2+k^2+l^2}} \tag{2.4}$$

In the case of no stressed nor relaxed layers, the parameter 'a' corresponds to the lattice parameter of the crystal under equilibrium. It is derived directly from the d_{hkl} value given by the position of the peaks on the diffractogram. However, when the epitaxial layer has a lattice parameter larger (or smaller) than the substrate, it undergoes compressive stresses (respectively in tension). The lattice parameter of the unconstrained material a_{FOS} must then be evaluated from the lattice parameter of the stressed layer a_{STR} (determined by Bragg's law), the stiffness constants C_{ij} of the material and the lattice parameter of the substrate a_{SUB}. As for a crystal with cubic symmetry, we have:

$$a_{FOS} = \frac{2\frac{C_{12}}{C_{11}}a_{SUB}+a_{STR}}{1+2\frac{C_{12}}{C_{11}}} \tag{2.5}$$

The determination of the lattice parameter can determine the composition of a layer of ternary material (for example GaP1-xNx) using Vegard's law, in a first approximation:

$$x = \frac{a_{GaP_{1-x}N_x}-a_{GaP}}{a_{GaN}-a_{GaP}} \tag{2.6}$$

However, the percentage of nitrogen determined here may be significantly underestimated. The Vegard's law only takes into account atoms at substitutional sites. In dilute nitrogen, a non-negligible fraction of N atoms can be incorporated into interstitial sites, with negligible effects on stress and therefore on the position of the XRD peak [17]. Thus, Vegard's law constitutes an estimate of the composition. Rutherford backscattering spectrometry (RBS) and secondary-ion mass spectrometry

(SIMS) experiments are required to determine the exact composition.

In the case of compounds with four or more elements, such as InGaAsP absorbers, it is impossible to know exactly the contribution to the constraint of each element. It is then necessary to take into account the information drawn from the XRD with other material characterization methods. One method involved, for example, estimating the band gap energy from the photoluminescence (PL) spectrum of the material, or even the external quantum efficiency (EQE) of a cell produced with it, and crossing this value with the lattice parameter determined from the XRD peak. The concentrations can then be estimated thanks to the values obtained within the framework of the tight-binding theory.

The thickness of a layer can also be measured from the position and integrated width of the corresponding diffraction peak. The thickness is then given by Scherrer equation:

$$t = \frac{\lambda}{\Delta(2\theta)\ \cos(\theta_B)} \tag{2.7}$$

With:

- λ, the wavelength of the incident beam
- θ_B, the Bragg angle of the peak
- $\Delta 2\theta$, the integrated width of the peak

Another technique which is more precise consists in using the thickness fringes (or Pendellösung fringes) which appear in XRD when the correlation lengths are uniform throughout the layer. The slope of fringe order m as a function of the fringe position expressed into scale of the diffraction vector modulus $S = (2 \sin \theta) / \lambda$ yields the corresponding thickness[21].

2.3.2. Optical characterization: Photoluminescence

Photoluminescence (PL) is an effective non-destructive technique to assess the quality of a material through its optical properties. It is one of the most useful techniques for the development of new optically active materials. It consists of the analysis of the photons emitted during the excitation by a beam of light with energy greater than the forbidden band energy of the studied material. The electron-hole pairs generated during these transitions have high kinetic energy and will de-excite by thermalization to reach the extremum of the conduction and valence bands. They will then recombine via various mechanisms (band-to-band transition, transition via intermediate levels) depending on the positions of the bands and the levels of the donors, acceptors and deep centers of the material. By varying different parameters (such as temperature or excitation power), it is also possible to obtain band offsets, identify transitions, and even the structural quality of materials [22], [23]. The evolution of the PL signal over time can also be used to precisely determine the lifetime of charge carriers [24], [25]. In fact, in order to optimize the GaInAsN(Sb) alloy for photovoltaics, PL has been widely used as the incorporation of nitrogen has a strong influence on the optical properties of GaInAs and there is a strong link between the optical and electrical properties of this family of dilute-nitride material [20].

The room temperature PL experiment carried out at FOTON laboratory consists of a pump CSW lasers with wavelengths of 407 nm (50mW), 532nm (250mW), 1064nm (200mW) necessary optical elements to focus the beam, collection of the light re-emitted by the material studied, and filters to attenuate the contribution of the pump laser to the negligible signal. The emission spectrum of the sample can be measured using two spectrometers with detector arrays: Si (0.3-0.1 µm, resolution 1.6 nm), and InGaAs (0.9-2.1 µm, resolution 5 nm).

2.4. Characterization of solar cells:

2.4.1. Quantum efficiency IQE/EQE

The Quantum Efficiency (QE) measurement is a measure of the conversion of the solar light spectrum into electricity as a function of the Energy, therefore the wavelength, of incident light. It is commonly used to understand the opto-electrical properties of solar cells, including current generation, recombination and charge carrier diffusion mechanisms.

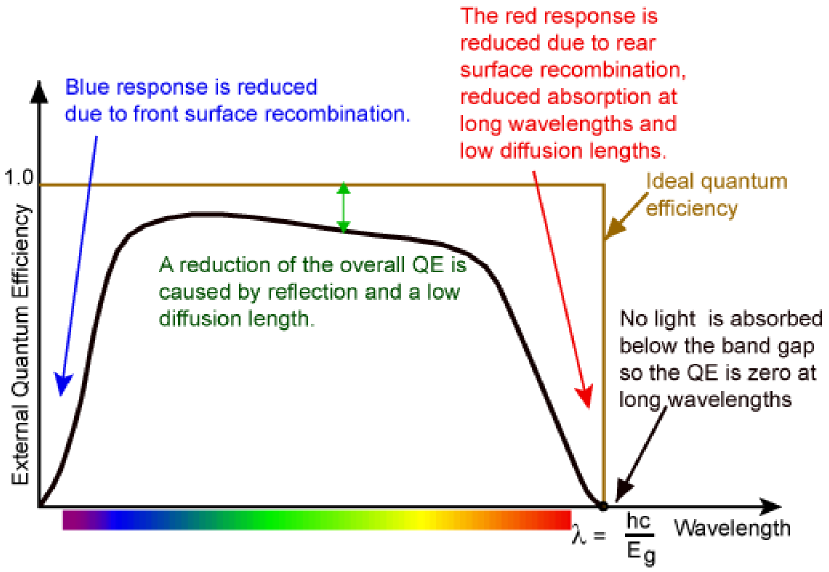

Fig. 2-10: EQE curves from an ideal solar cell and an actual one (from pveducation website)

If all the photons are absorbed and all the photo-generated charge carriers are collected, then the QE should be equal to 100%. Also the photons with an energy below the bandgap are not absorbed, so that the corresponding QE is equal to zero. Therefore, the ideal QE curve of a solar cell would be square shaped as shown in the figure 2-10. However, the QE curves for most solar cells are not ideal. Indeed, this shape is modified by all the optical and electrical losses occurring in the solar cell, such as shading losses, parasitic absorption of incident light, recombination losses, transmission losses etc. Thus, the final QE of the cell depends on three major phenomena: the absorption of light creating the photo-generated charge carriers (electron-hole pairs), the loss of some of the photo-generated carriers due to recombination and the electrical transport of these carriers that contribute to the electrical current from the cell.

Quantum efficiency measurement can be done in two ways. The external quantum efficiency (EQE), more representative of the performance of a cell, takes into account the wavelengths lost by transparency and reflection. We can correct the EQE by the absorption rate and calculate the internal quantum efficiency (IQE) to take into account only the number of photons.

The EQE measurements were carried out at FOTON through the Bentham PVE 300 device (see Fig. 2-11). Typically, the device uses lamps connected to a solar spectrum simulator and a monochromator to allow the passage of each wavelength with the appropriate intensity. The current generated is measured using a synchronous detection amplifier for each wavelength by the intervention of a chopper. A silicon solar cell is included as a reference for calibrating the device before each measurement. The schematic diagram of the PVE 300 is shown as Fig. 2-12.

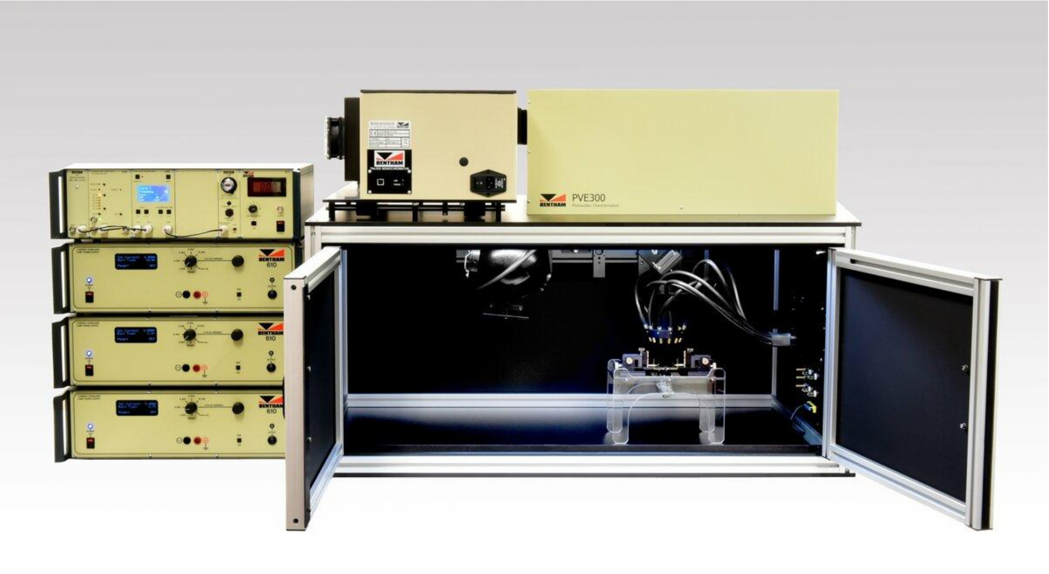

Fig. 2-11: Bentham PVE 300 at FOTON for EQE measurement.

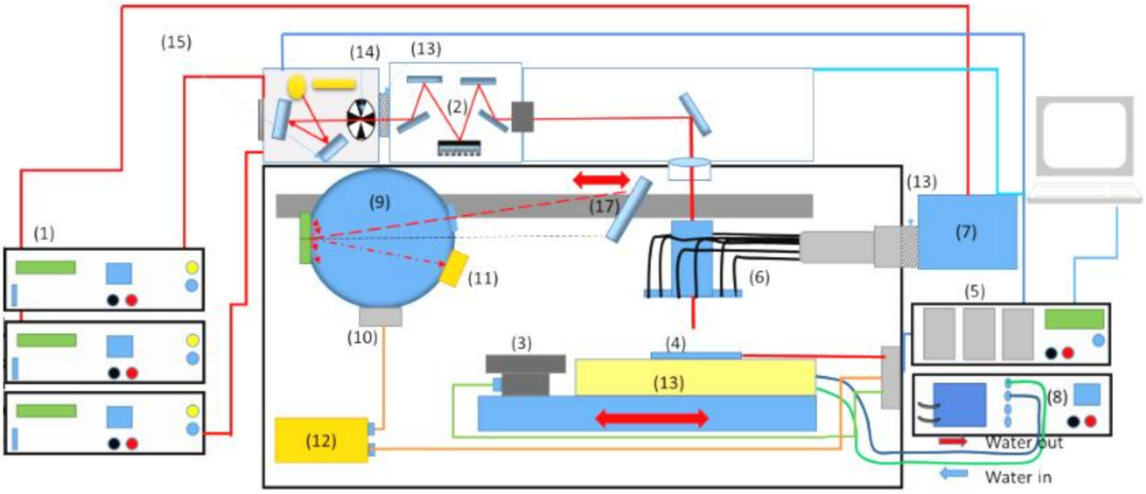

Fig. 2-12: Spectral quantum efficiency system for solar cell characterization. (1) Three constant current lamp power supplies, (2) Monochromator, (3) Reference Detector, (4)Device under test, (5)477 Current preamplifier/485 Lock-in amplifier /Chopper controller, (6) Solar simulator with six-fiber bundle, (7) Xenon Lamp, (8) TemperatureControl, (9) Integrating Sphere, (10) Detector Port, (11)Diffuse SPIN/SPEX Port, (12) Transformer, (13) Shutter, (14) Optical chopper, (15) Swing-away mirror (SAM), (16) Xenon and Halogen lamps, (17) Relay mirror out of beam[26]

2.4.2. Dark I-V

Current-voltage characteristic measurement I(V) is one of the common means of characterization for PV. The measurement presented in this manuscript is both carried out in collaboration with the Rennes 1 University and at FOTON.

A solar cell in non-illumination condition is identical to a PN diode and therefore applicable to the diode equation:

$$I = I_0\left(e^{\frac{qV}{nkT}} - 1\right) \qquad (2.8)$$

With:

- I, diode current
- I_0, saturation current
- q, charge of electron (1.6×10^{-19} coulombs)

- V, voltage applied across diode
- n, the ideality factor of the diode, typically between 1 and 2
- k, the Boltzmann constant
- T, the temperature in Kelvin

Here, the only parameter accounting for the non-ideality of the diodes is the factor n, which equals to 1 for an ideal cell (without recombination in SCR) and equals to 2 when the recombination in the SCR dominates (even if a value higher than 2 may be found in some cases). A more complete modeling of a solar cell must include the resistive effects. A series resistance R_s is often added to include the resistivity of the path taken by carriers throughout the cell (resistance of materials, contact resistance between metal and semiconductor, and resistance of the contacts themselves). The parallel resistance R_{sh} which represents the presence of the alternative paths for the carries (generally due to manufacturing defects) can also be added. These two resistances are the cause of a dissipation of electrical power in the cell which is minimal when R_s tends towards 0 and R_{sh} tends towards infinity. With these two new parameters, the diode equation then becomes:

$$I = I_0\left(e^{\frac{q(V-R_S I)}{nkT}} - 1\right) + \frac{V-R_S I}{R_{sh}} \tag{2.9}$$

It is interesting to numerically determine the parameters I_0, n, R_s and R_{sh} from the I(V) characteristic in the dark in order to obtain information on the quality of the cell.

2.4.3. Light I-V

The current-voltage characteristic of a solar cell under illumination is the characteristic of the PN junction in the dark translated into negative current. Under illumination, equation (2.9) becomes equation (2.10). This translation is due to the photocurrent I_{ph} which is the reverse current of the minority carriers generated during the absorption of the incident photons on the cell (see chapter 1).

$$I = I_0\left(e^{\frac{q(V-R_S I)}{nkT}} - 1\right) + \frac{V-R_S I}{R_{sh}} - I_{ph} \tag{2.10}$$

This I(V) curve makes it possible to obtain the efficiency η of a solar cell by determining the open-circuit voltage V_{OC} and the short-circuit current I_{SC} and the fill factor FF. Then we have:

$$\eta = \frac{P_{max}}{P_{lum}} = \frac{FF \cdot V_{OC} \cdot I_{SC}}{P_{lum}} \tag{2.11}$$

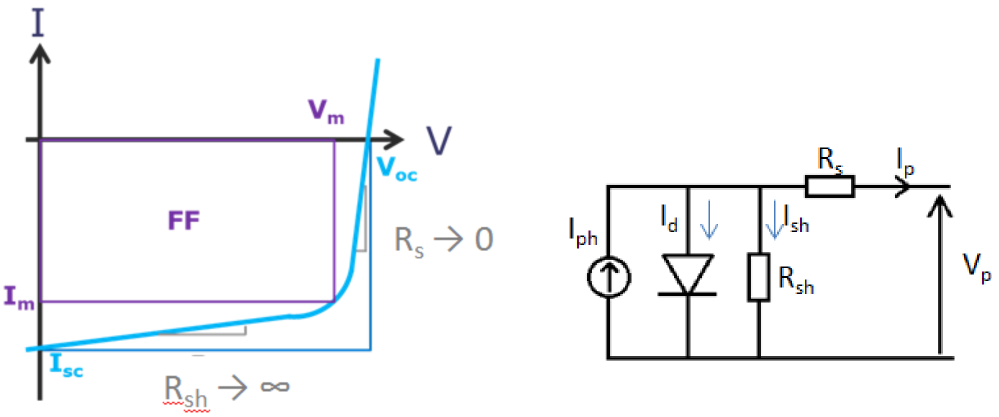

Fig.2-13: Current-voltage characteristics of solar cells under illumination which generates a photo-current I_{ph}; I_d is the current of the diode, I_p is the current produced by the cell.

It is obvious that the efficiency η is the maximum when FF, V_{OC} and I_{SC} are the maximum.

We know that V_{OC} and I_{SC} are very dependent on the bandgap of the absorber, in the mean time they are also strongly influenced by the quality of the material and the architecture of the cell.

I_{SC} is optimal when the photo-generated carriers are numerous and effectively collected by the cell (high collection probability). This requires the use of a material that minimizes the optical losses and recombination. Consequently, the generation rate of the carriers, the diffusion length of the minority carriers and their lifetimes at the interface must be maximized.

Recombination is also detrimental to V_{OC}. In fact, the recombination current participate in the direct current which is exactly opposite to the photo-current when the point V= V_{OC} is reached. Logically, the higher the recombination current, the greater the forward current and the lower the V_{OC}. The saturation current I_0 increases with the recombination current and is therefore a good way to evaluate this phenomenon.

The fill factor FF decreases when R_s is too high or R_{sh} is too low, because these resistances affect the slope of the I(V) curve at points (V_{OC}, 0) and (0, I_{SC}).

2.5. Modeling of hot carrier solar cells with SimWindows

SimWindows is a 1D semiconductor device simulator based on rate equations for various physical processes and the detailed balance principle. The propagation and reflection of light in the structure are treated as well, so that optoelectronic devices can be simulated.

It is the first simulator to combine the major physical models necessary for simulating optoelectronic devices such as surface emitting lasers and quantum well solar cells. The software extends many of the traditional electrical models by adding effects such as quantum confinement, tunneling current, and complete Fermi-Dirac statistics. The optical model includes computing electromagnetic field reflections at interfaces and determining the resonant frequency of laser cavities.

Any semiconductor device simulator must solve the equations describing the statistics and transport of charge through the device under equilibrium and non-equilibrium conditions. Three fundamental variables are necessary to describe uniquely the charge in a semiconductor device. In theory, the choice of variables is arbitrary, but it is easier numerically to solve variables that do not change by orders of magnitude over the length of the device. The variables chosen here are the electrostatic potential, $\phi(x)$, the electron Planck potential, $\eta_c(x)$, and the hole Planck potential, $\eta_\upsilon(x)$. The expressions relating the Plank potentials to the quasi-fermi levels and band edges are:

$$\eta_c(x) = \left(E_{fn}(x) - E_c(x)\right) / \, kT_n(x) \qquad (2.12)$$

$$\eta_\upsilon(x) = \left(E_\upsilon(x) - E_{fp}(x)\right) / \, kT_p(x) \qquad (2.13)$$

E_{FN}, E_{FP} Electron and hole quasi-fermi levels (eV)
E_c, E_v Conduction and valence band edges (eV)
k - Boltzmann Constant (8.62 x 10-5 eV K-1)
T_n (x)Electron Temperature (K)
T_p (x) Hole Temperature (K)

Three equations are necessary to solve the three fundamental variables. These equations vary depending on the simulation type: either equilibrium or non-equilibrium. In addition to equilibrium and non-equilibrium states, a third state, charge-neutral, is also useful to calculate. This is a non-physical state that SimWindows calculates prior to solving the equilibrium and non-equilibrium states.

There are a few equations that are common to each of the three states of a device. These are the effective density of states ($N_{c,v}(x)$), the total carrier concentrations ($n(x)$ and $p(x)$), the ionized doping concentrations ($N_D^+(\eta_c)$ and $N_A^-(\eta_v)$), and the total charge ($\rho(x)$). The bulk versions of these equations are:

$$N_{c,v}(x) = \frac{1}{4\pi^{\frac{3}{2}}}\left(\frac{2m^*_{n,p}(x)kT_{n,p}(x)}{\hbar^2}\right)^{\frac{3}{2}} \tag{2.14}$$

$$n(x) = N_c F_{1/2}(\eta_c) \qquad p(x) = N_v F_{1/2}(\eta_v) \tag{2.15}$$

$$N_D^+(\eta_c) = \frac{N_D}{1+g_D e^{E_D/(kT_n+\eta_c)}} \qquad N_A^-(\eta_v) = \frac{N_A}{1+g_A e^{E_A/(kT_p+\eta_v)}} \tag{2.16}$$

$$\rho(x) = q(p(x) - n(x) + N_D^+(x) - N_A^-(x)) \tag{2.17}$$

$\hbar$, Planck constant (1.0546 x 10^{-34} J s)
g_D, g_A, Donor and acceptor degeneracy factor (unitless)
η_c, the electron Planck potential
η_v, the hole Planck potential
E_D E_A, Donor and acceptor energy level relative to nearest band (eV)
n p, Total electron and hole concentration (cm^{-3})

Where Fj(x) is the Fermi integral of order j.

SimWindows uses q model for the charge in the quantum well that incorporates both the bound charge and the free charge. The density of states diagram in Fig. 2-14 shows the distinction between these two types of charge.

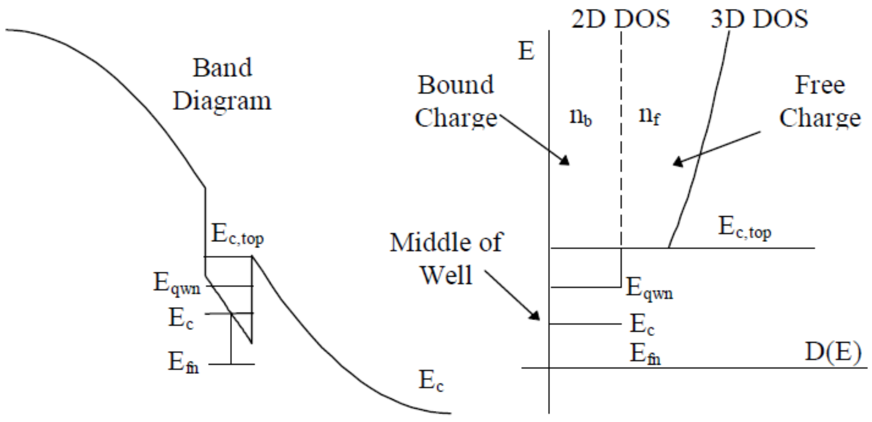

Fig. 2-14: Quantum well and corresponding density of states

The equations for the total charge in a quantum well employ several assumptions.

1) There is only one bound state below $E_{c,top}$, all states above $E_{c,top}$ are free.
2) The quantized energy level, E_{qwn}, is constant relative to the conductionband at the middle of the quantum well.
3) There is an abrupt transition between the two-dimensional and the three-dimensional density of states at an energy of $E_{c,top}$.
4) The quasi-fermi level is constant in the well.
5) Boltzmann statistics can describe the free charge. Using these assumptions, the equations for the bound carrier concentrations are:

Charge neutrality is a non-physical device state in which there is no net charge at all points in the device. SimWindows uses it only as a starting point for more simulations. It can calculates the electrostatic potential and the electron and hole Planck potential under the assumption of no net charge.

We use SimWindows to simulate our HCSC samples, both ternary and quaternary (see more details in Chapter 4).

2.6. Modeling of I-V curves with a two-diode equivalent circuit model

“zweidiodenmodell” (by Sephan Suckow[27], [28]) allows to simulate or fit current-voltage (I-V) measurement data of solar cells (or more generally p-n junctions) using different 2- or 3-diode models. Different file formats and batch processing are supported as well as different modes: dark or illuminated I-V curve fitting, variable fixed ideality factors, Suns- V_{OC} and an extended 2-diode model taking into account the distributed nature of a part of the series resistance according to a model developed by Breitenstein and Rißland[29].

The physical model used here is the regular 2-diode model.

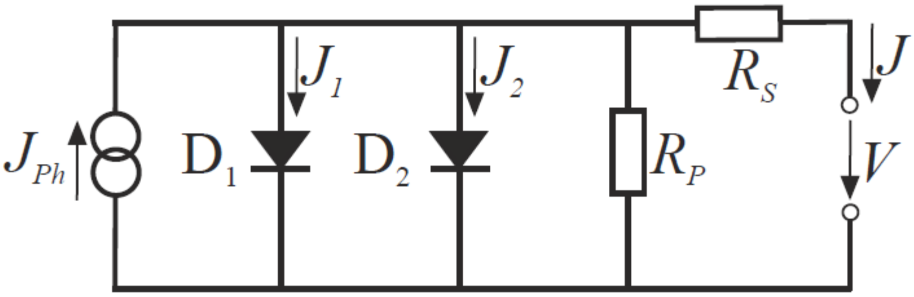

Fig. 2-15: Equivalent circuit of a solar cell according to the 2-diode model[27].

J and V are the current and voltage at the contacts, R_S is the lumped series resistance of the entire device, R_P a parallel resistance (shunt), D_1 is the diode to describe the diffusion current J_1, D_2 is the diode representing the recombination current J_2 and J_{Ph} is the photo current.

The 2-diode model has been pioneered by Wolf and Rauschenbach in 1963[30] and since then has become a valuable standard tool for solar cell characterization. Compared to the simpler 1-diode model it provides better accuracy, especially in the vicinity of the maximum power point of conventional Si solar cells[31].

We use “zweidiodenmodell” to simulate I-V curves, both under dark and illumination (see more details in Chapter 3).

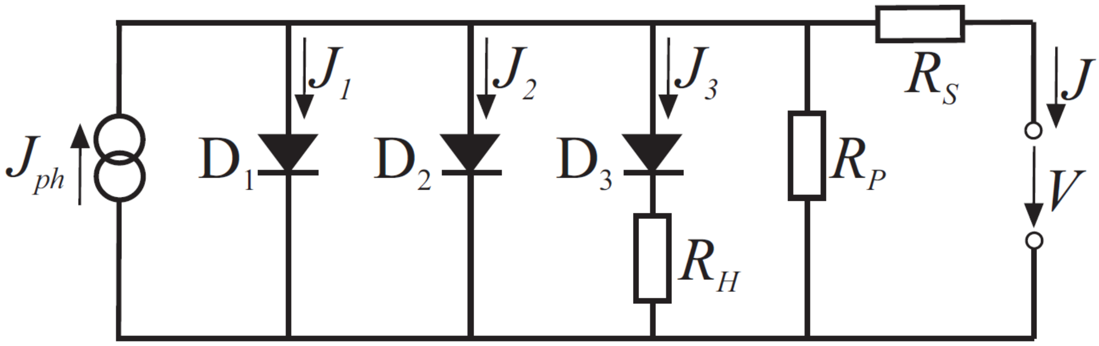

Fig. 2-16: Equivalent circuit of a solar cell according to the 3-diode model with resistance limited recombination[27].

We have also used an extension of the classical 2-diode model proposed in the same software, with adding a 3rd D_3 connected via an additional series resistance R_H. Diode D_3 represents recombination currents owing through regions with increased series resistance. This resistance must be due to local defects, because if it was homogenously distributed it would already be included in RS. This extension of the regular 2-diode model has been popularized by McIntosh[32].

References:

[1] Y. Furukawa, H. Yonezu, A. Wakahara, S. Ishiji, S. Y. Moon, and Y. Morisaki, "Growth of Si/III–V-N/Si structure with two-chamber molecular beam epitaxy system for optoelectronic integrated circuits," *J. Cryst. Growth*, vol. 300, no. 1, pp. 172–176, Mar. 2007, doi: 10.1016/j.jcrysgro.2006.11.021.

[2] J. M. Hartmann, V. Benevent, J. F. Damlencourt, and T. Billon, "A benchmarking of silane, disilane and dichlorosilane for the low temperature growth of group IV layers," *Thin Solid Films*, vol. 520, no. 8, pp. 3185–3189, Feb. 2012, doi: 10.1016/j.tsf.2011.10.164.

[3] K. Volz *et al.*, "GaP-nucleation on exact Si (0 0 1) substrates for III/V device integration," *J. Cryst. Growth*, vol. 315, no. 1, pp. 37–47, 2011, doi: 10.1016/j.jcrysgro.2010.10.036.

[4] O. L. Alerhand, A. N. Berker, J. D. Joannopoulos, D. Vanderbilt, R. J. Hamers, and J. E. Demuth, "Finite-temperature phase diagram of vicinal Si(100) surfaces," *Phys. Rev. Lett.*, vol. 64, no. 20, pp. 2406–2409, May 1990, doi: 10.1103/PhysRevLett.64.2406.

[5] A. J. Hoeven, J. M. Lenssinck, D. Dijkkamp, E. J. van Loenen, and J. Dieleman, "Scanning-tunneling-microscopy study of single-domain Si(001) surfaces grown by molecular-beam epitaxy," *Phys. Rev. Lett.*, vol. 63, no. 17, pp. 1830–1832, Oct. 1989, doi: 10.1103/PhysRevLett.63.1830.

[6] B. S. Swartzentruber, Y.-W. Mo, R. Kariotis, M. G. Lagally, and M. B. Webb, "Direct determination of step and kink energies on vicinal Si(001)," *Phys. Rev. Lett.*, vol. 65, no. 15, pp. 1913–1916, Oct. 1990, doi: 10.1103/PhysRevLett.65.1913.

[7] V. W. L. Chin, B. Zhou, T. L. Tansley, and X. Li, "Alloy-scattering dependence of electron mobility in the ternary gallium, indium, and aluminum nitrides," *J. Appl. Phys.*, vol. 77, no. 11, pp. 6064–6066, Jun. 1995, doi: 10.1063/1.359131.

[8] G. W. Wicks *et al.*, "Use of a valved, solid phosphorus source for the growth of Ga 0.5 In 0.5 P and Al 0.5 In 0.5 P by molecular beam epitaxy," *Appl. Phys. Lett.*, vol. 59, no. 3, pp. 342–344, Jul. 1991, doi: 10.1063/1.105590.

[9] J. S. Harris *et al.*, "Development of GaInNAsSb alloys: Growth, band structure, optical properties and applications," *Phys. status solidi*, vol. 244, no. 8, pp. 2707–2729, Aug. 2007, doi: 10.1002/pssb.200675620.

[10] A. J. Ptak, D. J. Friedman, and S. W. Johnston, "A comparison of MBE- and MOCVD-grown InGaAsN," in *International Conference on Molecular Bean Epitaxy*, 2002, vol. 251, pp. 291–292, doi: 10.1109/MBE.2002.1037874.

[11] H. Carrère, A. Arnoult, A. Ricard, X. Marie, T. Amand, and E. Bedel-Pereira, "Nitrogen-plasma study for plasma-assisted MBE growth of 1.3 μm laser diodes," *Solid. State. Electron.*, vol. 47, no. 3, pp. 419–423, Mar. 2003, doi: 10.1016/S0038-1101(02)00382-9.

[12] K. Klosek, M. Sobanska, G. Tchutchulashvili, Z. R. Zytkiewicz, H. Teisseyre,

and L. Klopotowski, “Optimization of nitrogen plasma source parameters by measurements of emitted light intensity for growth of GaN by molecular beam epitaxy,” *Thin Solid Films*, vol. 534, pp. 107–110, May 2013, doi: 10.1016/j.tsf.2013.02.013.

[13] M. M. Oye *et al.*, “Effects of different plasma species (atomic N, metastable N2*, and ions) on the optical properties of dilute nitride materials grown by plasma-assisted molecular-beam epitaxy,” *Appl. Phys. Lett.*, vol. 91, no. 19, p. 191903, Nov. 2007, doi: 10.1063/1.2806226.

[14] M. A. Wistey, S. R. Bank, H. B. Yuen, H. Bae, and J. S. Harris, “Nitrogen plasma optimization for high-quality dilute nitrides,” *J. Cryst. Growth*, vol. 278, no. 1–4, pp. 229–233, May 2005, doi: 10.1016/j.jcrysgro.2004.12.060.

[15] J. Kuyyalil *et al.*, “Nitrogen–phosphorus competition in the molecular beam epitaxy of GaPN,” *J. Cryst. Growth*, vol. 377, pp. 17–21, Aug. 2013, doi: 10.1016/j.jcrysgro.2013.04.052.

[16] A. Aho *et al.*, “Composition dependent growth dynamics in molecular beam epitaxy of GaInNAs solar cells,” *Sol. Energy Mater. Sol. Cells*, vol. 124, pp. 150–158, May 2014, doi: 10.1016/j.solmat.2014.01.044.

[17] H. Jussila *et al.*, “Substitutionality of nitrogen atoms and formation of nitrogen complexes and point defects in GaPN alloys,” *J. Phys. D. Appl. Phys.*, vol. 47, no. 7, p. 075106, Feb. 2014, doi: 10.1088/0022-3727/47/7/075106.

[18] S. R. Kurtz, A. A. Allerman, C. H. Seager, R. M. Sieg, and E. D. Jones, “Minority carrier diffusion, defects, and localization in InGaAsN, with 2% nitrogen,” *Appl. Phys. Lett.*, vol. 77, no. 3, pp. 400–402, 2000, doi: 10.1063/1.126989.

[19] B. Kunert, D. Trusheim, V. Voßebürger, K. Volz, and W. Stolz, “Annealing experiments of the GaP based dilute nitride Ga(NAsP),” *Phys. status solidi*, vol. 205, no. 1, pp. 114–119, Jan. 2008, doi: 10.1002/pssa.200777476.

[20] K. Volz *et al.*, “Optimization of annealing conditions of (GaIn)(NAs) for solar cell applications,” *J. Cryst. Growth*, vol. 310, no. 7–9, pp. 2222–2228, Apr. 2008, doi: 10.1016/j.jcrysgro.2007.11.199.

[21] O. Durand, D. Rogers, F. H. Teherani, M. Andrieux, and M. Modreanu, “Studies of oxide-based thin-layered heterostructures by X-ray scattering methods,” *Thin Solid Films*, vol. 515, no. 16, pp. 6360–6367, Jun. 2007, doi: 10.1016/j.tsf.2006.11.111.

[22] R. Kudrawiec *et al.*, “Photoluminescence from as-grown and annealed GaN0.027As0.863Sb0.11∕GaAs single quantum wells,” *J. Appl. Phys.*, vol. 98, no. 6, p. 063527, Sep. 2005, doi: 10.1063/1.2060940.

[23] J. R. Botha and A. W. R. Leitch, “Photoluminescence in MOVPE-Grown Pseudomorphic InGaAs/GaAs Quantum Wells on Vicinal GaAs Surfaces,” *Mater. Sci. Forum*, vol. 143–147, no. pt 1, pp. 635–640, Oct. 1993, doi: 10.4028/www.scientific.net/MSF.143-147.635.

[24] A. Aho, A. Tukiainen, V. Polojärvi, J. Salmi, and M. Guina, “High current

generation in dilute nitride solar cells grown by molecular beam epitaxy," in *Physics, Simulation, and Photonic Engineering of Photovoltaic Devices II*, Mar. 2013, vol. 8620, p. 86201I, doi: 10.1117/12.2002972.

[25] D. B. Jackrel *et al.*, "Dilute nitride GaInNAs and GaInNAsSb solar cells by molecular beam epitaxy," *J. Appl. Phys.*, vol. 101, no. 11, 2007, doi: 10.1063/1.2744490.

[26] A. M. Karmalawi, D. A. Rayan, and M. M. Rashad, "Establishment and evaluation of photovoltaic quantum efficiency system at central metallurgical research and development institute," *Optik (Stuttg).*, vol. 217, no. March, p. 164931, Sep. 2020, doi: 10.1016/j.ijleo.2020.164931.

[27] S. Suckow, "2/3-Diode Fit (2014)." http://nanohub.org/resources/14300.

[28] S. Suckow, T. M. Pletzer, and H. Kurz, "Fast and reliable calculation of the two-diode model without simplifications," *Prog. Photovoltaics Res. Appl.*, vol. 22, no. 4, pp. 494–501, Apr. 2014, doi: 10.1002/pip.2301.

[29] S. Rißland and O. Breitenstein, "Considering the Distributed Series Resistance in a Two-diode Model," *Energy Procedia*, vol. 38, no. 0, pp. 167–175, 2013, doi: 10.1016/j.egypro.2013.07.264.

[30] M. Wolf and H. Rauschenbach, "Series resistance effects on solar cell measurements," *Adv. Energy Convers.*, vol. 3, no. 2, pp. 455–479, Apr. 1963, doi: 10.1016/0365-1789(63)90063-8.

[31] K. Ishaque, Z. Salam, and H. Taheri, "Simple, fast and accurate two-diode model for photovoltaic modules," *Sol. Energy Mater. Sol. Cells*, vol. 95, no. 2, pp. 586–594, Feb. 2011, doi: 10.1016/j.solmat.2010.09.023.

[32] Keith Reid McIntosh, "Lumps, Humps and Bumps: Three Detrimental Effects in the Current-Voltage Curve of Silicon Solar Cells," University of New South Wales Sydney Australia, 2001.

Chapter 3 Towards the III-V/Si tandem solar cell through a monolithic approach

Nowadays, the best solar conversion efficiencies have been reached thanks to multi-junction solar cells consisting of a stacking of III-V semiconductor single junctions on GaAs or Ge substrates. While displaying high conversion efficiencies, these solar cells suffer from the high cost of such substrates. Therefore, our strategy is to develop a tandem cell on silicon, in order to benefit from both the low cost and technological maturity of silicon cells. Furthermore, this route would surpass the theoretical efficiency limit of the Si single cells. Indeed, theoretical studies have shown that a tandem cell consisting of a 1.7 eV bandgap material on a 1.1 eV Si cell would reach efficiencies as high as 37%[1]. To this aim, we use GaP, grown by MBE, which is quasi lattice-matched with Si. In addition to reaching a perfect lattice matching with Si and improving its optical properties, As and N incorporation in GaP, leading to a GaAsPN absorber, reduces the bandgap from 2.3 eV to the required 1.7 eV pseudo-bandgap. This chapter presents steps towards the development of GaAsPN/Si tandem cells, with a focus on the top junction development on Si substrate, and the GaP/Si interface. In particular, a GaP n-i-p photodiode grown on silicon substrate has been extensively studied, both in a top-top and top-bottom electrical contacts configurations.

3.1. Context of the study

In previous works (PhD works of Samiy Almosni and Mickael Da Silva, and in the framework of the ANR-MENHIRS project), the Institut FOTON lab has studied GaP/GaAsPN/GaP p-i-n junctions MBE-grown on GaP (001) substrates. The bandgap reached was about 1.65 eV (according to the PL peak emission) with a composition of a $As_{0.16}P_{0.80}N_{0.04}$. The quantum efficiency (around 30%) and the I-V curve show that carriers have been extracted from a 1-µm-thick GaAsPN alloy absorber, with a remarkable record open-circuit voltage of 1.18V. However, while 1 µm is required for optimal light absorption, the best cell was obtained using a 300-nm-thick absorber with 2.25% conversion efficiency (and FF of 70%) and EQE (External Quantum Efficiency) around 35%, under AM 1.5G. The general issue in this structure is the still low short-circuit current (3.77 mA/cm^2 in our case)[2]. This was attributed to the low diffusion length of the carriers in the GaAsPN. In addition, a solar cell with short-circuit current density of 4.08 mA/cm^2, and displaying a 1.75% efficiency was also demonstrated. This current density is encouraging considering the low GaAsPN absorber thickness. (300 nm) in this structure[1][3]. Obviously, the GaAsPN structural properties need optimization. A clear pathway to the higher efficiency of the top GaAsPN cell would require a thorough optimization of both the MBE growth and post-growth annealing step, accompanied by a PIN junction architecture improvement. Moreover, we obtained these results despite the lack of any anti-reflective layers and passivation coating. However, these results are promising and validate this approach for the elaboration of a lattice-matched dual-junction solar cell on silicon substrate. In this regard, the Institut FOTON lab has also developed a strategy to grow GaP low-defect layers on silicon, avoiding or reducing most of the local chemistry mismatch at the GaP/Si interface such as anti-phase domains (APDs) and microtwins (MTs) which are typical of epitaxies of polar materials on non-polar ones[4]–[6].

The scope of my PhD work on this topic was to begin to study the solar cells elaboration on silicon substrates.

3.2. Architecture of the targeted tandem cell

The targeted architecture of the final tandem cell is composed of a GaP/GaAsPN/GaP top junction on a silicon bottom junction electrically connected with an all-silicon tunnel junction (maybe by INL-Institue des Nanosciences de Lyon). This targeted structure is given in figure 3-1.

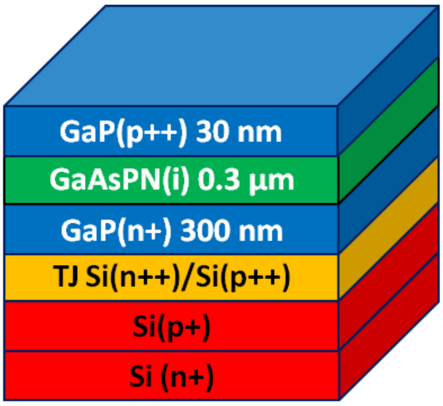

Fig. 3-1: Description of the targeted tandem cell structure (without the electrical contacts).

The thickness of the GaAsPN has been chosen according to the previous studies performed during the thesis of Mickael Da Silva and Samy Almosni, based on a compromise between the solar light absorption and the harvesting of the photogenerated carriers. The top GaP is p-doped with Be and the bottom GaP is n-doped with Si. All the previous studies have been described in previous papers[1], [2][3].

The bottom cell with the Tunnel Junction (TJ) has been performed by INL. Indeed, efficient n++/p++ or p++/n++ TJ on c-Si has been demonstrated, using low-cost techniques combining spin-on dopants and Rapid Thermal Diffusion[7]. It is characterized by sharp high doping profiles (Fig.3-2). Tunnel diodes were fabricated (insert) by INL, exhibiting a peak current density in the 140-270 mA/cm^2 range depending on the structure, much higher than required (20 mA/cm^2). For instance, for a 20 mA/cm^2 current density, voltage losses should be less than 100 μV.

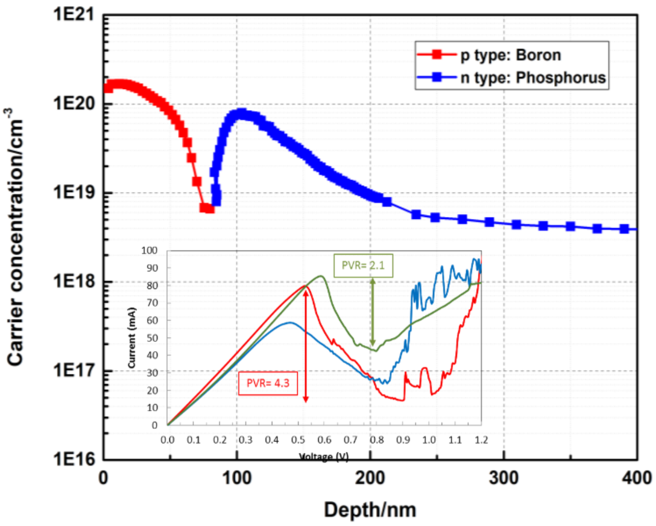

Fig. 3-2: Doping profile corresponding to a p++/n++ tunnel junction. Insert: I(V) profile for a tunnel diode exhibiting high peak density.

3.3. Ohmic contacts on GaP

3.3.1. Physics of contacts on semiconductors

In a photovoltaic component, it is necessary to ensure that charge carriers are collected efficiently, which implies developing ohmic contacts with the lowest possible resistance. The physics of metal/semiconductor (SC) contacts is discussed in this section.

The work function of a material refers to the energy required for an electron to be extracted from the Fermi E_F level of the material to the vacuum level. The behavior of a metal/semiconductor contact depends on the difference between the work functions of both the metal Φ_M and the SC Φ_S. In particular, the difference between these work functions determines the rectifying (Schottky) or ohmic behavior of the electrical contact.

When contact is achieved, the electrons diffuse to the lowest energy level between the Fermi level of the metal or the conduction band of the SC: thermodynamic equilibrium is then reached when the Fermi levels of the metal and the SC are aligned. Fig. 3-3 and Fig. 3-4 show the evolution of the band structure for a metal/SC n-type interface before and after contact. χ is the electronic affinity of the semiconductor.

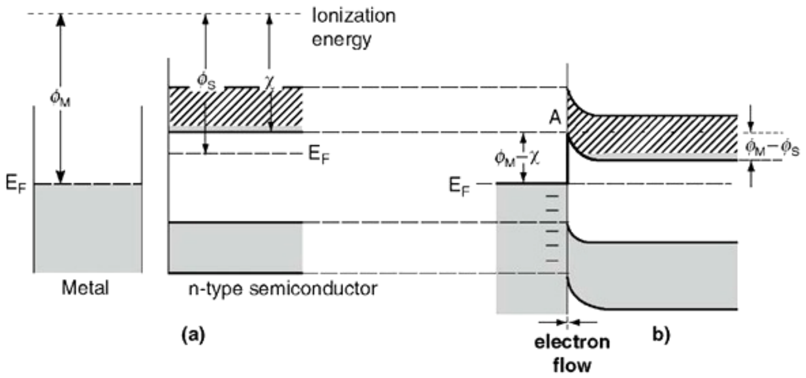

Fig. 3-3: Band diagram of an n-type semiconductor/metal interface before (a) and after (b) contact in the $\Phi_M>\Phi_S$ case. The contact here is rectifier (Schottky).

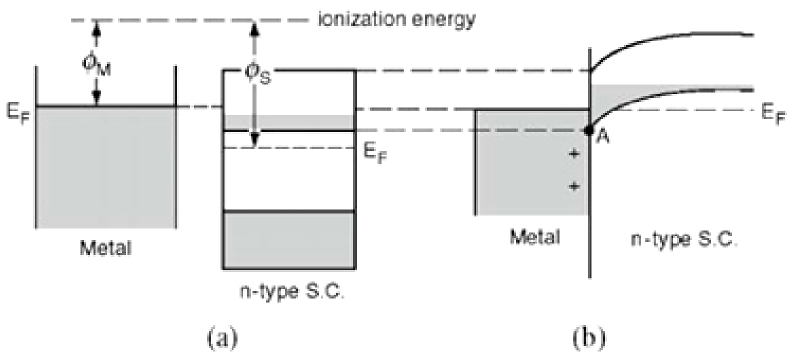

Fig. 3-4: Band diagram of an n-type semiconductor/metal interface before (a) and after (b) contact in the $\Phi_M<\Phi_S$ case. The contact here is ohmic.

Theoretically, in the case where Φ_S is smaller than Φ_M, the deformation of the SC electronic bands generates a potential barrier of energy Φ_M - Φ_S. The interface region where the mobile carriers have been diffused away is called the depletion zone (it remains only uncovered ions). When a reverse external bias is applied, the width of the depletion area is large: the passage of electrons from the SC to the metal is then blocked. On the contrary in forward polarization, its thickness is lower and the passage of current is possible (see Fig. 3-5 (a)). This is the rectifying behavior of a Schottky contact.

On contrary, if Φ_S is greater than Φ_M, the curvature of the SC band theoretically does not generate a barrier. The relationship between the applied bias and the current flowing through the metal/SC junction is then linear: we obtain an ohmic contact (Fig. 3-5 (b)).

In practice, the conditions on the work function must be nuanced. Indeed, the conduction can take place by tunneling effect thanks to the diffusion of doping elements from the metal contact towards the SC which then results in a very high level of doping at the interface. On the other hand, it is possible that the ohmic character of the contact is not verified because of the presence of surface states at the metal/SC interface.

In the case of a p-type SC, a similar behavior is observed for holes. The ohmic or Schottky behavior of a metal/SC contact as a function of doping is summarized in Table 1. It can be seen that the relationships between Φ_S and Φ_M are reversed for the p-type. This is a major problem because, in the case of SCs with large gaps such as GaP (2.26 eV) or GaN (3.4 eV), it is impossible to find a metal with a large enough work function to make an ohmic contact. However, the work function of a material varies with the concentration of dopants. Therefore, one can use thin layers with very high doping at the metal/SC interface. Alternatively, one can reduce the gap with intermediate metamorphic layers (e.g., GaAsP over GaP:p) [8]. The high doping reduces the width of the potential barrier at the interface and allows electrons to tunnel in both directions. In the following, we will discuss the contacts used to study GaP-based top cells at FOTON.

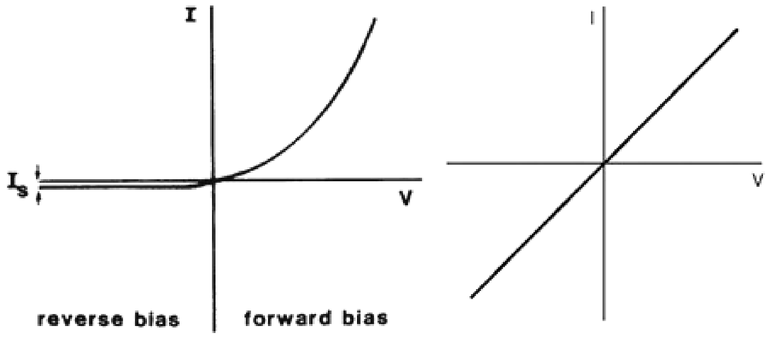

(a) (b)

Fig. 3-5 : Representations of the current-voltage characteristics of a Schottky contact (a) and an ohmic contact (b).

	$\Phi_S < \Phi_M$	$\Phi_S > \Phi_M$
SC type n	**Schottky**	**Ohmic**
SC type p	**Ohmic**	**Schottky**

Table 3.1: Behavior of a metal/semiconductor contact as a function of the type of semiconductor and the difference between the output work of the materials involved.

3.3.2. Contacts on GaP: n+

The n contact on GaP has been studied before the beginning of this thesis by Samy Almosni and Jean-Philippe Gauthier during their PhD. They developed a contact based on a Ni/Au/Ge alloy. The most commonly used alloy for the realization of n-type ohmic contacts on GaAs and InP is the eutectic alloy $Au_{0.88}Ge_{0.12}$ with a nickel diffusion layer [9]. This diffusion layer is essential to realize an alloy with GaP by diffusion of the Ge dopant during the annealing of the contact and to reach doping levels that allow the passage of carriers by tunneling effect. Such Ni/Au/Ge contacts have been studied since the 1970s [10], [11] and have been shown to be suitable for the GaP: n case. Ni/Au/Ge ohmic contacts made at FOTON on GaP substrates doped n at 10^{18} cm^{-3} yield contact resistances of the order of magnitude of 10^{-4}-10^{-5} Ω.cm^2

3.3.3. Contacts on GaP: p+

For a p-type semiconductor, it is common to realize non-annealed metal contacts which need to be deposited on a thin ultra-doped semiconductor layer. This is the case in GaAs devices where thin carbon doped layers allow to expect very high doping levels on which Au/Ti or Au/Pt/Ti alloys are deposited. However, this approach is difficult to employ in the case of p-type GaP. A non-annealed contact on GaP: p has been demonstrated [12] but most studies have focused on annealed contacts. In this case, the high doping of the SC is ensured by diffusion of dopants from the metal contact to the SC during annealing. During the 1970s, in the context of LED development, Au/Be and Au/Zn based contacts were tested and showed modest contact resistances on the order of 10^{-3}-10^{-4} Ω.cm² [11], [13], [14]. In the late 1990s, contacts including a first layer of palladium were explored. With Pd serving as both a wetting layer and a diffusion barrier, ohmic Pd/Zn/Pd contacts with contact resistances of the order of 10^{-5} Ω.cm² after a 3 min anneal at 550 ℃ were demonstrated [15], [16]. Such contacts were first used at FOTON for GaP-based solar cells and showed a contact resistance of $1.8.10^{-5}$ Ω.cm² for a p-doping of 10^{18} cm^{-3} [17]. However, the zinc evaporation was performed in a dedicated Joule evaporator in order to avoid polluting the electron gun frame used for the other metal deposits, which considerably increased the fabrication time of the devices. On the other hand, the very volatile behavior of zinc during its evaporation did not allow to precisely control the homogeneity of the deposited contact.

A new approach involving a thin intermediate layer of GaAsP between the GaP and the contact was then explored by M. Da Silva during his PhD at FOTON lab. The Ti/Pt/Au alloy, common in the GaAs industry, was selected as a candidate for these new p contacts on heavily doped GaAsP. The GaAsP layer was grown by MBE in the sequence $GaAs_{0.2}P_{0.8}$:p+/GaP:p+ (200nm)/GaP:i (100 nm)/GaP:i and the contact resistance ρ_c was evaluated by CTLM (Circular Transmission Line Measurement). The Ti/Pt/Au contact was deposited using an electron gun evaporator. The GaAsP layer was selectively etched in a $H_3PO_4(5)/H_2O_2(1)/H_2O(10)$ solution to ensure the flow of carriers into the GaP. During his PhD work, M. Da Silva showed that the contact deposited directly on GaP without a GaAsP layer did not achieve an ohmic contact, and that it is only possible to realize a Ti/Pt/Au contact on GaP:p if an intermediate GaAsP layer of at least 15 nm thickness is used. Moreover, it appeared that $GaAs_{0.2}P_{0.8}$ doped at 3.10^{19} cm^{-3} was suitable for the realization of ohmic Ti/Pt/Au contacts on GaP:p. The ρ_c values are always of the same order of magnitude (10^{-5}-10^{-6} Ω.cm²) so the good ohmic behavior of these contacts on GaAsP:p+ was confirmed. These values of ρ_c are perfectly suitable for the operation of a PV cell. The contacts were also annealed 30s at 375°C with a slight improvement in ρ_c. Nevertheless, it was considered that the contact was quite efficient and that this step was optional as the difference before and after annealing is low. The CTLM measurements performed on this sample before and after annealing are presented in Fig. 3-6.

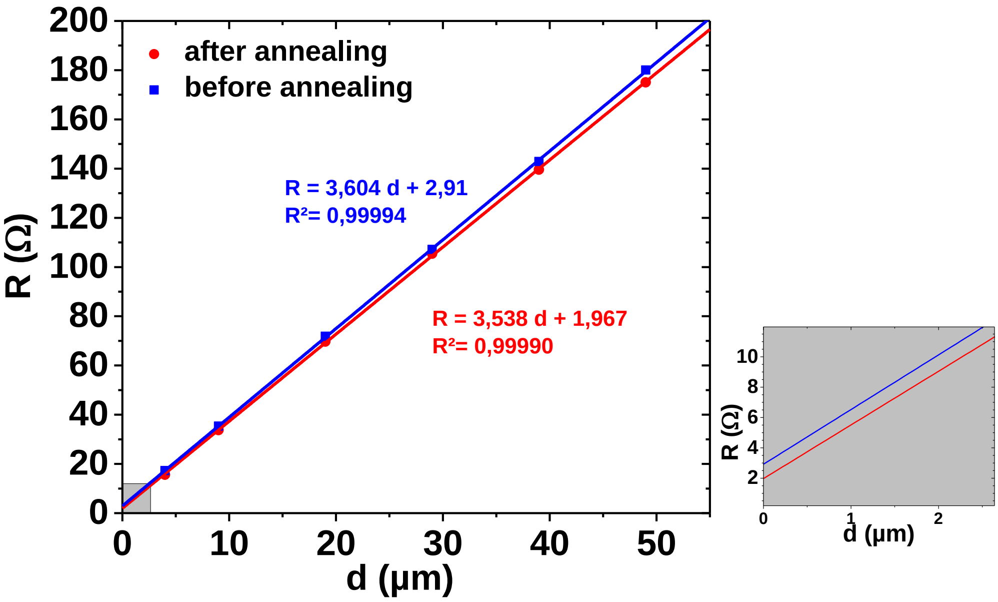

Fig. 3-6: Total resistance measured as a function of the distance d between CTLM patterns for a Ti/Pt/Au contact on GaAsP:p/GaP:p before (blue squares) and after annealing (red disks).

3.3.4. Contact on Si: n+

In the top-bottom configuration, ionic implantation of phosphorus has been performed to n-dope the silicon substrate after the MBE growth, and Al contact (Al with 1% Si) is used. This part has been performed by INL.

3.4. GaP-based absorbers

As an intermediate step towards III-V on silicon tandem cells, the first sample studied is a p-i-n onto Si substrate with an absorber made with a simple GaP binary layer with a thickness of 300 nm, that is the thickness targeted for the future GaAsPN absorber. Figure 3-7 shows the sample structure. A p-i-n junction is grown using solid source molecular beam epitaxy at Institut FOTON. First, a 500 nm-thick i-GaP buffer layer is grown on a n-doped Si substrate. Indeed, in a first step, the study of a doped GaP layer directly on the silicon substrate has not been performed since the first attempts has led to non-single crystalline GaP. Therefore, a first undoped GaP buffer layer has been deposited, leading to a good crystallinity of the GaP Stacking. Then a 300 nm i-GaP absorber sandwiched by a 30 nm p++ GaP (doping rate: 1.10^{19} cm^{-3}) and a 500 nm n-GaP (doping rate: 8.10^{17} cm^{-3}) is grown. Therefore a total thickness of 1 µm thick GaP (500 nm-thick undoped and a 500 nm-thick n-doped) has been grown to ensure a sufficient good crystallinity of the GaP absorber. Finally, a 20 nm p++ GaAsP (doping rate: 3.10^{19} cm^{-3}) is deposited to ensure good electrical injection.

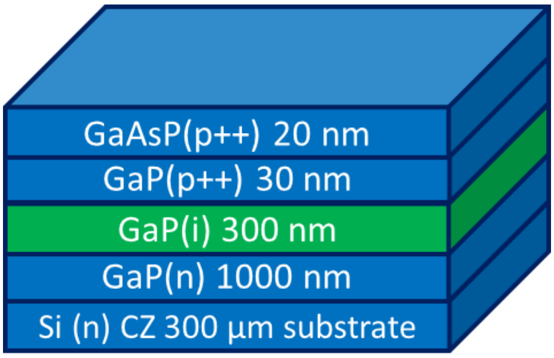

Fig. 3-7: Structure of III-V GaP solar cell on silicon

3.4.1. Structural analysis (XRD)

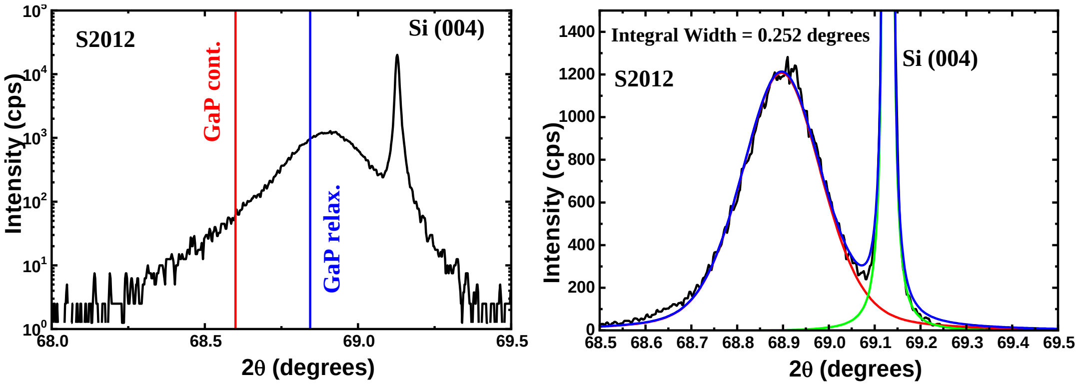

Fig. 3-8: XRD results of the III-V GaP solar cell on Si (presented in section 3.2.1.) around both the Si (004) and GaP (004) diffraction peaks. Left: on a logarithmic scale, and right: on a linear scale and including a modeling of the GaP (004) peak using a pseudo Voigt function.

From the XRD result, we can see clearly that the GaP is fully relaxed. As the critical thickness of GaP/Si is 90nm, and the thickness of our GaP stacking is far more than 90nm, so it is absolutely relaxed[18]. A calculation of the diffraction correlation length along the growth direction, from the integral peak width (Fig. 3-8) and using the Scherrer's law, gives 42.5 nm, much less than the nominal layer thickness. Since this value is inversely proportional to the defects density, which means the layer contains a non-negligible density of crystalline defects, likely due to the relaxation process (a layer grown below the critical thickness usually gives a narrow peak with a width given the thickness, through the Scherrer formula). However, the absence of any other diffraction peaks than the (001) diffraction ones seems to indicate an epitaxy of the GaP on silicon. Moreover, the pole figures performed on the GaP/Si (001) are characteristics of an epitaxy of the GaP onto the Si substrate.

3.4.2. Previous results

Optimization of the GaP growth on silicon substrates and thorough analyses of the GaP epitaxy have been performed during the thesis of Yanping Wang and Ang Zhou. Details of these studies can be found in the following papers[4], [5]. The growth has been performed on (001)-oriented silicon substrates displaying a 6 °-off miscut along the [110] in-plane direction. This allows to eliminate the antiphase domains at the vicinity of the interface between the GaP and the silicon. The optimized GaP layers display a very low density of remaining defects (APDs and MTs), as showed in Fig. 3-9, Fig. 3-10 and Fig. 3-11. Finally, thin GaP display low surface roughness (RMS 0.3 nm), and thick GaP display larger surface roughness (RMS 2 nm).

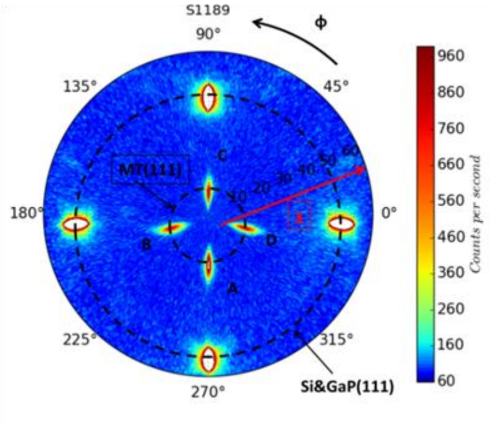

Fig. 3-9: Typical XRD pole figure around the (111) Bragg peak, on a GaP/Si (001) pseudo-substrate, with micro-twins-MTs. The reciprocal lattice streaks around the middle of the pole figure are characteristics of the MTs which are small domains of rotated crystals.

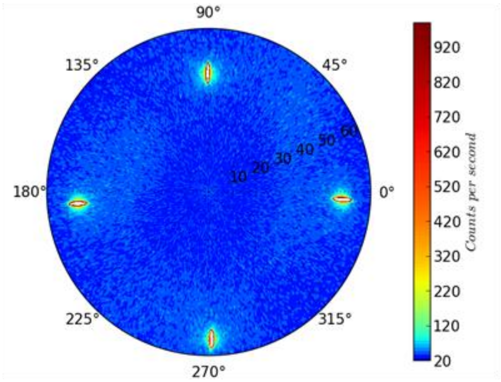

Fig. 3-10: Typical XRD pole figure around the (111) Bragg peak, on a GaP/Si (001) pseudo-substrate without MTs.

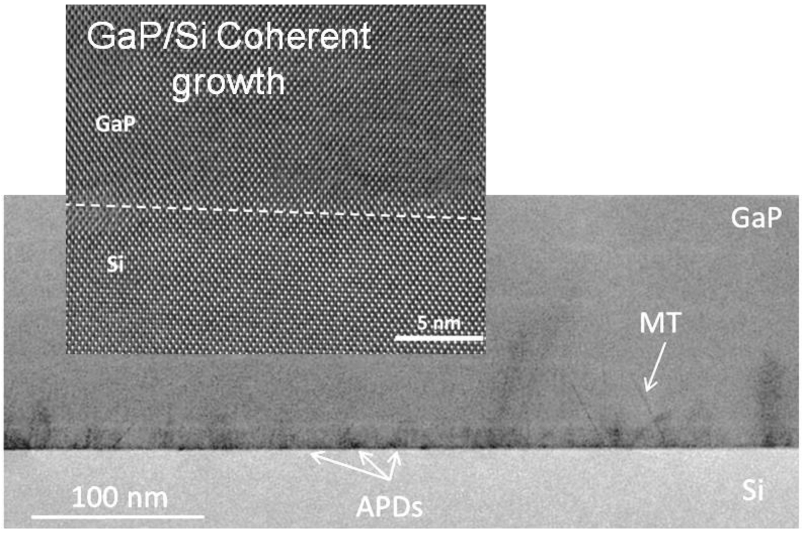

Fig. 3-11: Typical TEM cross-section images displaying nearly inexistent micro-twins and self-annihilating anti-phase domains at the interface between the GaP and the silicon.

3.5. p-i-n cells with top-top electrical contacts

3.5.1. Architecture description

We have first developed some solar cells in a top-top electrical contact configuration in which the electrical current does not see the GaP/Si interface in order to evaluate the influence of this interface, with a comparison between both the top-top and top-bottom configurations. However, we are aware that this comparison is limited due to the difference between the electrical contacts, especially the distances between the front electrical contacts. In this top-top configuration, the contacts are taken on the top GaAsP p++ layer and on the bottom GaP, either n-doped one, or the thick i-GaP (see Fig. 3-7).

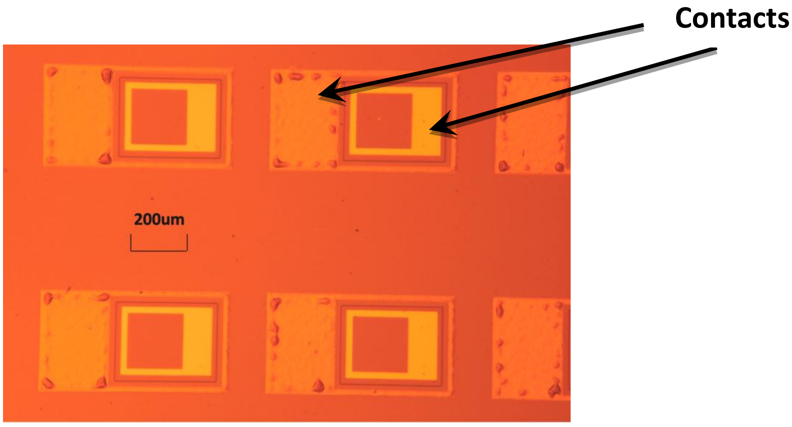

Fig. 3-12: Optical picture of the top electrical contacts in the case of the top-top GaP solar cell.

The inner surface area of the cells was: 200 µm * 195 µm. We have taken this surface into account for the EQE measurements and to calculate the conversion efficiency. However, we have chosen to calculate the electrical current density using the surface between the electrical contacts, that is 365 µm * 290 µm (see Fig. 3-12). The top contact materials used on n-GaP was: Ni-Au-Ge.

3.5.2. Quantum efficiency measurements

The EQE measurements are also performed to study the electro-optical properties of the GaP solar cells with the top-top contacts.

The surface area of the light spot used during the EQE measurement is: 740 µm * 740 µm. The surface area of the top-top sample is: 200 µm * 195 µm which is much smaller than the light spot. In this situation, correction is needed for the EQE result. The Fig. 3-13 are the results corrected according to the surface area of top-top contacts.

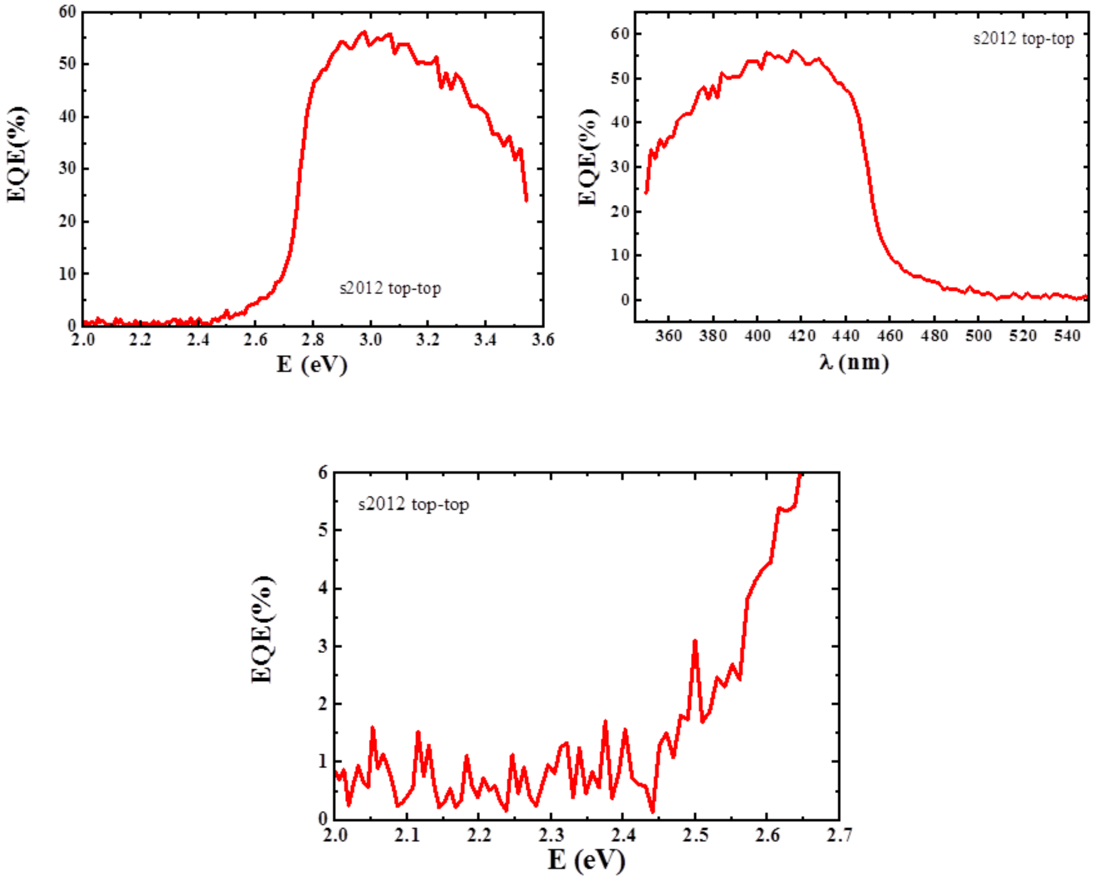

Fig. 3-13: Top: external quantum efficiency (EQE) curves for the p-i-n GaP solar cell in the top-top electrical contacts configuration, versus the Energy, and versus the wavelength. Bottom: zoom in the vicinity of the indirect bandgap.

In this case, only the direct bandgap absorption threshold is seen (Fig. 3-14), which is measured equal to 2.73 eV using a Tauc plot[21], [22], and in agreement with the previous result (top-bottom configuration). The indirect bandgap cannot be measured, because the red response is too low in this case.

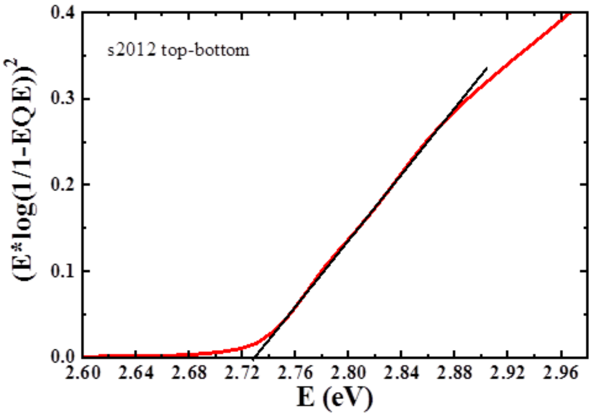

Fig. 3-14: EQE Tauc plot for the direct transition.

Finally, the value of the short-circuit electrical current has been extracted from the EQE, giving 1.82 mA/cm^2 for the top-top contacts sample. The calculated value of J_{SC} from the EQE is on the same order of magnitude with the measured one with the L-I-V measurement (0.84 mA/cm^2 for the top-top, as shown in the following).

3.5.3. L-I-V analysis

The I-V curve under solar light illumination is shown in figure 3-15, which shows also the P-V curve in order to measure the bias at the maximum electrical power. Therefore, the maximum bias and the maximum electrical current are measured equal to 0.811V and 7.101x10^{-4} mA respectively, while the V_{OC} and I_{SC} are measured equal to 0.95V and 8.872x10^{-4} mA. Then the fill factor is equal to:

$$FF = \frac{V_M . I_M}{V_{OC} . I_{SC}} = 68.3\%$$

The top-top solar cell presents a window to harvest the solar light much smaller than the mesa surface. Therefore, we propose a corrected conversion efficiency in this case, taking into account the ratio of the cell window surface of 39.10^{-5}cm^2 and the mesa surface of 106.10^{-5}cm^2. Considering this ratio, the corrected conversion efficiency reaches 1.48%.

$$\eta = \frac{FF . V_{OC} . I_{SC}}{P_{Light}^{STC}} = 1.48\%$$

While, if the efficiency calculated with the same area between the illuminated zone and the extracted electrical current (106.10^{-5}cm^2), we find the efficiency value of 0.54%.

$$\eta = \frac{FF . V_{OC} . I_{SC}}{P_{Light}^{STC}} = 0.54\%$$

Considering the large GaP bandgap, this value is around 18.5% of the theoretical value (8%), calculated from the SQ limit (see Fig. 3-26).

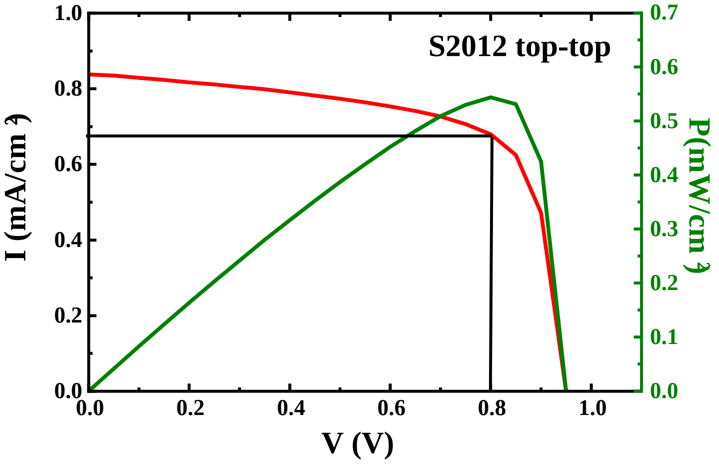

Fig. 3-15: L-I-V curve from a solar simulator, on the "top-top" configuration solar cell. The green curve is the P-V one obtained with the L-I-V.

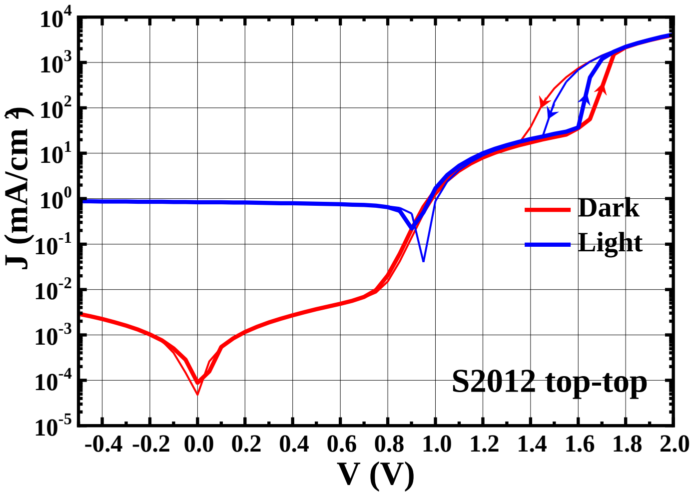

(a)

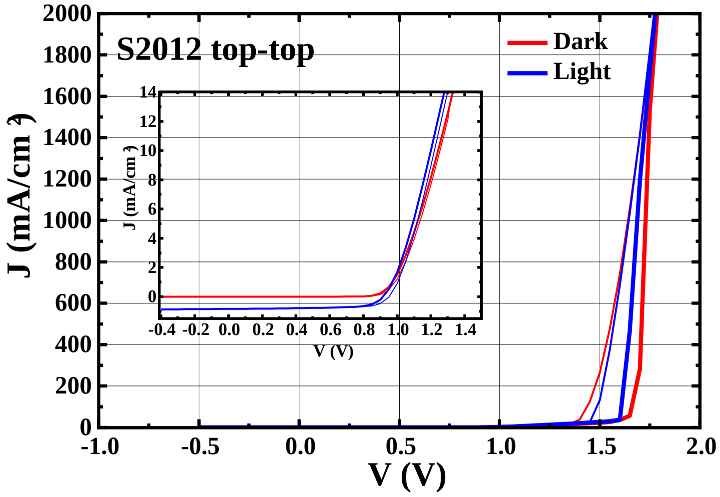

(b)

Fig. 3-16: L-I-V and D-I-V curves: (a) in a logarithmic scale; (b) in a linear scale

Figure 3-16 shows the superimposed I-V curves in the dark and under solar light illumination, in a logarithmic scale. One can remark that both the D-I-V and L-I-V curves show a hysteresis around 1.40 V - 1.75 V. In a first approximation, the R_s and R_{sh} resistances have been determined through the slope of the I-V curve between -0.5V and 0V for R_{sh} and between 1 mA/cm^2 and 1.5 mA/cm^2 for R_s. Considering the Dark I-V curves, R_s has been estimated equal to 53 Ω.cm^2 and R_{sh} equal to $1.8x10^5$ Ω.cm^2; while in the L-I-V case R_s has been estimated equal to 34 Ω.cm^2 (lower than in the D-I-V case) and R_{sh} equal to $1.1\text{x}10^4$ Ω.cm ²(one order of magnitude lower than in the D-I-V case). Let us notice that these values are less accurate than values from a simulation but can be used as factor-of-merit to compare different samples. Therefore, the illumination yields to the increase of shunting paths inside the p-n diode. This can be due to some threading defects inside the stacking (dislocations due to the relaxation of the lattice mismatch?, antiphase domains?, etc..). However, the series resistance seems to be lower in the L-I-V measurement than in the D-I-V one.

I-V curve simulations have been made after to have a better understanding of the physics behind. Fig. 3-17 shows the simulation results that match very well with the experimental results both in the dark and under illuminations. Table 3.2 gives the simulation parameters used to obtain Fig.3-17.

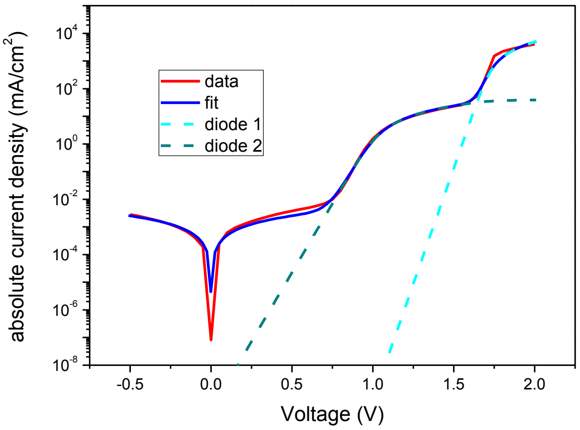

Fig. 3-17: Top-top contacts sample I-V curve simulation using two-diode model in the dark (red dot: original experimental data; blue curve: simulation curve).

J_1 (mA/cm^2)	n1	J_2 (mA/cm^2)	n2	R_{par} (Ω)	R_{ser} (Ω)	R_{rec} (Ω)
$8.6\text{x}10^{-27}$	1	$2.3\text{x}10^{-10}$	1.7	$2\text{x}10^5$	0.05	16.6

Table 3.2: Electrical parameters of top-top contacts sample from I-V curve simulation using two-diode model in the dark.

The simulation model chosen here is a two-diode equivalent circuit with a series resistance added in series to the second diode (in order to obtain a better fit). The description of this model is shown in chapter 2 section 2.6 (see McIntosh dissertation and the "manual for program 2/3-Diode Fit" by Sephan Suckow[19]). The result of the simulation yields a low series resistance of 0.05 Ohm.cm ²and a large shunt resistance of 2.10^5 Ohm.cm ²which is characteristic of a good diode. Moreover, at high injection, that is at large applied bias, the ideality factor of the diode is equal to 1.01, very close to unity (as in an ideal diode characteristic). At lower injection, the second diode displays a larger ideality factor, as expected, around 1.7. Such large ideality factor of the second diode (n2 in the following) seen at lower bias (lower injection regime) could have many origins: Shockley-Read-Hall (SRH) recombination (n2 = 2), Auger recombination (while n2 should be less than unity in this case..), edge shunts (n2 > 2), local Schottky contacts bypassing the pn-junction (n2 = 1.4), etc… All these reported cases have been described in the McIntosh dissertation[20]. However, it is very hard to attribute an effect simply on the value of the n2 ideality factor. Moreover, we can see that, in large injection regime, the I-V curve displays an hysteresis. To enter deeper in the understanding of such effect, let us remark that this behavior is also present in the top-bottom case as shown in the next part (fig 3-24), and at the same voltage (with also an hysteresis phenomenon). Therefore, this effect likely comes from an inner interface inside the GaP stacking or from the GaP/Si interface if the electrical current flows through this interface at such large applied bias. We assume that such effect could arise from an accumulation of charges effect due to a barrier. However, this effect is not completely understood so far.

3.6. p-i-n cells with top-bottom electrical contacts

3.6.1. Architecture description

Using the same stacking than previously, we have developed some solar cells in a top-bottom electrical contact configuration.

Fig. 3-18: Optical picture of the top electrical contacts in the case of the top-bottom GaP solar cell.

The surface area of the cells was: 0.525cm*0.525cm with a finger spacing equal to 200 µm. Therefore, the surface of the cell is equal to 0.276 cm^2. The description of the technological steps is given in details in chapter 2.

3.6.2. Quantum efficiency measurements

We have performed some EQE measurements to study the electro-optical properties of the GaP solar cells. The surface area of the light spot used during the EQE measurement is: 740 µm * 740 µm. The surface area of the top-bottom sample is: 0.525 cm * 0.525 cm which is much larger than the light spot. In this situation, there is no need to correct the EQE result for the top-bottom sample (correction was needed for the top-top sample because the surface area of top-top is smaller than the light spot).

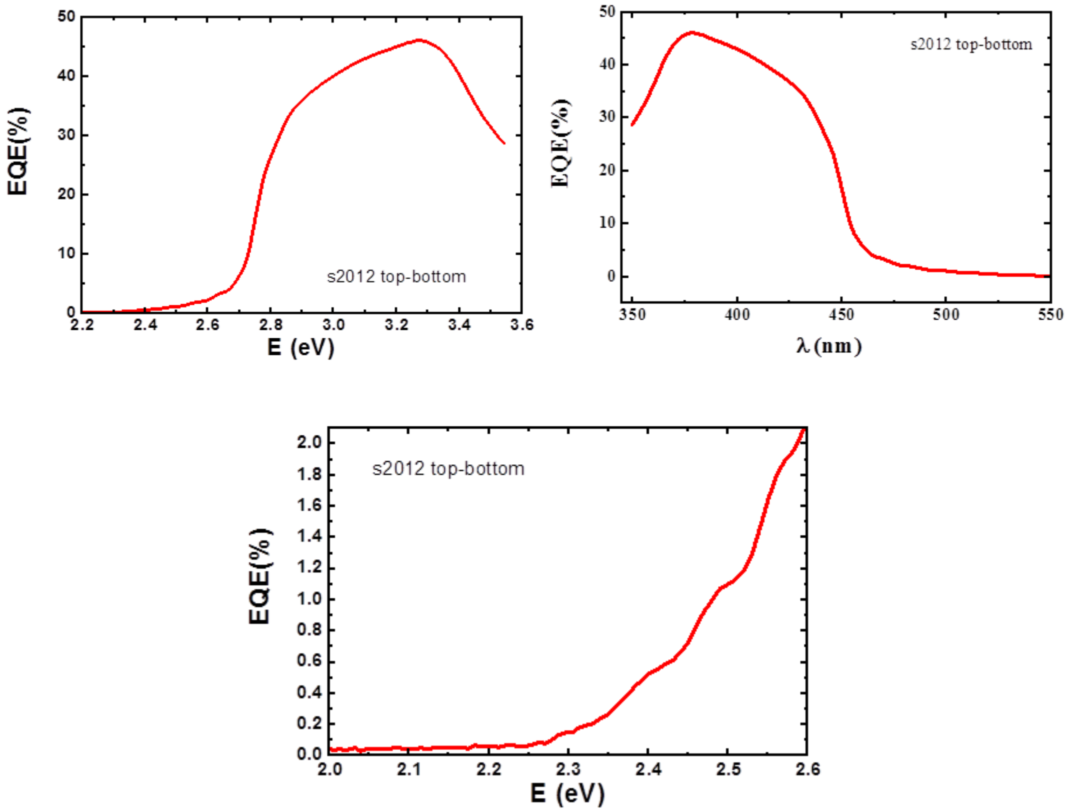

Fig. 3-19: Top: external quantum efficiency (EQE) curves for the p-i-n GaP solar cell in the top-bottom electrical contacts configuration, versus the Energy, and versus the wavelength. Bottom: zoom in the vicinity of the indirect bandgap.

As shown in figure 3-19, there are two absorption thresholds: the first one at around 2.25 eV corresponding to the indirect bandgap of GaP, and at around 2.7 eV, corresponding to the direct bandgap of GaP. I order to clarify the two values of the bandgap, we have performed some Tauc plots from the EQE[21], [22], which gives 2.25 eV for the indirect bandgap and 2.73 eV for the direct one (Fig. 3-20), which is in perfect agreement with the expected values.

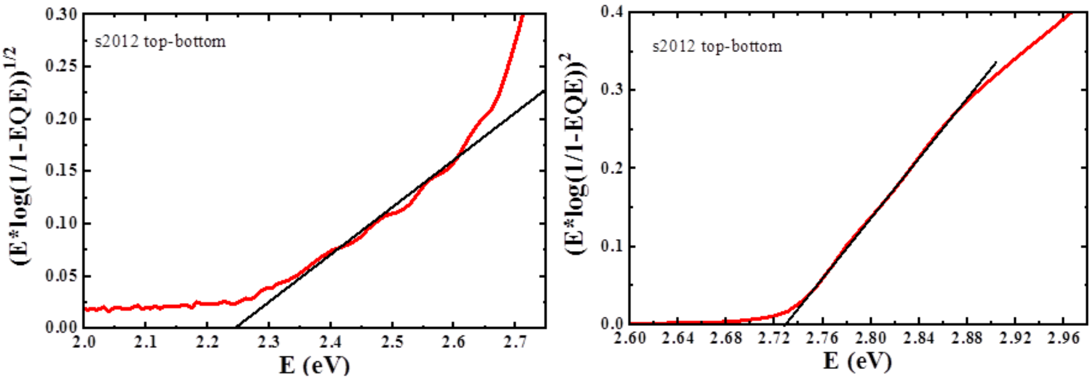

Fig. 3-20: EQE Tauc plots: Left for the indirect transition, and right for the direct

transition.

We can remark that the EQE is 40% at 3 eV and 46% at 3.3 eV. According to reference[23] around 90% of the incoming flux is absorbed in 350 nm of GaP at 3 eV, and 99% at 3.3 eV (and not taking into account the 1 µm-thick n-type and i-type GaP layers below the GaP absorber, in a first approximation). Considering also the transmission coefficient of GaAsP at 3 eV (61.5%) and at 3.3 eV (67%)[23], one can consider, in a rough approximation and according to the fact that our solar cell does not contain any anti-reflection coating (ARC), that the maximum theoretical external quantum efficiency is equal to 55% at 3 eV, and 66% at 3.3 eV. So, we can consider that the differences between these theoretical values and the experimental ones (40% instead of 55% at 3 eV, and 46% instead of 66% at 3.3 eV) mainly come from some issues concerning the extraction of the carriers (limited diffusion lengths in the different materials, losses at the electrical contacts, etc…). Some improvements are possible to overcome the carriers extraction limitation, for instance by decreasing the GaP thickness below the absorber which was fixed at 1 µm in a first step, in order to ensure a sufficient good crystallinity of the GaP absorber. An optimization of the growth of doped GaP directly onto the n-doped silicon substrate would allow to dramatically decrease the buffer thickness, which would allow improving the carriers extraction.

Finally, the value of the short-circuit electrical current has been extracted from the EQE, giving 1.26 mA/cm^2 for the top-bottom contacts sample. The calculated values of J_{SC} are on the same order of magnitude with the measured one (1.49 mA/cm^2 for the top-bottom). It is a common phenomenom in thin film PV devices that the short circuit current calculated from EQE measurement is different to J_{SC} from I-V measurement.

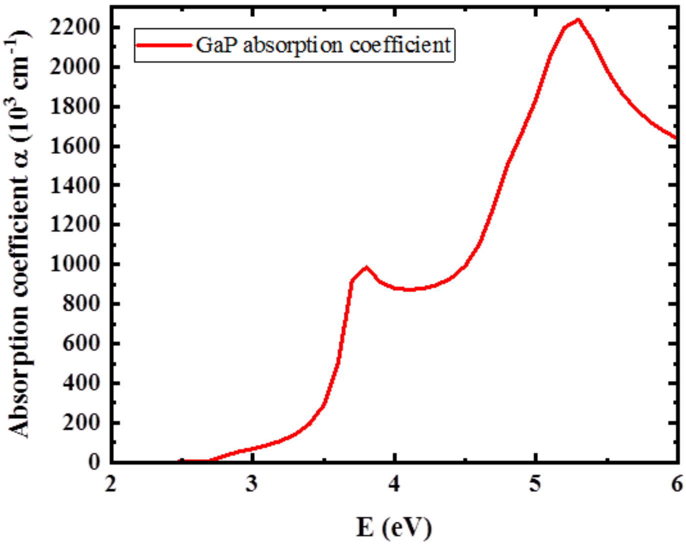

Fig. 3-21: Absorption coefficient of crystalline GaP, from ref.[23]

To compare with the previous study (top-top configuration), we can remark that the

EQE was 55% at 3 eV and 45% at 3.3 eV for the top-bottom. Therefore, the EQE value at 3.3 eV ("blue response") is the same as in the top-top configuration, while the value at 3 eV ("red response") is lower (40% instead of 55%). Since the EQE at lower energy (larger wavelength) is much more sensitive to the absorption at deeper thickness, this could be an indication that the extraction of the carriers is more difficult below the GaP absorber, in the top-bottom configuration, i.e. when the carriers cross the 1 µm thick n- and i-GaP buffer and cross the GaP/Si interface.

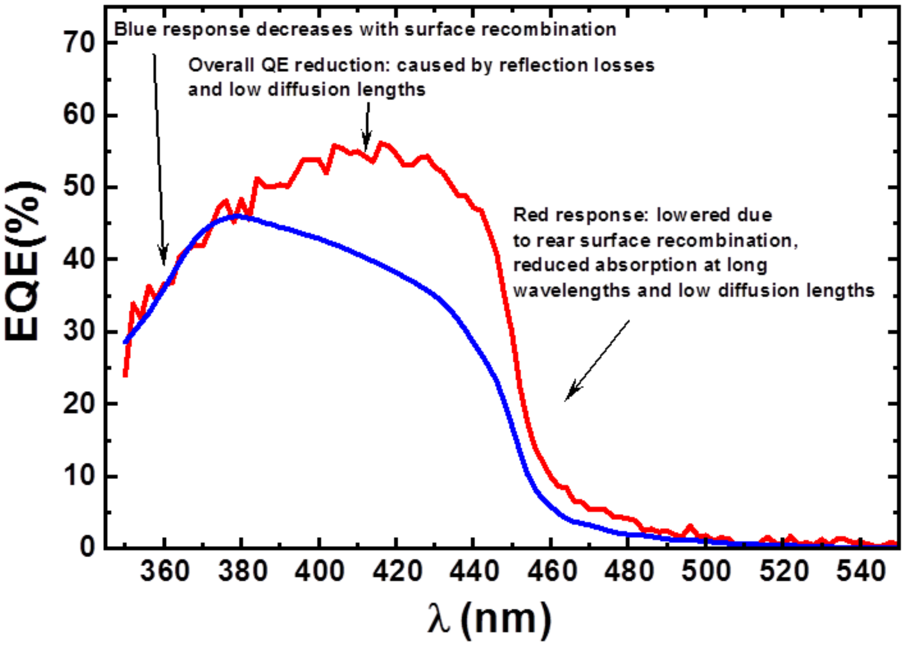

Fig. 3-22: Comparison between the EQE curves of the top-top configuration (red curve) and the top-bottom one (blue curve).

3.6.3. L-I-V analysis

The I-V curve under solar light illumination is shown in figure 3-23, which also shows the P-V curve in order to measure the bias at the maximum electrical power. Therefore, the maximum bias and the maximum electrical current are measured equal to 0.742 V and 0.272 mA respectively, while the V_{OC} and I_{SC} are measured equal to 1.043 V and 0.398 mA. Then the fill factor is equal to:

$$FF = \frac{V_M . I_M}{V_{OC} . I_{SC}} = 48.7\%$$

The electrical current density, taking into account the surface area of the cell is calculated equal to 1.493 mA/cm^2, and the conversion efficiency is therefore:

$$\eta = \frac{FF.V_{OC}.J_{SC}}{P_{Light}^{STC}} = 0.77\%$$

Considering the large GaP bandgap, this value is around 10% of the theoretical value.

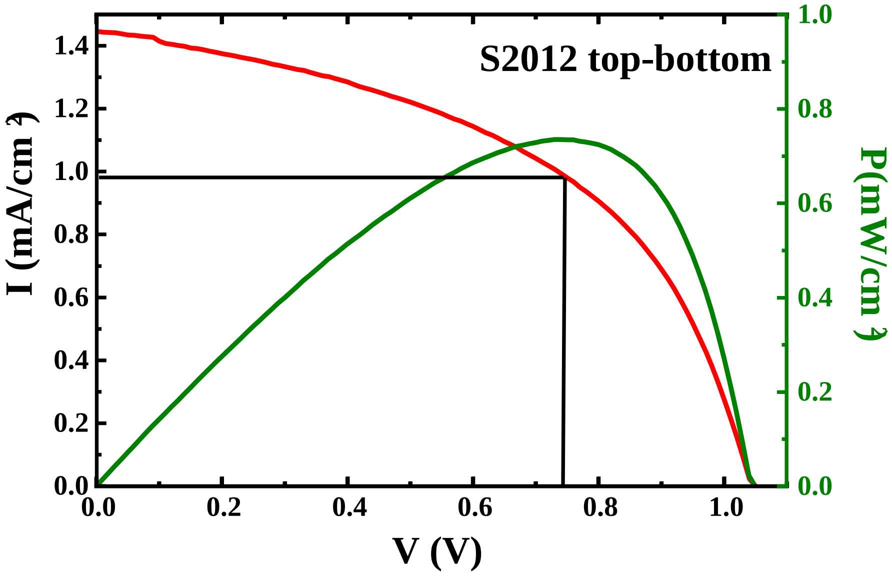

Fig. 3-23: L-I-V curve from a solar simulator, on the “top-bottom” configuration solar cell. The green curve is the P-V one obtained with the L-I-V.

Moreover, the conversion efficiency is reduced by some resistive effects dissipating the electrical power in solar cells. Indeed, series resistance, R_s and shunt resistance, R_{sh} are usually added to the electrical model to describe the L-I-V curves. R_s can be due to parasitic resistances in the metallic contacts, the interconnections, the carrier transport through the different layers, the contact between the metallic contacts and the SC, etc.. R_{sh} can be due to p-n junction non-idealities, impurities near the junction (partial shorting of the junction), shunt near cell edges, any manufacturing defects that provide an alternate current path for the photocurrent.

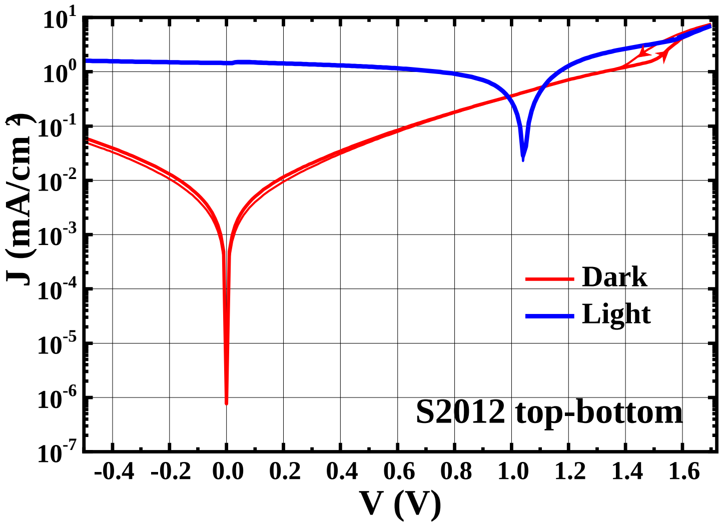

(a)

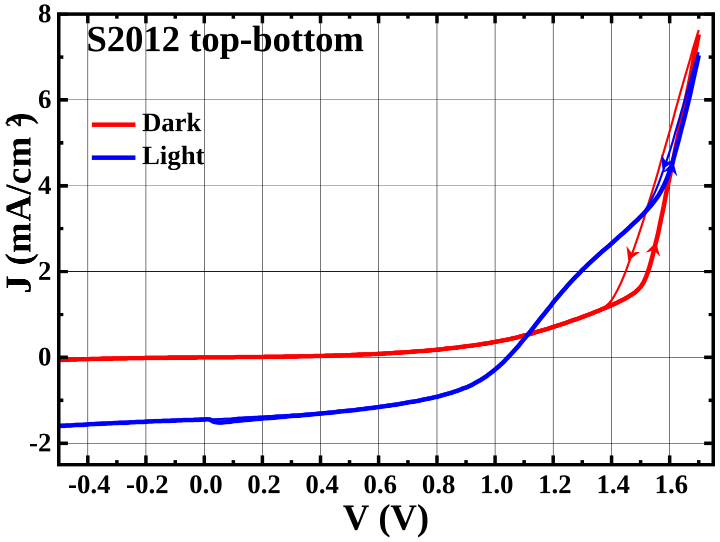

(b)

Fig. 3-24: : L-I-V and D-I-V curves for top-top contacts: (a) in a logarithmic scale; (b) in a linear scale.

Fig. 3-24 shows the superimposed I-V curves in the dark and under solar light illumination, in a logarithmic scale. One can remark that the D-I-V curve shows a hysteresis around 1.4 V – 1.5 V, as in the top-top case, as already reported in the last part (related to the top-top case).

Again, the R_s and R_{sh} resistances have been determined through the slope of the I-V curve between -0.5V and 0V for R_{sh} and between 1 mA/cm ^{2}and 1.5 mA/cm ^{2}for R_s. Considering the Dark I-V curves, R_s has been estimated equal to 302 Ω.cm ^{2}and R_{sh}

equal to $1.0x10^4$ Ω.cm ^{2}; while in the L-I-V case R_s has been estimated equal to 120 Ω.cm ^{2}(almost the same value than in the D-I-V case) and R_{sh} equal to $3.3x10^3$ Ω.cm ^{2} (about one order of magnitude lower than in the D-I-V case). Again, the illumination yields to the increase of shunting paths inside the p-n diode as in the top-top case and the series resistance is lower in the L-I-V measurement than in the D-I-V one All the resistances are around one order of magnitude larger than in the top-top case, which explains the lower FF value and therefore the lower efficiency, despite a larger Jcs in the top-bottom case.

3.7. Comparison between both cells

The Table 3.3 below gives the comparison between the two different types of contacts, top-top contacs and top-bottom contacts.

	V_{OC} (V)	J_{SC} (mA/cm^2)	V_{max} (V)	J_{max} (mA/cm^2)	FF	η	$\eta_{theoretical}$
Top Top	0.95	0.837	0.80	0.680	0.68	0.54%	8%
Top Bottom	1.043	1.493	0.74	1.004	0.48	0.77%	8%

	D-I-V R_s (Ω.cm^2)	L-I-V R_s (Ω.cm^2)	D-I-V R_{sh} (Ω.cm^2)	L-I-V R_{sh} (Ω.cm^2)
Top Top	53	34	1.8×10^5	1.1×10^4
Top Bottom	308	120	1.0×10^4	3.33×10^3

Table 3.3: Electrical results comparison between top-top contacts and top-bottom contacts of the GaP solar cell.

A comparison between the top-top and the top-bottom configurations seems to indicate that the passage through the GaP/Si interface probably degrades a little bit the characteristics of the solar cells in terms of fill factor (due to the degradation of both the series resistance and the shunt resistance). Indeed, top-top contacts sample has a fill factor (FF) of 0.68, which is better than top-bottom contacts sample of 0.48. A reason is because top-top contacts sample has a lower series resistance as revealed by the L-I-V shape. A larger series resistance is probably due to the remaining structural defects at GaP/Si interface, and this can explain the lowering of the EQE shape at the large wavelengths.

However, the results obtained on the top-bottom configuration are sufficiently interesting to develop the III-V/Si tandem cells in the future. In the next section, we will present a first try of a GaAsPN/Si tandem cell, which was not yet optimized. It would be also interesting, in the future, to develop some GaP/Si tandem cells, prior to the optimization of the required GaAsPN/Si tandem solar cells.

The theoretical value for the GaP is extracted from a curve which has been drawn according to the Shockley-Queisser limits (see Fig. 3-25). With a bandgap energy of 2.7 eV (GaP direct bandgap), the theoretical maximum light to electric power conversion efficiency (detailed balance limit) for a solar cell operated at 298.15 K and illuminated with the AM 1.5G is around 8%[24], [25]. Our result for the top-top contacts reaches 18.5% of this maximum theoretical value, which is encouraging for our work.

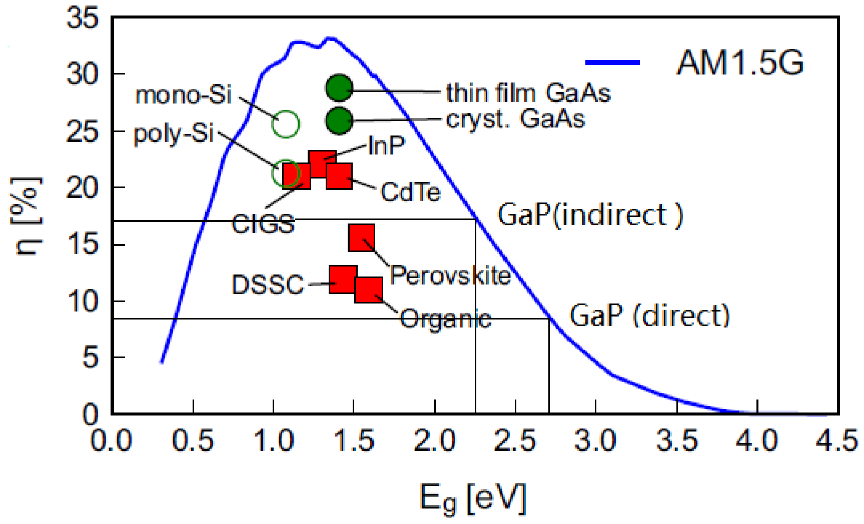

Fig. 3-25: The maximum light to electric power conversion efficiency (detailed balance limit) for a solar cell operated at 298.15 K and illuminated with the AM 1.5G spectral irradiance in accordance with standard solar test conditions as a function of the bandgap energy[25].

3.8. First attempt to develop a tandem cell

In this part, we investigate the targeted sample of the GaAsPN/Si tandem solar cell on silicon grown by MBE. This sample has been performed during a previous thesis work (Mickael Da Silva) and was not fully studied. The bottom structure has been provided by Mustapha Lemiti and Alain Fave from the Institut des Nanosciences de Lyon, in the framework of the MENHIRS project[7], [26]–[28]. The structure of this sample has already been presented in the beginning of this chapter as Fig. 3-1. “p” and “n” doping have been realized using Be and Si respectively. This sample is grown at 480℃ using a Riber Compact 21 Solide Source MBE system. The growth rate has been fixed at 0.5 ML/s. The V/III beam equivalent pressure (BEP) ratio has been set at 10. In order to obtain a GaAsPN compound lattice-matched to the GaP, the As flux has been set at 0.2 µTorr for the sample. Then the sample has been annealed using a JetFirst (Jipelec) rapid thermal annealer at 800℃ during 1 min.

Atomic Force Microscopy (AFM) was used to analyze the morphology of the sample surface. The AFM image of the surface morphology of the GaAsPN/Si tandem heterostructure on silicon substrate is presented below as Fig. 3-26.

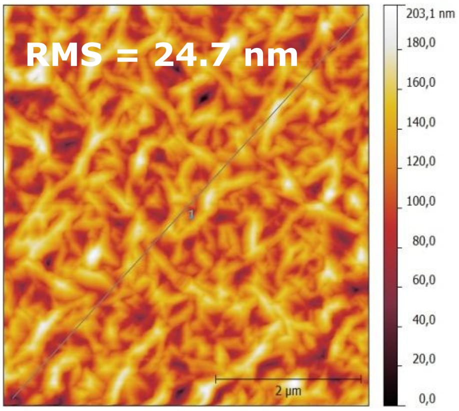

Fig. 3-26: AFM image of the surface morphology of the GaAsPN/Si tandem heterostructure on silicon substrate

The emerging defects (including APDs) in the AFM image above reveal a high roughness, result in a high r.m.s. surface roughness of 24.7 nm.

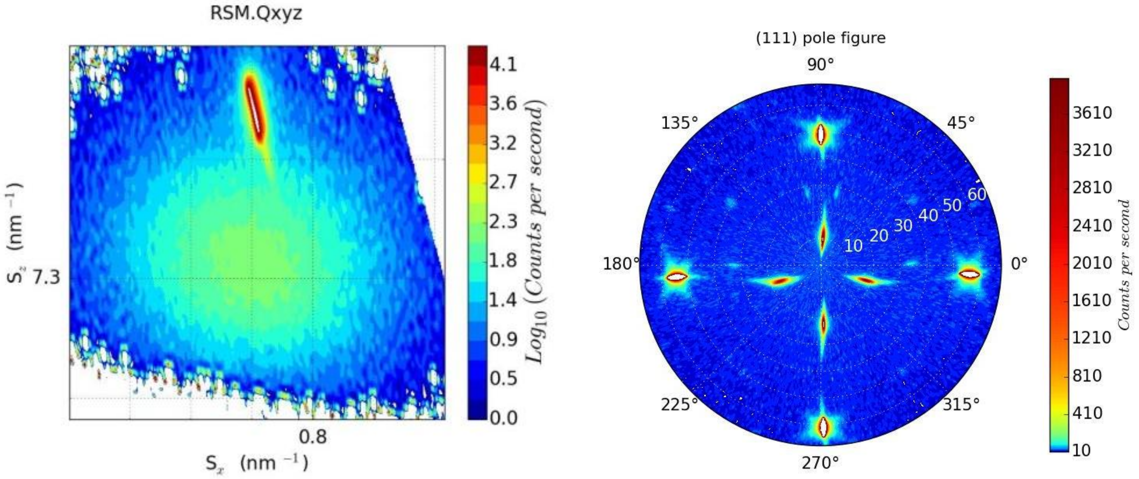

Fig. 3-27: X-ray diffraction measurements on the GaAsPN/Si tandem heterostructure on silicon substrate. Left: reciprocal space mapping around the (004) RLP. Right: Pole figure on the GaP/Si(111) Bragg peak.

Both the RSM and pole figure XRD measurements (Fig. 3.27) display typical XRD profiles of a fully relaxed sample (Fig 3-27 left) and displaying a huge density of microtwins (Fig 3-27 right), as can be observed through the additional reciprocal lattice points close to the pole figure center (at a Chi angle around 16 degrees). Considering the AFM image and the XRD measurements, we can conclude that the solar cell top junction contains a huge density of crystalline defects: antiphase boundaries, micro-twins, as well as relaxation dislocations. However, we have decided to perform some EQE and L-I-V measurements on this first GaAsPN/Si tandem cell.

The EQE measurements are performed to study the electro-optical properties of this first attempt. Fig. 3-28 gives the EQE results both versus Energy and wavelength. The total EQE of this tandem cell is almost the same as the EQE value given from the Si bottom subcell. We can remark that the EQE is over 60% at around 1.65 eV for the Si bottom subcell. Therefore, the contribution from the GaAsPN top subcell to the total EQE is negligible.

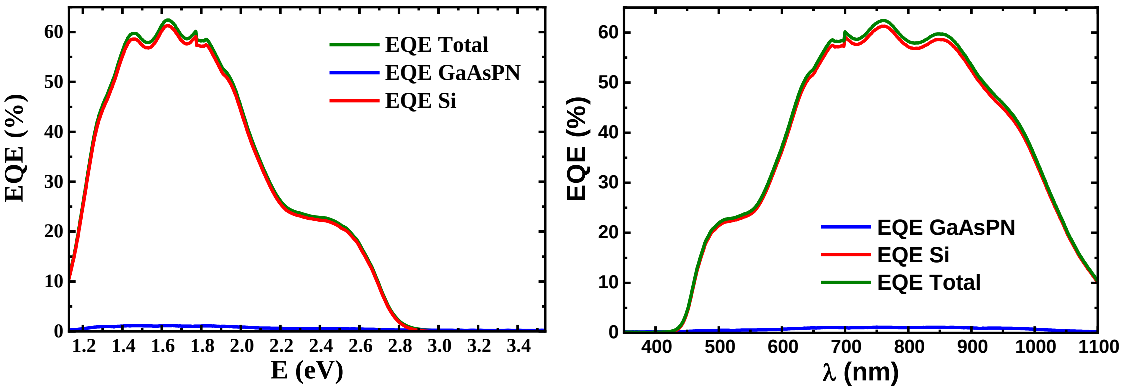

Fig. 3-28: external quantum efficiency (EQE) curves for the tandem solar cell in the top-bottom electrical contacts configuration, versus the Energy (left), and versus the wavelength (right). The green curve is from the overall EQE, while the red one is from the silicon bottom subcell and the blue one from the GaAsPN top subcell.

The I-V curves both under solar light illumination and in the dark are given below as Fig.3-29. The right one is in a logarithmic scale and the left one is in a linear scale. The V_{OC} is 0.28V and the J_{SC} is as large as 14.23 mA/cm^2. The value of the fill factor equals to 48.8%. And the efficiency reaches 1.96%. Therefore, the large value of the J_{SC} indicates that the current comes from the Si bottom subcell. Let us remind that in a tandem cell, the total electrical current is the current displayed by the subcell generating the lower current. Considering the EQE measurement and the fact that the GaAsPN does display only a very low signal, the L-I-V curve indicates therefore that the GaAsPN top subcell is likely shunted. This result is certainly due to the huge amount of structural defects, which is consistent with the low value of the V_{OC}.

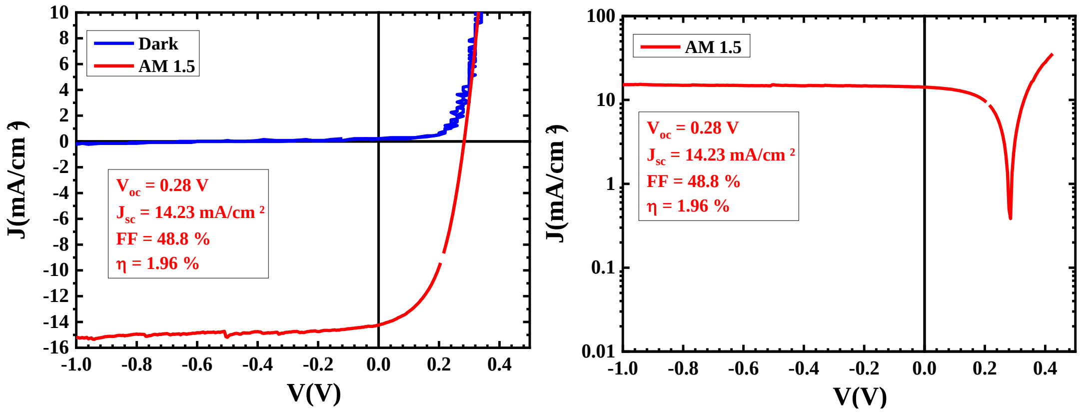

(a) (b)

Fig. 3-29: L-I-V and D-I-V curves: (a) in a linear scale; (b) in a logarithmic scale.

3.9. Conclusion

In this chapter, a GaP n-i-p photodiode grown on silicon substrate has been studied. It could serve as a top cell in the tandem cell structure onto silicon substrate. For both top-top and top-bottom electrical contacts, we obtain efficiencies equal to 1.48% and 0.77% respectively, which reach almost 18.5% of the theoretical efficiency value set by Shockley-Queisser limits. This top cell structure is suitable for the development of tandem cell onto silicon and any other III-V photonic devices onto silicon too.

For the first attempt of the GaAsPN/Si tandem cell, we have both the EQE and I-V results of this sample. The efficiency for this cell reaches 1.96% which is likely due to the huge amount of structural defects of the GaAsPN top cell, leading to an electrical shunt of this subcell. Therefore, an improvement of the MBE growth process would be necessary for the development of such tandem cells.

References:

[1] S. Almosni *et al.*, "Correlations between electrical and optical properties in lattice-matched GaAsPN/GaP solar cells," *Sol. Energy Mater. Sol. Cells*, vol. 147, pp. 53–60, Apr. 2016, doi: 10.1016/j.solmat.2015.11.036.

[2] O. Durand *et al.*, "Monolithic Integration of Diluted-Nitride III–V-N Compounds on Silicon Substrates: Toward the III–V/Si Concentrated Photovoltaics," *Energy Harvest. Syst.*, vol. 1, no. 3–4, pp. 147–156, Jan. 2014, doi: 10.1515/ehs-2014-0008.

[3] M. Da Silva *et al.*, "GaAsPN-based PIN solar cells MBE-grown on GaP substrates: toward the III-V/Si tandem solar cell," in *Physics, Simulation, and Photonic Engineering of Photovoltaic Devices IV*, Apr. 2015, vol. 9358, p. 93580H, doi: 10.1117/12.2081376.

[4] Y. Ping Wang *et al.*, "Quantitative evaluation of microtwins and antiphase defects in GaP/Si nanolayers for a III–V photonics platform on silicon using a laboratory X-ray diffraction setup," *J. Appl. Crystallogr.*, vol. 48, no. 3, pp. 702–710, Jun. 2015, doi: 10.1107/S1600576715009954.

[5] Y. Ping Wang *et al.*, "Abrupt GaP/Si hetero-interface using bistepped Si buffer," *Appl. Phys. Lett.*, vol. 107, no. 19, p. 191603, Nov. 2015, doi: 10.1063/1.4935494.

[6] A. Zhou *et al.*, "A study of the strain distribution by scanning X-ray diffraction on GaP/Si for III–V monolithic integration on silicon," *J. Appl. Crystallogr.*, vol. 52, no. 4, pp. 809–815, Aug. 2019, doi: 10.1107/S1600576719008537.

[7] A. Fave, J.-F. Lelièvre, T. Gallet, Q. Su, and M. Lemiti, "Fabrication of Si tunnel diodes for c-Si based tandem solar cells using proximity rapid thermal diffusion," *Energy Procedia*, vol. 124, pp. 577–583, Sep. 2017, doi: 10.1016/j.egypro.2017.09.281.

[8] M. Heidemann, S. Höfling, and M. Kamp, "(In,Ga)As/GaP electrical injection quantum dot laser," *Appl. Phys. Lett.*, vol. 104, no. 1, p. 011113, Jan. 2014, doi: 10.1063/1.4860982.

[9] A. . Baca, F. Ren, J. . Zolper, R. . Briggs, and S. . Pearton, "A survey of ohmic contacts to III-V compound semiconductors," *Thin Solid Films*, vol. 308–309, no. 1–4, pp. 599–606, Oct. 1997, doi: 10.1016/S0040-6090(97)00439-2.

[10] T. F. Lei, C. L. Lee, and C. Y. Chang, "Specific contact resistance of the Ni/Au Ge/nGaP system," *Solid. State. Electron.*, vol. 21, no. 2, pp. 385–391, Feb. 1978, doi: 10.1016/0038-1101(78)90268-X.

[11] K. K. Shih and J. M. Blum, "Contact resistances of Au Ge Ni, Au Zn and Al to III–V compounds," *Solid. State. Electron.*, vol. 15, no. 11, pp. 1177–1180, Nov. 1972, doi: 10.1016/0038-1101(72)90037-8.

[12] M. V. Tagare, T. P. Chin, and J. M. Woodall, "Nonalloyed ohmic contacts to heavily Be ‑ doped GaP and In x Ga 1− x P," *Appl. Phys. Lett.*, vol. 68, no. 24, pp. 3485–3487, Jun. 1996, doi: 10.1063/1.115766.

[13] W. A. Brantley, B. Schwartz, V. G. Keramidas, A. K. Sinha, and G. W. Kammlott, "Modified Contact Metallizations for GaP to Provide Barrier Action Against

Gallium Migration," *J. Electrochem. Soc.*, vol. 122, no. 8, pp. 1152–1154, Aug. 1975, doi: 10.1149/1.2134415.

[14] J. Pfeifer, "Ohmic contact to p-type GaP," *Solid. State. Electron.*, vol. 19, no. 11, pp. 927–929, Nov. 1976, doi: 10.1016/0038-1101(76)90104-0.

[15] L. Baojun, L. Enke, and Z. Fujia, "Pd/Zn/Pd ohmic contacts to p-type GaP," *Solid. State. Electron.*, vol. 41, no. 6, pp. 917–920, Jun. 1997, doi: 10.1016/S0038-1101(96)00203-1.

[16] F. Zhang, D. Zhang, B. Li, E. Liu, F. Liu, and R. Gan, "Pb/Zn/Pd ohmic contacts to p-GaP," *Mater. Sci. Eng. B*, vol. 48, no. 3, pp. 198–201, Aug. 1997, doi: 10.1016/S0921-5107(97)02054-0.

[17] J.-P. Gauthier *et al.*, "Electrical injection in GaP-based laser waveguides and active areas," in *26th International Conference on Indium Phosphide and Related Materials (IPRM)*, May 2014, no. V, pp. 1–2, doi: 10.1109/ICIPRM.2014.6880545.

[18] T. Soga, T. Jimbo, and M. Umeno, "Dislocation generation mechanisms for GaP on Si grown by metalorganic chemical vapor deposition," *Appl. Phys. Lett.*, vol. 63, no. 18, pp. 2543–2545, Nov. 1993, doi: 10.1063/1.110427.

[19] S. Suckow, "2/3-Diode Fit (2014)." http://nanohub.org/resources/14300.

[20] Keith Reid McIntosh, "Lumps, Humps and Bumps: Three Detrimental Effects in the Current-Voltage Curve of Silicon Solar Cells," University of New South Wales Sydney Australia, 2001.

[21] C. McDonald *et al.*, "Zero-dimensional methylammonium iodo bismuthate solar cells and synergistic interactions with silicon nanocrystals," *Nanoscale*, vol. 9, no. 47, pp. 18759–18771, 2017, doi: 10.1039/C7NR05764D.

[22] B. G. Mendis *et al.*, "Nanometre-scale optical property fluctuations in Cu2ZnSnS4 revealed by low temperature cathodoluminescence," *Sol. Energy Mater. Sol. Cells*, vol. 174, no. March 2017, pp. 65–76, Jan. 2018, doi: 10.1016/j.solmat.2017.08.028.

[23] D. E. Aspnes and A. A. Studna, "Dielectric functions and optical parameters of Si, Ge, GaP, GaAs, GaSb, InP, InAs, and InSb from 1.5 to 6.0 eV," *Phys. Rev. B*, vol. 27, no. 2, pp. 985–1009, Jan. 1983, doi: 10.1103/PhysRevB.27.985.

[24] W. Shockley and H. J. Queisser, "Detailed Balance Limit of Efficiency of p‐n Junction Solar Cells," *J. Appl. Phys.*, vol. 32, no. 3, pp. 510–519, Mar. 1961, doi: 10.1063/1.1736034.

[25] S. Rühle, "Tabulated values of the Shockley–Queisser limit for single junction solar cells," *Sol. Energy*, vol. 130, pp. 139–147, Jun. 2016, doi: 10.1016/j.solener.2016.02.015.

[26] P. Bellanger, A. Minj, A. Fave, Z. Djebbour, S. Roques, and A. Slaoui, "Silicon Tunnel Junctions Produced by Ion Implantation and Diffusion Processes for Tandem Solar Cells," *IEEE J. Photovoltaics*, vol. 8, no. 6, pp. 1436–1442, Nov. 2018, doi: 10.1109/JPHOTOV.2018.2864632.

[27] F. Gérenton, F. Mandorlo, J.-B. Brette, and M. Lemiti, "Pattern of Partial Rear Contacts for Silicon Solar Cells," *Energy Procedia*, vol. 77, pp. 677–686, Aug. 2015, doi: 10.1016/j.egypro.2015.07.097.

[28] F. Gérenton, F. Mandorlo, E. Fourmond, M. Le Coz, D. Blanc-Pélissier, and M. Lemiti, “Laser ablation compatible substoichiometric SiO x /SiN y passivating rear side mirror for passivated emitter and rear thin-film crystalline silicon solar cells,” *J. Vac. Sci. Technol. A Vacuum, Surfaces, Film.*, vol. 34, no. 5, p. 051201, Sep. 2016, doi: 10.1116/1.4958985.

Chapter 4 Towards hot carrier solar cells – Design of selective contacts

Hot carrier solar cells are one of the third generation photovoltaic devices, which offer the opportunity to harvest more solar energy than the limit (33%) set by the Shockley-Queisser model. Unlike classical photovoltaic devices, in hot carrier solar cells the excess kinetic energy is converted into useful electric power rather than being lost through thermalization mechanisms. To extract the carriers while they are still “hot”, we need to develop efficient energy selective contacts. In this chapter, we investigate a set of HCSC with two different contacts (a semi-selective barrier and a selective single quantum well) to study the extraction of the hot carriers from the two contacts. First we simulate different HCSC structures with SimWindows. Then we investigate the real samples made on InP (001) substrate, with AlInAs barrier serving as the semi-selective contact and AlInAs-InGaAs-AlInAs single quantum well serving as the selective contact.

4.1. Principles of selective contacts

4.1.1. Objectives and context of the study

The study of semi-selective and selective contacts for hot carrier solar cells is performed in the framework of the ICEMAN ANR project. The ambitious objectives of this project are summarized hereafter.

“Ultra-thin absorbers and selective contacts are designed and fabricated to reach a voltage gain of 50mV under 1000 SUNS; with an effective-Seebeck coefficient of 300µV/K. Nanophotonic structures are added on the solar cell to obtain an integrated power absorption over the absorber band gap of more than 85%. All these improvements may induce more than 80% efficiency carrier collection through energy selective contacts at 1000 SUNS.”

Among several semiconducting based materials to fabricate multiple wells (MQWs) structures (GaSb based, InGaAs-based…), the InGaAsP-based structures allow for obtaining both high carrier temperature and sufficient design flexibility (ratio between quantum well and barrier widths and absorber thickness); this absorber material is chosen for the ICEMAN project. Energy selective contacts are based on multi quantum wells, which present the advantage of reliability, and ease the control of energy extraction by varying the material composition and/or dimension. Such selective contacts lead to the Negative Differential Resistance (NDR) effect. These structures can be adjusted by a suitable asymmetry so that high transmissions are achieved at the desired bias.

The study of selective contacts is divided in two steps. First, a type II alignment creates a semi-selective contact. Then, this type II alignment is replaced by a double barrier resonant tunneling diode with AlInAs/GaInAs quantum well heterostructures lattice-matched with InP. The advantage is to maintain a common V element, which is easier to grow. Adjustment of the composition, as well as the well/barrier thickness ratio allows obtaining the appropriate energy level value inside the well.

4.1.2. Physical principles

The important property of HCSC is not only the inhibiting of carrier cooling process, but also the extraction whilst they are still at elevated energies. A hot carrier cell must only allow extraction of hot carriers through contacts that accept only a very narrow range of energies (energy selective contacts, ESCs). The ESCs are essential to prevent cold carriers in the contact from cooling the extracted hot carriers, i.e., the increase in entropy on carrier extraction is minimized[1]. While the realization of extraction of carriers from hot carrier absorber is practically difficult.

ESCs can be realized by the purely quantum phenomenon of resonant tunneling. This effect exists if electron-reflecting interfaces are closely spaced, i.e., with separations comparable to the electron wavelengths. Interference between different electron waves leads to discrete transmission peaks. So, one practical implementation of the requirement for a narrow range of contact energies is an energy selective contact based on double barrier resonant tunneling. Tunneling to the confined energy levels in a quantum dot layer embedded between two dielectric barrier layers, can give a conductance sharply peaked at the line up of the Fermi level on the ‘hot’ absorber side of the contact with quantum dot confined energy level. Conductance both below this energy and above it should be very significantly lower. This is the basis of the current work on double barrier resonant tunneling ESCs.

ESCs for a hot carrier solar cell can be implemented using different materials and structures. The main property that needs to be achieved is precise energy selectivity in carrier extraction. Among the different possible material configurations, group IV and group III-V double barrier resonant tunneling structures look to be the most promising. ESCs for a III-V based hot carrier cell can be realized using a QW structure in a double barrier structure, probably requiring either MBE or MOVPE growth. Modelling results have shown that, for a hot carrier cell based on an InN absorber, the optimum configuration for ESCs is constituted by an InN/$In_xGa_{1-x}N$ double-barrier structure[2].

In general the optimal extraction energy for electrons and holes is different, due to the different values of effective mass. Thus, the hole ESC QW should be physically thinner and have a higher barrier than the electron ESC QW to achieve similar currents at reasonable extraction energies, as illustrated in Figure 4-1.

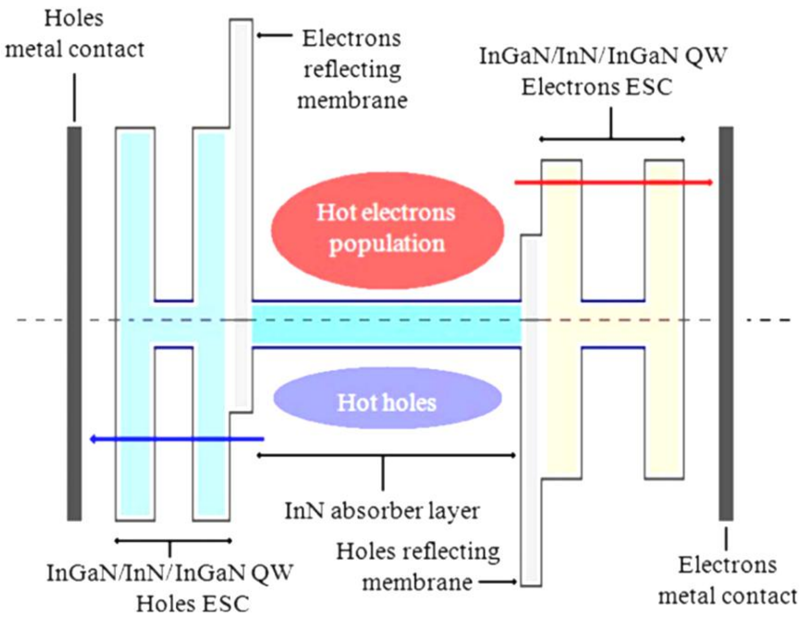

Fig. 4-1: Schematic of a hot carrier solar cell based on an InN absorber and InN/InGaN ESCs[3].

4.2. Design and simulation

4.2.1. Design of the samples

The study of selective contacts is an important step towards the development of HCSC. As explained in the ICEMAN project description, we study InGaAs/AlInAs type II heterojunction as a selective contact. To define the composition of the samples, we first perform basic simulations for two different types of selective contacts to obtain their band diagrams: one structure has a barrier acting as a semi-selective filter (high pass filter), the other structure has a single quantum well acting as a resonant tunneling contact (selective contact). This simulation study will help us to choose the characteristics of the real samples studied in the experimental part.

The structures of the two samples are shown below as Fig. 4-2 and Fig.4-3. Both samples are PIN diodes grown on InP substrate and are fully lattice matched to InP. A etch stop zone in InGaAs allows to perform the final study in ICEMAN project: removing the substrate and replace it by a dielectric mirror to improve absorption (which will be done by C2N in the ICEMAN project). The intrinsic zone named “absorber” is InGaAs. A future type of samples more adapted to the experimental setup of the partners will have an absorber in quaternary alloy InGaAsP but due to technical problems, these samples are not grown yet. P-doped layer is also in InGaAs but a AlInAs barrier is grown between absorber and p-InGaAs to perform hole selective contact. The n-doped layer is made of n++ InP over the etch stop layer. The n-selective contact is performed by an AlInAs barrier, with or without an InGaAs quantum well, purpose of this chapter.

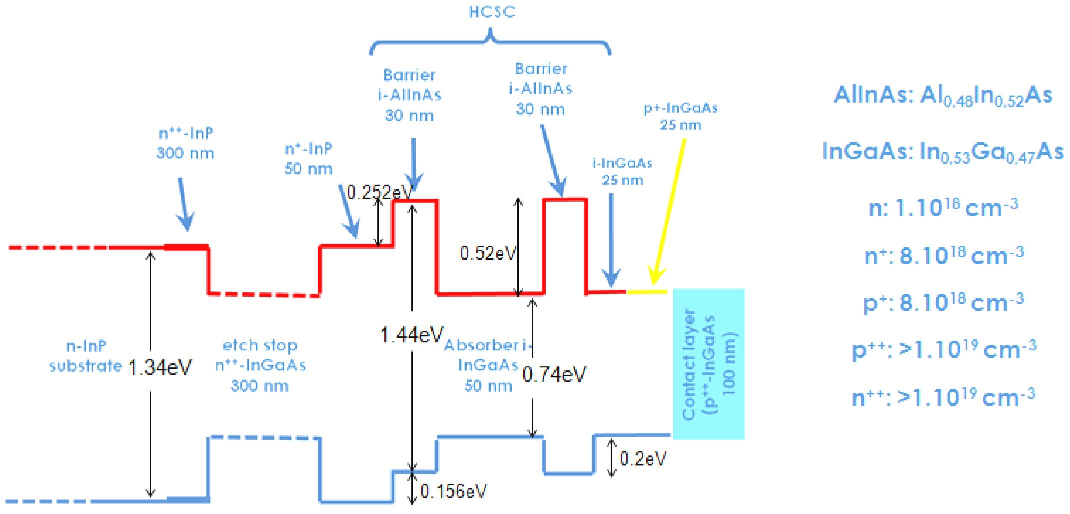

Fig. 4-2: Band line-up of Sample HCSC-Barrier, with a 30nm-thick AlInAs barrier as

the semi-selective contact on the n-side.

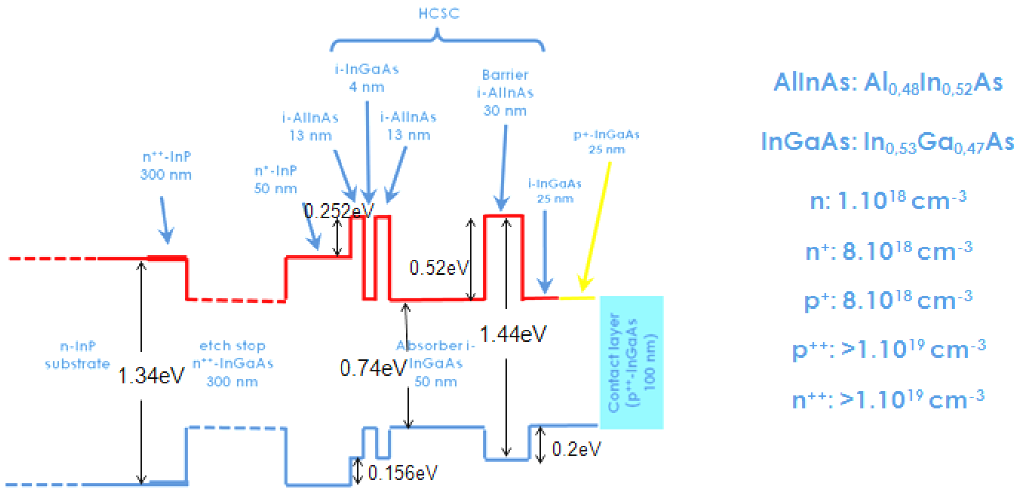

Fig. 4-3: Band line-up of Sample HCSC-SQW, with a 13nm-4nm-13nm AlInAs-InGaAs-AlInAs single quantum well as the type N selective contact.

The band line-ups are extracted from Vurgaftman database [4]. Table 4.1 summarizes the band structure parameters used to simulate the devices.

	Bandgap E_G (eV)	Electronic affinity χ (eV)	Electron effective mass m_e^* (m_0)	Hole effective mass m_h^* (m_0)
InP	1.35	3.681	0.080	0.45
InGaAs	0.74	3.943	0.043	0.53
AlInAs	1.45	3.421	0.076	0.55

Table 4.1: Parameters of simplified energy band diagram for InP, InGaAs and AlInAs[4]

4.2.2. Device simulation results

We use SimWindows to simulate both structures with different absorber thickness, different doping levels, and under different light conditions (dark and AM1.5G). The aim is the optimization of the HCSC simplified structure in order to guide the structure elaboration with two main objectives: improve the absorber to obtain enough carriers which can be extracted and study the selective contacts (one barrier and one SQW).

Firstly, I present the band diagrams of the two different structures both under dark and under illumination, the carrier concentrations are also presented for comparison (see Fig. 4-4 to 4-9). Secondly comes the band diagram simulations for two different p-covers (InP and InGaAs) of Sample-HCSC-Barrier (see Fig. 4-10 and 4-11). Thirdly, the InGaAs absorber thickness of Sample-HCSC-Barrier is studied (see Fig. 4-12). And then the AlInAs barrier doping levels of Sample-HCSC-Barrier is presented (see Fig. 4-13).

- *Simulation results for the final structures used to fabricate the real samples:*

The band diagrams of the two different structures both in dark are presented below (Fig.4-4, Fig.4-5), and under illumination (Fig.4-6, Fig.4-8). The energy scale takes the vacuum level as a reference point of the origin and the position scale is from 0.3 μm to 0.51 μm because the thickness of the InP substrate is 0.35 μm and the top layer ends at 0.51 μm.

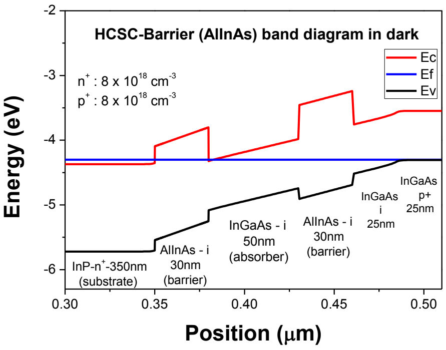

Fig. 4-4: Band diagram of Sample HCSC-Barrier in dark.

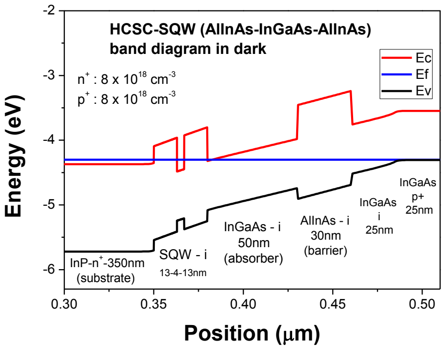

Fig. 4-5: Band diagram of Sample HCSC-SQW in dark.

Both samples HCSC-Barrier and HCSC-SQW are p-i-n diodes, with p side on the right (p-doped InGaAs) and n side on the left (n-doped InP) (substrate). The intrinsic area is in the middle which has a slope for both valence band (black line in the Fig.4-4 and Fig. 4-5) and conduction band (red line in the Fig. 4-4 and Fig. 4-5). The constant blue lines in the Fig. 4-4 and Fig. 4-5 stand for Fermi level, which is under equilibrium with no light, assuming there is no carrier generated without light.

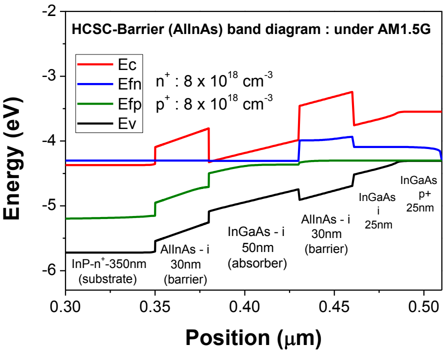

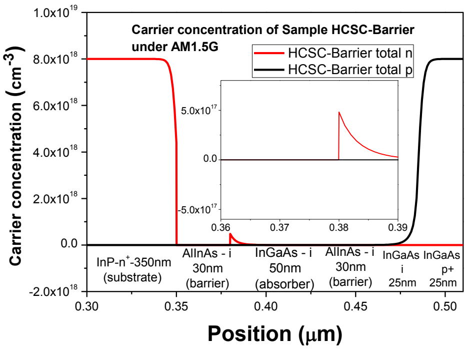

Fig. 4-6: Band diagram of Sample HCSC-Barrier under illumination (AM 1.5G).

Fig. 4-7: Carrier concentration of Sample HCSC-Barrier under illumination.

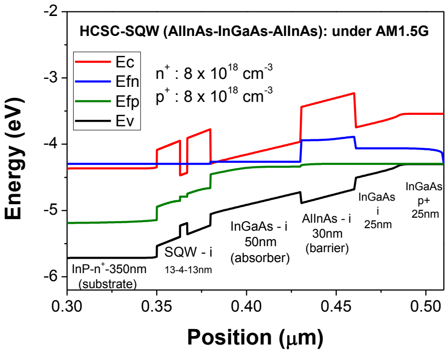

Fig. 4-8: Band diagram of Sample HCSC-SQW under illumination (AM 1.5G).

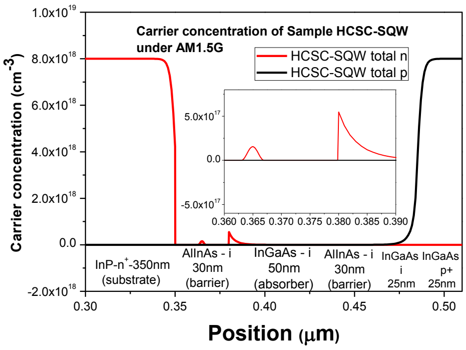

Fig. 4-9: Carrier concentration of Sample HCSC-SQW under illumination.

Under illumination, the Fermi level is no longer constant, and two quasi-Fermi levels (QFL) are defined, one for holes E_{FP} and one for electrons E_{FN}. The quasi-Fermi level splitting is linked to the maximum open-circuit voltage that a solar cell fabricated from that material can achieve.

We can see the quasi-Fermi level splitting when the samples are both under illumination. The blue lines in the figures stand for E_{FN}, the yellow lines in the figures stand for E_{FP}. On the left n-part of the diode (InP n+ substrate), the carrier density is linked to the distance between quasi-Fermi levels and the band edges, which has been presented in Chapter 2 section 2.5. See the following equations as formula (2.12) and (2.13) which recall the link between electron ($\eta_c(x)$) and hole ($\eta_\upsilon(x)$) Plank potentials and quasi-Fermi levels.

$$\eta_c(x) = \big(E_{fn}(x) - E_c(x)\big) / \, kT_n(x) \tag{2.12}$$

$$\eta_\upsilon(x) = \Big(E_\upsilon(x) - E_{fp}(x)\Big) \, / \, kT_p(x) \tag{2.13}$$

The distance between E_{FN} and E_c is far less than the distance between E_{FP} and E_v, which means the carrier density of electrons is much higher than holes in this area. And on the right p-part of the diode (InGaAs p+ p-cover), the distance between E_{FN} and E_c is much larger than the distance between E_{FP} and E_v, which means the carrier density of holes is much higher than electrons in this area. As shown in Fig. 4-7 and Fig. 4-9. We can also notice that there is a small amount of carrier concentration in the left part of zoom-in figure inside Fig.4-9 around 0.365 μm, while there is no carrier concentration at the same position of Fig. 4-7. This contribution of the carrier concentration is linked to the single quantum well: the electron QFL is aligned with the first confined state in the quantum well.

Electrons and holes are generated in the InGaAs absorber as we expected, and also in the doped layers but they recombine rapidly.

- *Simulation results for the Sample HCSC-Barrier with two different p-covers (InP and InGaAs):*

The band diagram of Sample HCSC-Barrier with a p-cover of InP is presented below under illumination, see Fig.4-10.

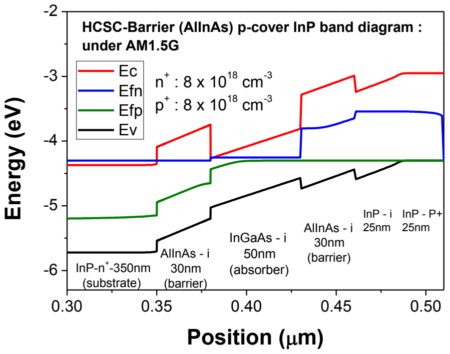

Fig. 4-10: Band diagram of Sample HCSC-Barrier under illumination (AM 1.5G).

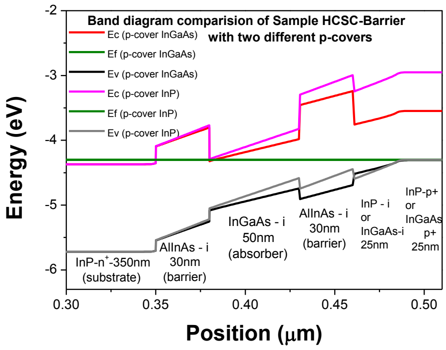

Fig. 4-11: Band diagrams of the simplified HCSC-Barrier structure with two different p-covers in dark, without contact.

The slope of the intrinsic area stands for the value of electric field. The InP cover induces a larger electric field but the hole extraction can be limited. According to this simulation step, we decide to choose the InGaAs as the p-cover to have a better alignment with the InGaAs absorber, and to enhance the extraction of the holes. As a result, all simulations after are all with the p-cover of InGaAs.

- *Simulation results for the Sample HCSC-Barrier with different absorber thickness (30nm, 50nm, and 100nm):*

Then, we simulated on different absorber thickness (30nm, 50nm, and 100nm) of the HCSC-Barrier sample. Fig.4-12 is the band line-ups with three different absorber thicknesses.

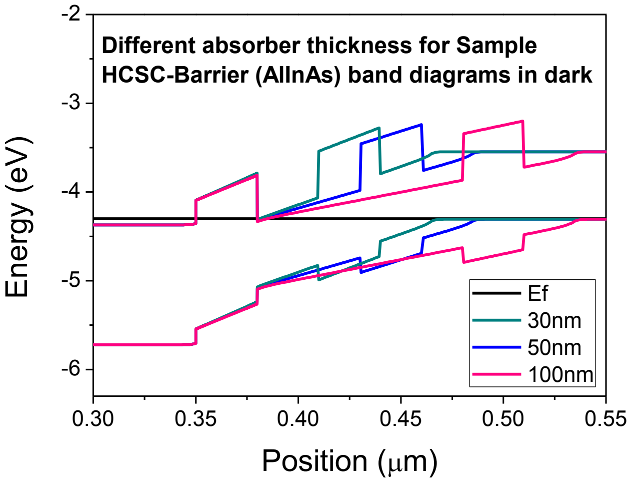

Fig. 4-12: Electronic band line-ups of the simplified HCSC-Barrier structure with a barrier as a semi-selective contact, in the dark.

The 30nm-thick InGaAs absorber has a steeper slope than the 100nm-thick InGaAs absorber. In the middle position of each absorber the values of electrical field are: 81 kV/cm (30 nm-absorber at 0.395 μm), 67 kV/cm (50 nm-absorber at 0.405 μm) and 45 kV/cm (100 nm-absorber at 0.43 μm). The values of electrical field are inversely proportional to the absorber thickness.

To separate the generated electron and hole pairs, we need large electric field which means steeper slope, which means thinner absorber thickness. While we also need larger size of the absorber to generate more electron and hole pairs. As the three slopes are proportional to each other as expected, we propose to choose the middle value of 50nm as the thickness of the InGaAs absorber for both Sample HCSC-Barrier and Sample HCSC-SQW.

- *Simulation results for the Sample HCSC-Barrier with different doping levels of the AlInAs barrier :*

Different barrier doping levels (AlInAs) for Sample-HCSC-Barrier are also studied.

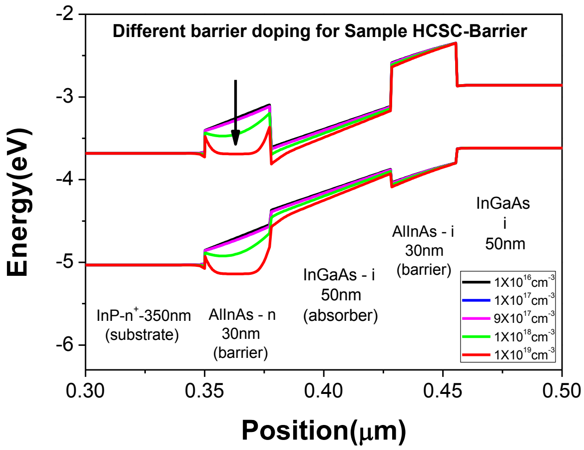

Fig. 4-13: Electronic band line-up of the Sample-HCSC-Barrier with a barrier as a semi-selective contact, in the dark;

We simulated different doping levels for the AlInAs barrier of Sample HCSC-Barrier. We applied 1 x 10^{16} cm^{-3}, 1 x 10^{17} cm^{-3}, 9 x 10^{17} cm^{-3}, 1 x 10^{18} cm^{-3}, and 1 x 10^{19} cm^{-3}, five different doping levels to see the differences of their band diagrams. For doping levels below 1 x 10^{18} cm^{-3}, there is no big difference appeared in the doped AlInAs area, while when it gets over this value, the barrier becomes smaller and smaller with the increase of doping levels. From Fig. 4-13 we can see clearly that with a heavy doping, the barrier would finally disappear, so we decide not to dope this barrier layer to keep the AlInAs barrier effective. Undoped layers are also easier to grow with MBE setup.

- *Sample structure improvements (changing absorber material into InGaAsP):*

As we all know, InGaAsP has a larger bandgap than InGaAs, our Sample HCSC-Barrier and HCSC-SQW both have a InGaAs absorber bandgap of 0.74eV. The InGaAsP absorber that we want to investigate has a bandgap of 0.89eV. The ICEMAN project partners in Paris use an InGaAs photodetector equipment to exhibit hot carrier effect from opto-electrical measurements. This detector is efficient for energies over 0.8 eV so we plan to grow the same samples with an InGaAsP absorber.

We also performed SimWindows simulation with this InGaAsP absorber which bandgap energy is suitable for our partners. We conclude from the band diagrams both in the dark and under illumination and the electric field results that no big difference showed up when we change the absorber from InGaAs into InGaAsP. That is to say, it is ok to fabricate real samples with MBE using the InGaAsP absorber.

All simulation results helped to make the final structure of the real samples fabricated through MBE. Further high level simulations like described in [5] would help to design more efficient selective contacts but this experimental study is a first step.

4.3. Device presentation and structural characteristics

4.3.1. Device presentation

The detailed fabrication steps are already presented in Chapter 2, Figure 4-14 is the pictures of the Sample HCSC-Barrier (on the left) and Sample HCSC-SQW (on the right) taken just after the MBE growth.

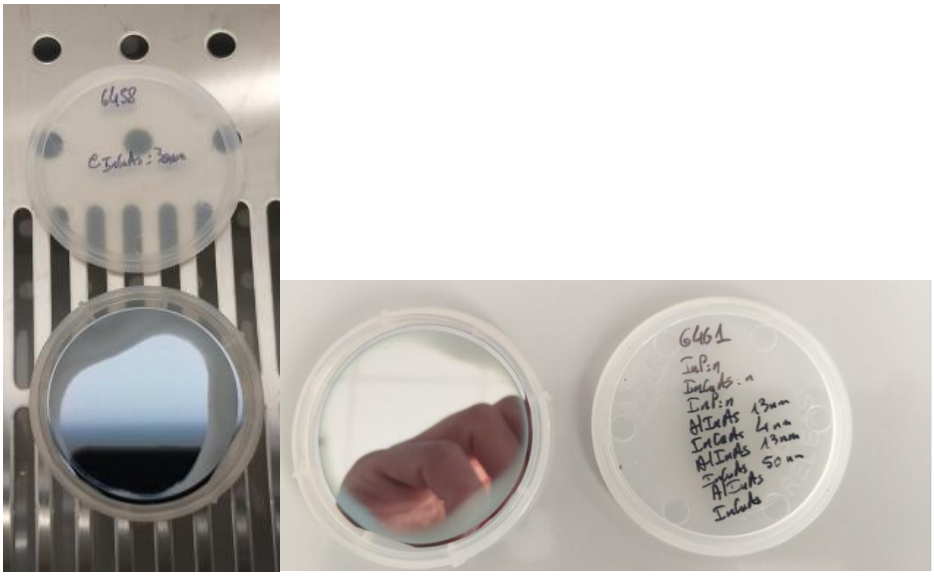

Fig. 4-14: Pictures of Sample HCSC-Barrier (on the left) and Sample HCSC-SQW (on the right) taken just after the MBE growth.

From the pictures above we can see that the middle of the sample presents a mirror effect while the surface is quite rough at the edges. Therefore, the middle of the samples will be preferred for technological process.

The picture of the final devices fabricated in the clean room is presented below as Fig.4-15 (a), the steps of fabrication are presented in Chapter 2. Fig. 4-15 (b) shows a microscope view to give a clearer look of the diodes.

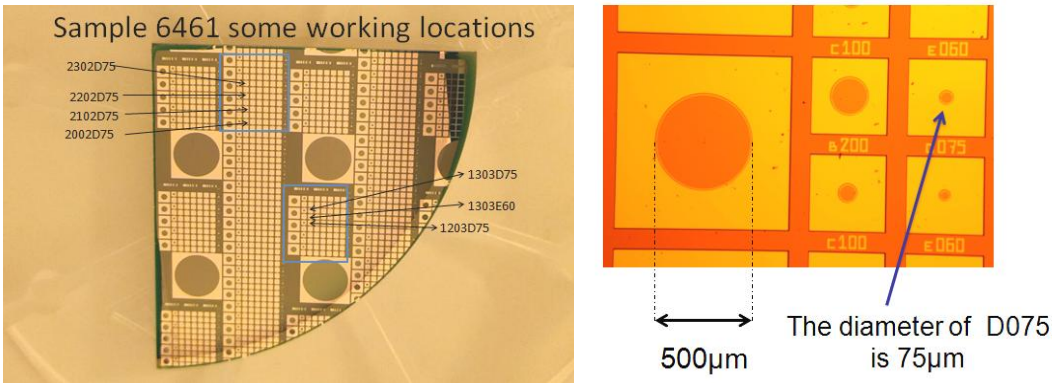

(a) (b)

Fig. 4-15: Pictures of the device corresponding to Sample HCSC-SQW, (a) picture with some working locations marked; (b) enlarged picture with the dimension of the selected device, which has a diameter of 75 µm.

Dark I-V measurements have been performed on a large number of diodes but a lot of them showed bad contact with no current. The devices marked on the picture (2302D75, 2202D75, 2102D75, 2002D75, 1303D75, 1303E60, 1203D75) had good enough characteristics to perform I-V measurements under solar simulator and photocurrent measurements. The diameter of the ‘D’ devices is 75µm, and the diameter of the ‘E’ device is 60 µm. The reason why there are only a few working points is because the lacking of the uniformity during the MBE growth process. We can also notice that the working points are concentrated in a small area together not separated over the whole sample.

4.3.2. Structural characteristics

X-ray diffraction analyses have been done on both the HCSC heterostructures.

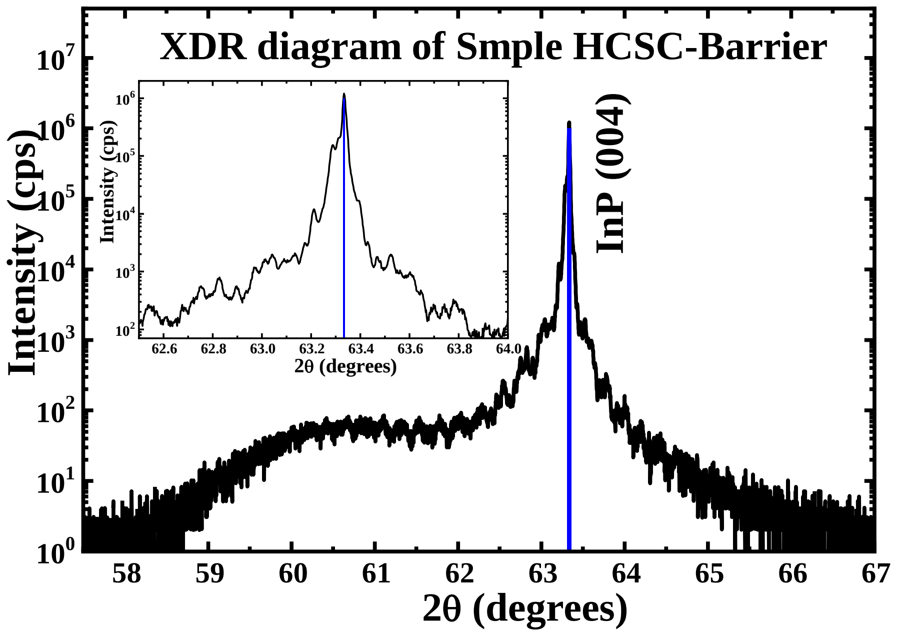

Fig. 4-16: X-ray diffraction result of Sample HCSC-Barrier

For the Sample HCSC-Barrier, the main diffraction peaks coming from the InGaAs and AlInAs layers are very close to the InP (004) substrate diffraction peak (the blue line in the figure) meaning that the heterostructure is almost lattice-matched as expected (Fig. 4-16). The GaInAs peak position has been measured at 6.8155 nm^{-1} which corresponds to a interreticular distance of 0.58690 nm. Therefore, considering the strain on the InP substrate, the In composition is equal to 0.533 (very close to the required 0.53 amount of In).

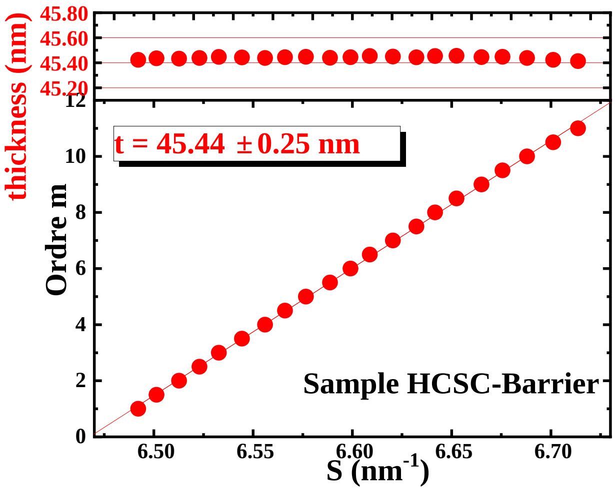

Fig. 4-17: Thickness fringes of Sample HCSC-Barrier.

Moreover, some thickness fringes are seen at the left of the substrate peak. The slope of fringe order m as a function of the fringe position expressed into scale of the diffraction vector modulus S = (2 sin θ) / λ yields the corresponding thickness. This slope gives a thickness around 45 nm-46 nm (Fig. 4-17). This thickness, around 50 nm can be due either to the top (i-InGaAs 25 nm/ p+-InGaAs 25 nm) layer, either the 50 nm nominally thick InGaAs absorber, or the 50 nm nominally thick n+ InP layer (localized between the n++-InGaAs etch-stop layer and the AlInAs barrier). An etching of the p-doped InGaAs top layers has been done (to check the PL peak position of the InGaAs absorber layer, without a parasitic free-carriers absorption due to the doped top layers) and the XRD pattern displays again the 45 nm-46 nm thickness fringes. Moreover, we have also grown a similar sample with an absorber thickness of 7.4 nm (results not shown here) and its XRD pattern displays also the same thickness fringes system. Therefore, we attribute this thickness to the 50 nm nominally thick n+ InP layer.

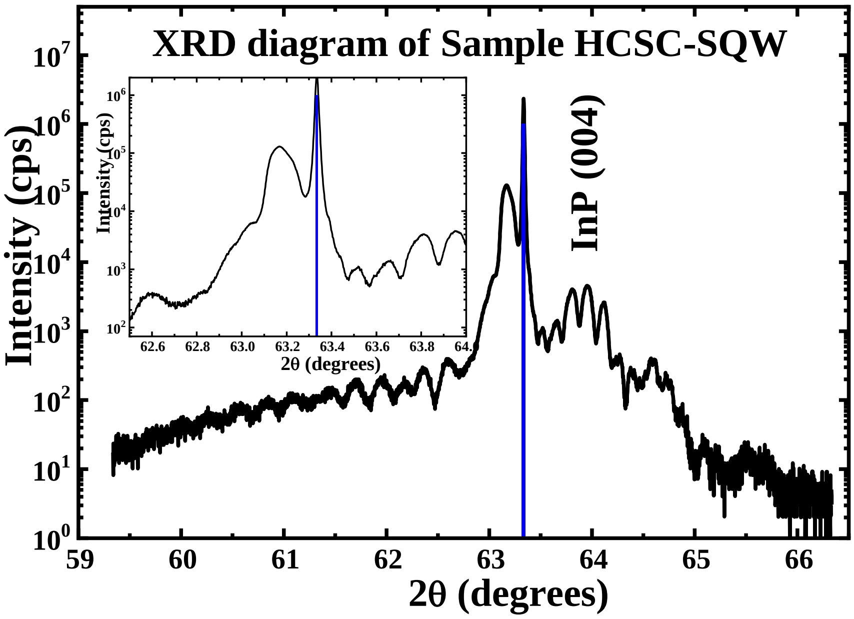

Fig. 4-18: X-ray diffraction result of Sample HCSC-SQW

Considering now the sample HCSC-SQW (with a SQW as a selective contact) and as shown in Fig. 4-18, the GaInAs peak position has been measured at 6.80084 nm^{-1} which corresponds to a inter-reticular distance of 0.58816 nm. Therefore, considering the strain on the InP substrate, the In composition is equal to 0.548 (again, close to the required 0.53 amount of In).

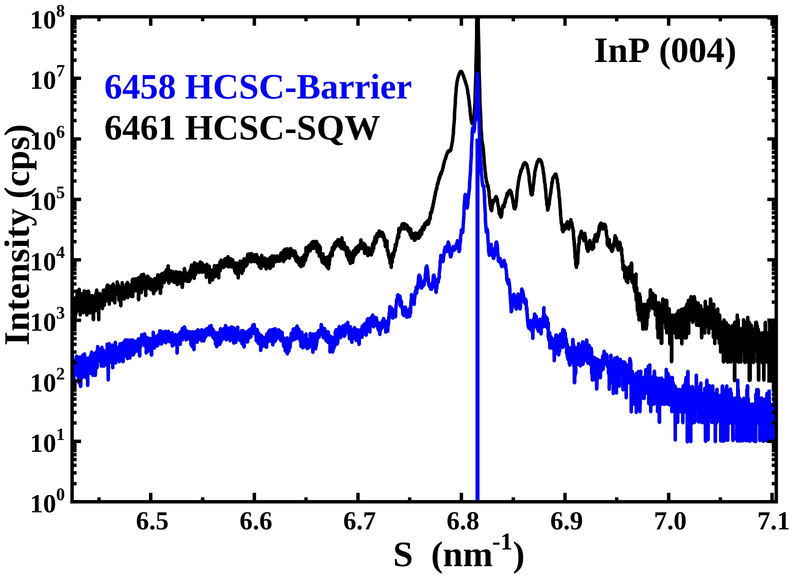

Fig. 4-19: Comparison of X-ray diffraction results between Sample HCSC-Barrier and Sample HCSC-SQW.

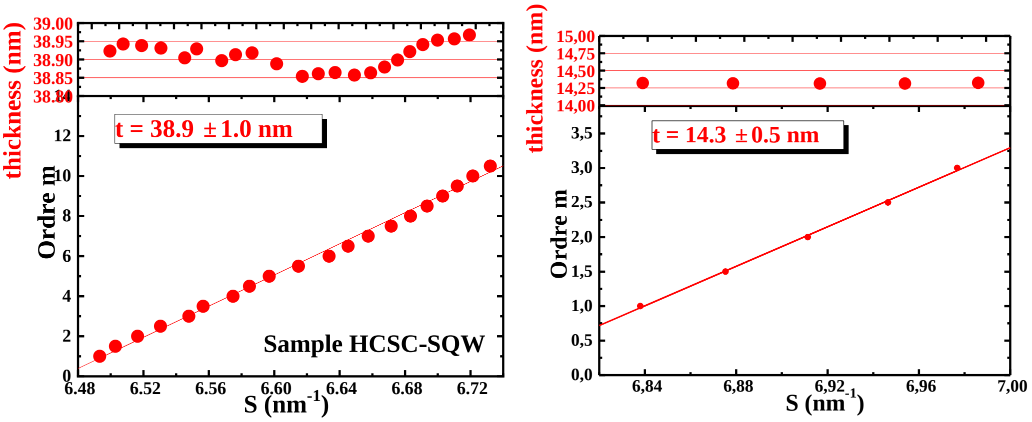

Fig. 4-20: Thickness fringes of Sample HCSC-SQW. Left: to the left of the InP diffraction peak, and right: to the right of the InP diffraction peak.

As can be seen in Fig.4-19, the thickness fringes system is always present at the left of the InP (004) diffraction peak, the giving 39 nm (Fig.4-20), a thickness a little bit lower than the nominal 50 nm-thick. A new thickness fringes system is also present at the right of the InP (004) diffraction peak, which gives a thickness around 14 nm. We attribute this contribution to the 13 nm nominally-thick AlInAs barriers surrounding the InGaAs SQW.

4.3.3. Photoluminescence results

Photoluminescence (PL) experiments have been performed on sample-HCSC-Barrier (6458). Since the sample is p-i-n diodes, the upper p-doped part has been etched by RIE to avoid the electrical field effect. However, we are not sure that all the p-doped part is all etched off, but the etching has been sufficient to perform the PL measurement. The PL experiment details are the following:

The applied laser wavelength is 532nm (green) with a power of 100 mW and the integration time is 1 second, average time is 20 seconds.

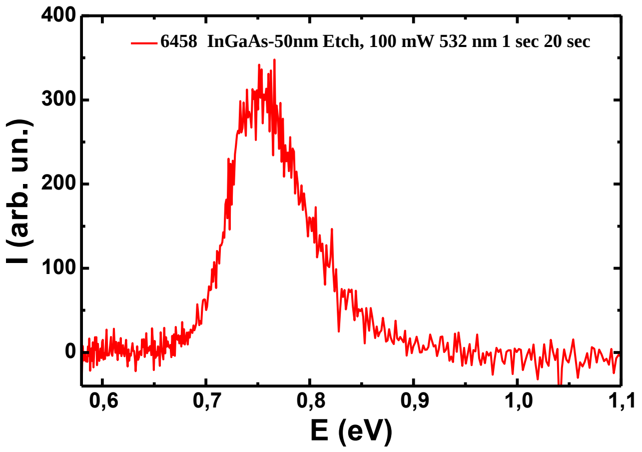

Fig. 4-21: Photoluminescence spectrum of Barrier sample

Position of the PL peak is around 0.755eV (1650nm), which corresponds to the 0.74eV bandgap energy expected for the $In_{0.53}Ga_{0.47}As$. Even if the PL intensity is very low compared to classical InGaAs/InP samples, the PL peak position confirms the quality of InGaAs.

All these structural characteristics present good enough results to process the samples and obtain photodiodes. The following part presents opto-electrical measurements performed on the diodes after technological process presented in chapter 2 section 2.2.2.

4.4. Opto-electrical results

The aim of this part is to explore the effect of the InGaAs quantum well on opto-electrical properties of the photodiodes. Opto-electrical measurements presented in this part have been performed on two circular diodes with a 75-μm diameter. Sample-HCSC-Barrier stands for the diode number 1402D075 of the wafer number 6458, with semi-selective contacts: two AlInAs barriers. Sample-HCSC-SQW stands for the diode number 2302D075 of the wafer number 6461, with an InGaAs quantum well in the AlInAs barrier on n-side. We first present electrical characteristics obtained under solar simulator and then photocurrent measurements with two lasers of different wavelengths. The corresponding energies are 1.16 eV, under the bandgap of AlInAs and 2.32 eV, over this bandgap. We demonstrate a better carrier extraction with the SQW sample than with the barriers.

4.4.1. Electrical characteristics

J-V measurements have been performed to study the electrical characteristics of both samples. Fig. 4-22 and 4-23 present electrical characteristics of the two samples, obtained under solar simulator (AM1.5G without concentration). Table 4.2 summarizes the electrical characteristics of the studied diodes.

The applied solar power density during the experimental is 960W/m^2, equals to 96mW/cm^2.

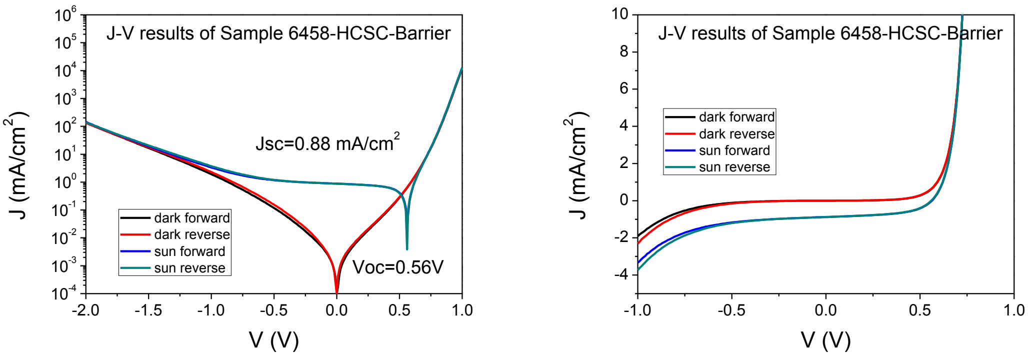

(a) (b)

Fig. 4-22: I-V results for Sample-HCSC-Barrier under solar spectrum (AM1.5G): (a) in a logarithmic scale for voltage; (b) in a linear scale for voltage.

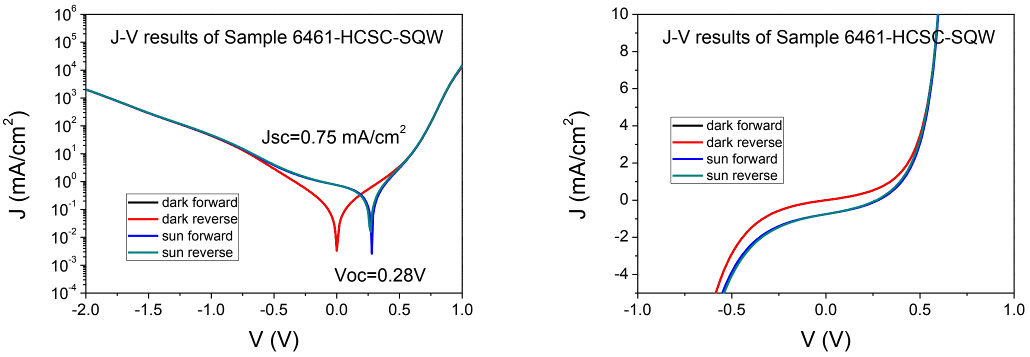

(a) (b)

Fig. 4-23: I-V results for Sample-HCSC-SQW under solar spectrum (AM1.5G): (a) in a logarithmic scale for voltage; (b) in a linear scale for voltage.

Unlike Fig. 3-16 (a) and Fig. 3-25 (a), one can notice that the forward curve and reverse curve in the figures above have the same shape (Fig. 4-22 and Fig. 4-23).

The J_{SC} given by Sample-HCSC-Barrier is 0.88 mA/cm^2, and the J_{SC} by Sample-HCSC-SQW is 0.75 mA/cm^2, which are on the same order of magnitude. The values of V_{OC} are very low for both samples, 0.56V given by Sample-HCSC-Barrier and 0.28V given by Sample-HCSC-SQW. The V_{OC} of Sample-HCSC-Barrier is two times of the V_{OC} of Sample-HCSC-SQW. The low values of the V_{OC} and the fill factor (FF) obtained for the SQW sample are certainly linked to the shunt resistance. And compared to the theoretical efficiency value for the InGaAs (0.74eV), which is around 22.5%, extracted from the Shockley-Queisser limits (see Fig. 3-28), the efficiency we measured for Sample-HCSC-Barrer and Sample-HCSC-SQW are both very low, while we didn't expect for high efficiency values because we added barriers in both structures.

	V_{OC} (V)	I_{SC} (mA)	J_{SC} (mA/cm^2)	FF	P_{max} (mW)	η	Surface area (cm^2)
Barrier	0.56	3.87x10^{-5}	0.88	53.07%	1.15x10^{-5}	0.27%	4.42x10^{-5}
SQW	0.28	3.30x10^{-5}	0.75	32.79%	3.03x10^{-6}	0.072%	4.42x10^{-5}

Table 4.2: Electrical characteristics of the diodes

The first effect of the SQW in the barrier seems to be the V_{OC} reduction. But the high shunt resistance certainly due to defects in the structure may also explain this V_{OC} low value. However, several diodes on the same wafer present a negative resistance effect around 0.3 V, linked to the selective contact. This SQW in the AlInAs barrier acts as a tunnel junction as shown in Fig. 4-24. The four chosen curves in Fig. 4-24 stand for four different diodes, which can be located as 2102A500, 2202A500, 2302A500 and 2502A500. We observe that V_{OC} is almost at the same value as the negative resistance effect in the dark (0.3 V). This negative resistance effect arises at a too low voltage to enable hot carrier selection. Some more studies are necessary to increase this voltage, as performed for GaAs/AlGaAs[6]. However, we decide to study deeply the samples available with photocurrent measurements.

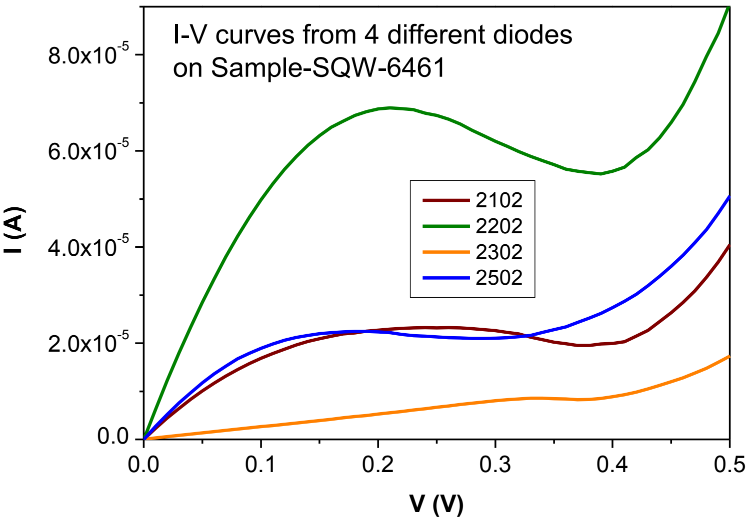

Fig. 4-24: I-V curves with negative resistances

4.4.3. Photocurrent results

To better understand the role of the SQW in the barrier, photocurrent measurements were performed, using laser excitation with two different wavelengths: 532 nm corresponds to 2.33 eV and 1064 nm corresponds to 1.16 eV at room temperature.

We first present the photocurrent results obtained with the Sample-HCSC-Barrier. Figure 4-25 present the I-V curves under laser excitation for different incident powers.

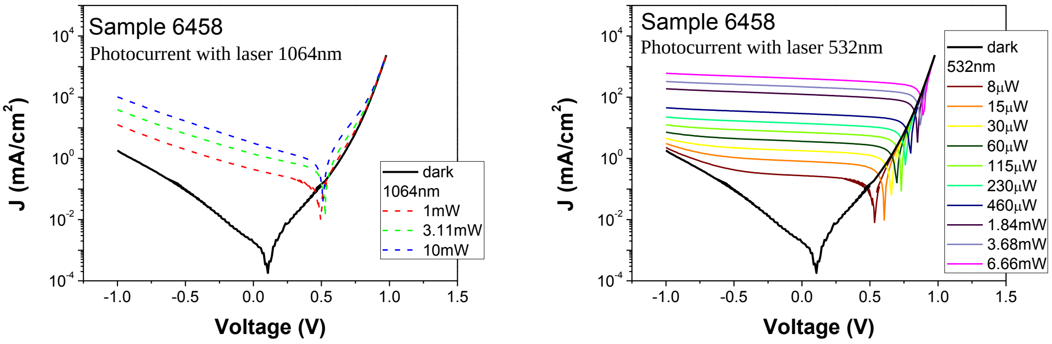

(a) (b)

Fig.4-25: Sample-HCSC-Barrier (6458) I-V characteristics measured under dark and two different laser illumination wavelengths with varying incident power (a): wavelength = 1064 nm; (b):wavelength = 532 nm.

To see more details in the area around V_{OC}, Fig.4-26 presents the linear curves.

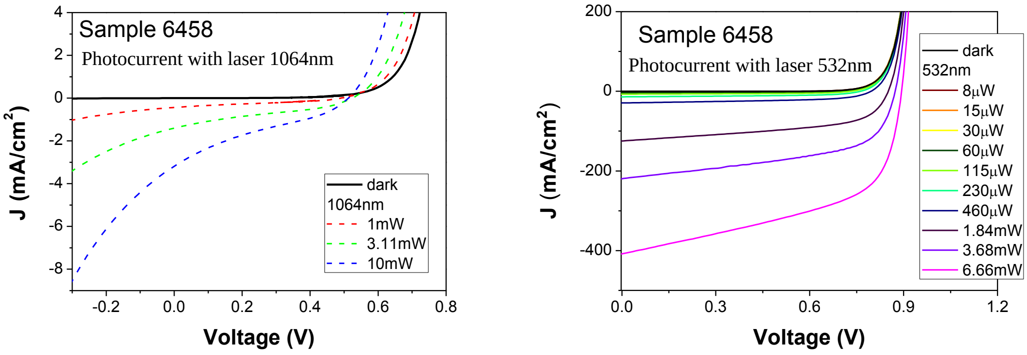

(a) (b)

Fig.4-26: Zoom in of I-V characteristics under laser illumination with varying incident power (a): wavelength = 1064 nm; (b): wavelength = 532 nm.

1064 nm wavelength is not absorbed by the active layer in InGaAs: a very low current is obtained even with a strong power: the short circuit current is almost multiplied by 100 with the 532 nm laser compared to the 1064 laser with an incoming power of 3 mW. The same experiment has been performed with the SQW sample. The opto-electrical characteristics are really different for the 1064 nm laser as shown in the following part.

Results of Sample-HCSC-SQW (6461)

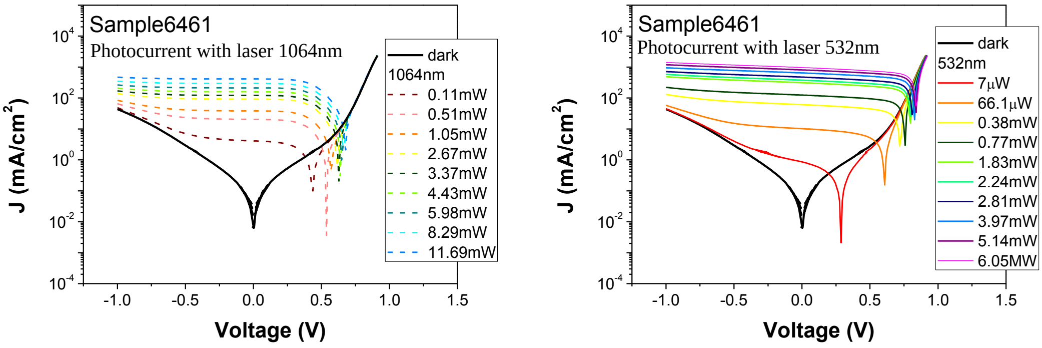

(a) (b)

Fig.4-27: Sample-HCSC-SQW (6461) I-V characteristics measured under dark and two different laser illumination wavelengths with varying incident power (a): wavelength = 1064 nm; (b):wavelength = 532 nm.

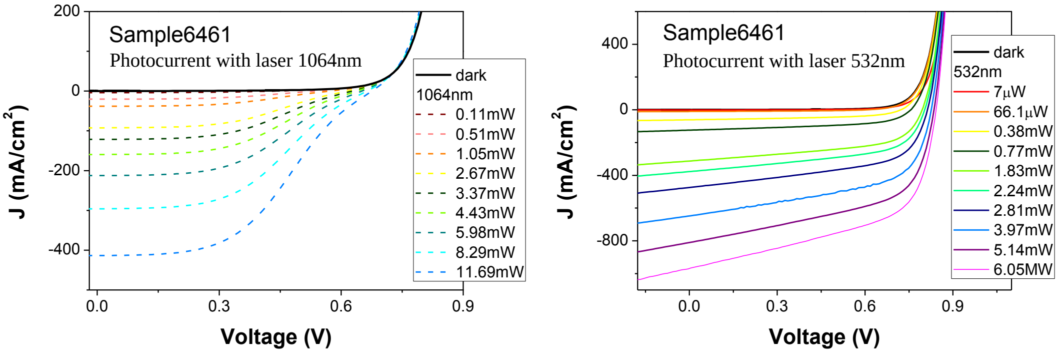

(a) (b)

Fig. 4-28: Zoom in of I-V characteristics under laser illumination with varying incident power (a): wavelength = 1064 nm; (b): wavelength = 532 nm.

At 1064 nm, the SQW sample exhibits good I-V characteristics: photocreated carriers in InGaAs can be extracted and contribute to photocurrent, contrary to the sample with the barriers. The curves of Fig. 4-28 (a) (under 1064 nm) show two different regimes with a transition around 0.3 V, while the right figure (b) shows classical I-V shape. The specific shape of the I-V curve with 1064 nm may be explained by the selective contact. For low tension, photo-created electrons can cross the barrier by tunnel effect if the confined level is adapted, while the increase of voltage limits this effect and reduces the current. A specific “s-shape” is therefore observed which limits the V_{OC} obtained with the 1064 nm laser.

Comparison between sample 6458 and 6461:

The following curves present the variations of the electrical characteristics as functions of incident laser power for each wavelength.

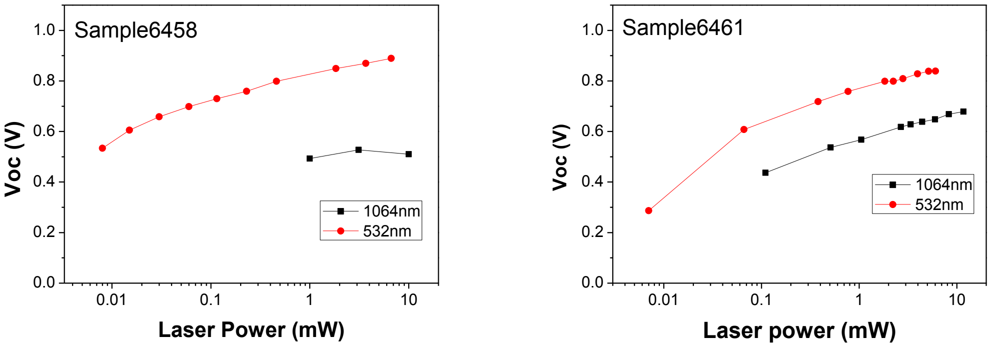

(a) (b)

Fig. 4-29: V_{OC} values as a function of laser power under different wavelengths: (a) Sample-Barrier-6458; (b) Sample-SQW-6461.

Fig. 4-29 shows that the V_{OC} increases as a logarithmic function of laser power for the 532 nm laser for both samples. For 1064 nm laser, this trend is only observed with the SQW sample while it remains almost constant for the barrier sample (with very low corresponding J_{SC}). This trend is also observed when measuring the V_{OC} variation of classical solar cells as a function of concentration [7]. In our case, with the J_{SC} equals to 0.88 mA/cm^2 for the Barrier sample under AM 1.5G which is 1 sun, we can get the concentration for J_{SC} (0.81 mA/cm^2) with 532 nm (laser power=0.015 mW) photoexcitation, which is 0.92 sun. Using the same relationship, a laser power of 1mW would correspond to a concentration of 61.3 suns. And same with the SQW sample, the J_{SC} equals to 0.75 mA/cm^2 for the Barrier sample under AM 1.5G which is 1 sun, we can get the concentration for J_{SC} (0.87 mA/cm^2) with 532 nm (laser power=0.007mW) photoexcitation, which is 1.16 sun, that is to say a laser power of 1mW is equivalent to 165.7 suns. For the SQW sample, V_{OC} is reduced for the 1064 nm laser compared to 532 nm laser but the two curves remain parallel.

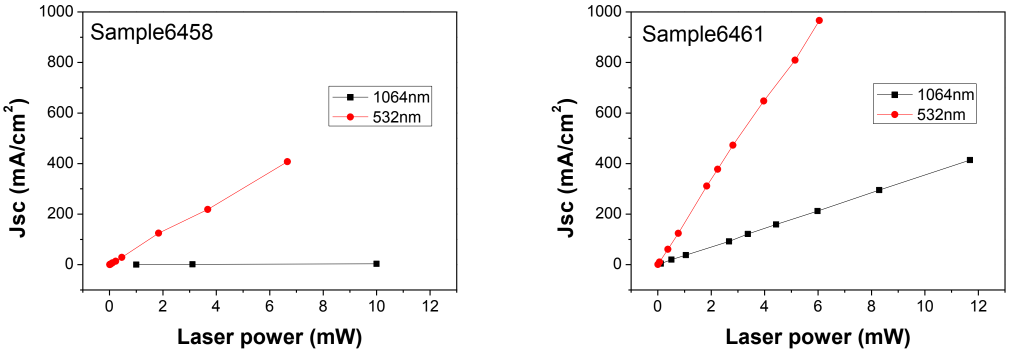

(a) (b)

Fig. 4-30: J_{SC} values as a function of laser power under different wavelengths: (a) Sample-Barrier-6458; (b) Sample-SQW-6461.

From the comparisons above (see Fig. 4-30), we can see the Sample-HCSC-SQW (6461) has better J_{SC} than the Sample-HCSC-Barrier (6458) for the 532 nm wavelength (6461 has the value of J_{SC} about two times of sample 6458), suggesting that there is more current went through the single quantum well. J_{SC} varies almost linearly as a function of laser power. This trend is the same as observed for solar cells under varying concentration [7].

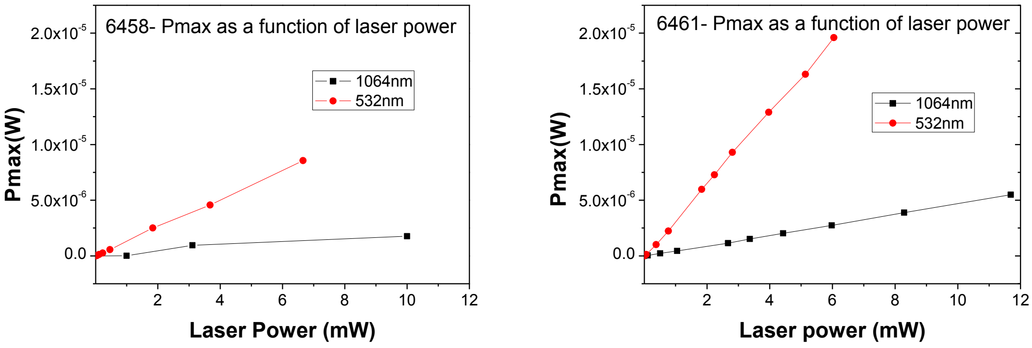

(a) (b)

Fig. 4-31: Maximum power values as a function of laser power under different wavelengths: (a) Sample-Barrier-6458; (b) Sample-SQW-6461.

Maximum electric power follows the same trend as J_{SC} for each set of measurement (see Fig. 4-31). To compare them, we extracted conversion efficiency from the slopes of these curves. To calculate the conversion efficiency, first we need the surface area of the ellipse which comes from the NA 0.22 fiber to produce the exciting light. Fig.4-32 shows the fiber and the tested diode. The ellipse has diameters of 400 µm by 200 µm, while the diode has a diameter of 75 µm. So we can get the ratio of the inserted light power over the output power from the fiber, which equals to the area of the diode divided by the area of the ellipse that is 7%.

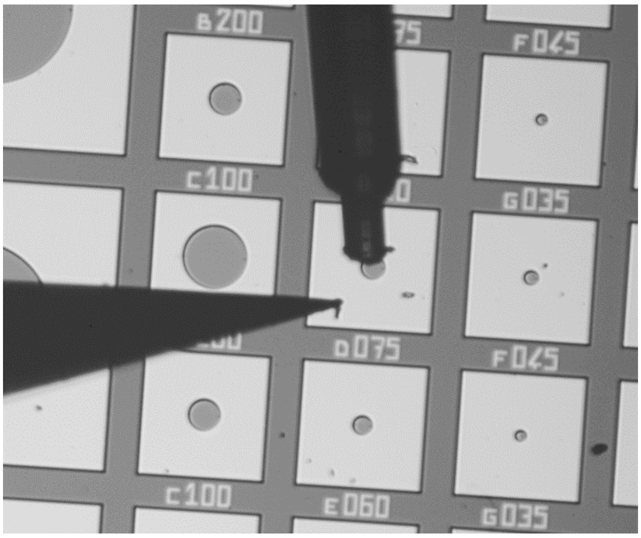

Fig. 4-32: Picture taken when measuring the photocurrent, giving a clear look of the fiber and the tested diode.

For the Sample-HCSC-Barrier 6458 under 1064 nm photoexcitation, we can get conversion efficiency by divide the slope of the linear curve (0.0013) by the ratio of the inserted light power over the output power (7%), which equals to 1.86%.

The 1064nm wavelength is not absorbed, or only by barrier layers and very low power is obtained while the 532nm creates electron-hole pairs in the device and the conversion efficiency is about 1.86%. This efficiency is calculated from the slope of the linear curve above which equals to 0.0013 (see Fig. 4-31 (a)) considering the percentage of the inserted light power over the output power from the fiber.

For the Sample-HCSC-SQW 6461 under 1064 nm photoexcitation, we can get conversion efficiency by divide the slope of the linear curve (0.0005) by the ratio of the inserted light power over the output power (7%), which equals to 0.71%. And under 532nm, the slope of the linear curve equals to 0.003, then we get the conversion efficiency value of 4.3%.

To understand the trends observed here, we performed SimWindows simulations taking into account laser excitation with the both wavelengths.

Results on Sample HSCS-Barrier-6458

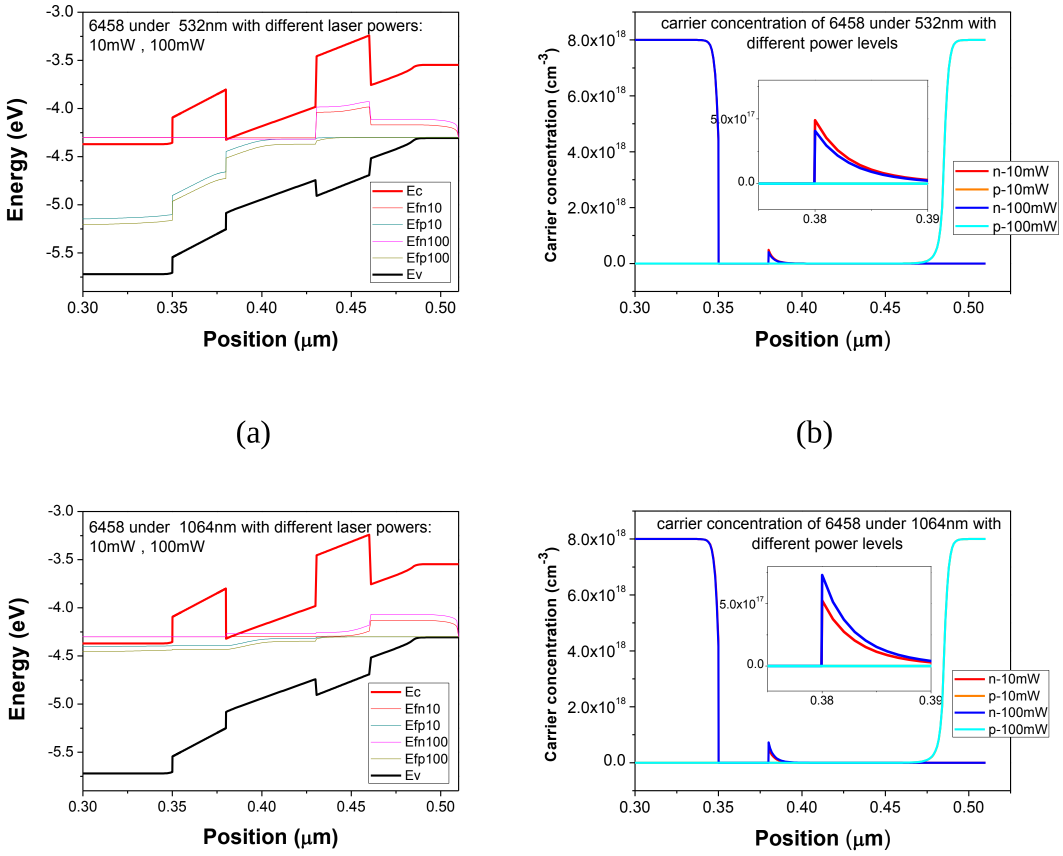

(a) (b)

(c) (d)

Fig. 4-33: Simulation of Sample-Barrier-6458 with two different laser wavelengths under different level of laser powers: (a) band diagram with 532nm; (b) carrier concentration with 532nm; (c) band diagram with 1064nm; (d) carrier concentration with 1064nm.

Fig. 4-33 (b) shows that the carrier concentration is almost as a function of laser power for the 532 nm wavelength. For a laser power of 10mW, the n-type concentration reaches almost 5.10^{17} cm^{-3}, almost the same value as observed on Fig. 4-7 with AM1.5G excitation. When the laser power increases, the carrier concentration decreases, showing th carriers are easily extracted: the increase of mean carrier energy with laser power helps the carrier extraction to overcome the barrier. Conversely, for the 1064 nm laser (Fig. 4-33 (d)), one can observe that the carrier concentration in the InGaAs absorption layer increases with the laser power, reaching 7.10^{17} cm^{-3}. The AlInAs barrier clearly blocks electrons. Only electrons with high enough energy can cross the barrier, explaining the poor electrical characteristics obtained with this sample at 1064 nm wavelength.

Results on Sample HSCS-SQW-6461

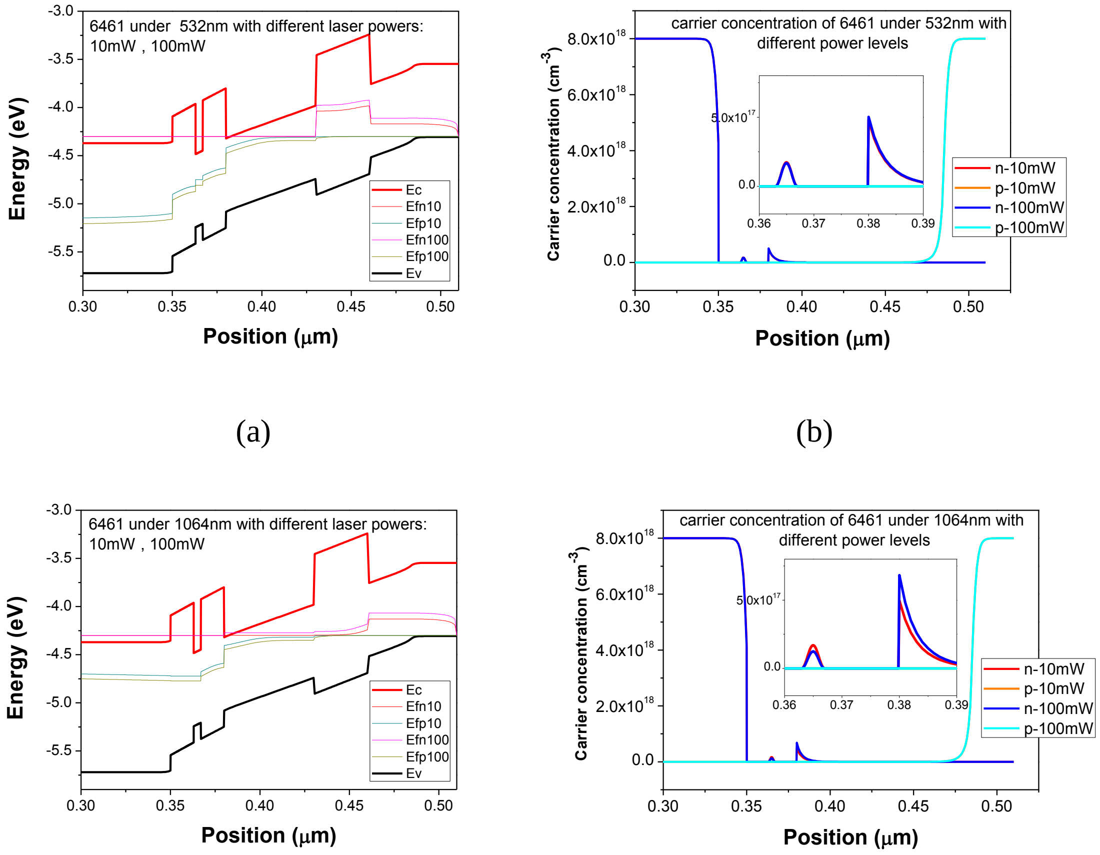

(a)

(b)

(c)

(d)

Fig. 4-34: Simulation of Sample-Barrier-6461 with two different laser wavelengths under different level of laser powers. (a) band diagram with 532nm; (b) carrier concentration with 532nm; (c) band diagram with 1064nm; (d) carrier concentration with 1064nm.

Fig. 4-34 (b) shows the carrier concentration for a 532 nm wavelength laser. It presents the same shape as Fig. 4-9 under AM1.5G solar spectrum with 10 mW or 100mW: almost 2.10^{17} cm^{-3} in the well and maximum 5.10^{17} cm^{-3} in the absorber layer. Contrary to the barrier sample, the carrier concentration does not depend on the laser power: more carriers are photogenerated with a higher laser power but they are well extracted and contributed to the photocurrent. For 10 mW laser power, the mean carrier energy is certainly smaller but carriers are also extracted by the SQW confined level. Figure 4-34 (d) shows the carrier concentration for a 1064 nm wavelength laser. For a high laser power, the electron concentration increases in the absorber layer while decreases in the SQW. The average electronic energy is certainly higher and does not correspond anymore to the confined electronic level in the well, reducing the carrier extraction efficiency. Tunnelling seems to be more efficient for a low laser power.

These simulations help to explain the photocurrent results: tunnelling fully explains the better electrical characteristics of the SQW sample with the 1064 nm laser. The high laser power regime simulated has not been reached experimentally so the decrease of tunnelling with the laser power was not observed.

4.5. Conclusion

In this chapter, a set of HCSC with two different contacts (a semi-selective barrier and a selective single quantum well) are presented to study the extraction of hot carriers from the two contacts. Basic simulations using SimWindows gives the band diagrams of all structures both in the dark and under illumination. It helped to determine the p-cover (InGaAs), absorber thickness (50 nm InGaAs) and the doping levels (no doping for the AlInAs barrier). Samples have been grown through MBE, structural characteristics have been studied. The main diffraction peaks coming from InGaAs and AlInAs layers are very close to the InP (004) substrate diffraction peak, suggesting the heterostructure is almost lattice-matched. And with the opto-electrical results for both samples, we demonstrated the effect of selective and semi-selective contacts on solar cells characteristics. The bad shunt resistance prevented us to reach higher V_{OC} for the SQW sample and to obtain hot carrier signature. However, the photocurrent results obtained with different lasers showed a strong effect of the SQW, showing higher efficiency for both wavelengths. A next step is to adapt the confined level to hot carriers to allow higher V_{OC}.

References:

[1] S. K. Shrestha, P. Aliberti, and G. J. Conibeer, “Energy selective contacts for hot carrier solar cells,” *Sol. Energy Mater. Sol. Cells*, vol. 94, no. 9, pp. 1546–1550, Sep. 2010, doi: 10.1016/j.solmat.2009.11.029.

[2] Y. Feng *et al.*, “Non-ideal energy selective contacts and their effect on the performance of a hot carrier solar cell with an indium nitride absorber,” *Appl. Phys. Lett.*, vol. 100, no. 5, p. 053502, Jan. 2012, doi: 10.1063/1.3680594.

[3] Y. F. Conibeer G, Guillemoles J F, *Advanced Concepts in Photovoltaics. Cambridge: Royal Society of Chemistry*. 2014.

[4] I. Vurgaftman, J. R. Meyer, and L. R. Ram-Mohan, “Band parameters for III–V compound semiconductors and their alloys,” *J. Appl. Phys.*, vol. 89, no. 11, pp. 5815–5875, Jun. 2001, doi: 10.1063/1.1368156.

[5] N. Cavassilas *et al.*, “Theoretical Demonstration of Hot-Carrier Operation in an Ultrathin Solar Cell,” *Phys. Rev. Appl.*, vol. 17, no. 6, p. 064001, Jun. 2022, doi: 10.1103/PhysRevApplied.17.064001.

[6] A. Julian, Z. Jehl, N. Miyashita, Y. Okada, and J.-F. Guillemoles, “Insights on energy selective contacts for thermal energy harvesting using double resonant tunneling contacts and numerical modeling,” *Superlattices Microstruct.*, vol. 100, pp. 749–756, Dec. 2016, doi: 10.1016/j.spmi.2016.10.023.

[7] P. Singh and N. M. Ravindra, “Temperature dependence of solar cell performance—an analysis,” *Sol. Energy Mater. Sol. Cells*, vol. 101, pp. 36–45, Jun. 2012, doi: 10.1016/j.solmat.2012.02.019.

General conclusions and future works

This thesis focuses on two kinds of advanced solar cells aiming to surpass the theoretical efficiency set by Shockley-Queisser limit: tandem cells and hot carrier solar cells based on III-V materials.

Concerning the tandem cells, a GaP n-i-p photodiode grown on silicon substrate has been studied. It could serve as a top cell in the tandem cell structure onto silicon substrate. Two different electrical contacts have been investigated to identify the effects of the GaP/Si interface: top-top and top-bottom contacts. For top-top and top-bottom electrical contacts, we obtain efficiencies equal to 1.48% and 0.77% respectively, which reach around 10% of the theoretical efficiency value set by Shockley-Queisser limits. This experimental study shows that the EQE is slightly different between the diode with full GaP contacts (named top-top) and the diode with a rear face contact on silicon (named top-bottom). The GaP/Si interface does not deteriorate the solar cell properties, so the GaP/Si platform is a good candidate to grow III-V solar cells onto Si. And for the first attempt of the GaAsPN/Si tandem cell, we have both the EQE and I-V results of this sample. The efficiency for this cell reaches only 1.96% which is likely due to the huge amount of structural defects of the GaAsPN top cell, leading to an electrical shunt of this subcell. Therefore, an improvement of the MBE growth process would be necessary for the development of such tandem cells.

The prospects of this work are to go on developing different types of tandem cells on this GaP/silicon platform like the GaAsPN/Si solar cell. The GaP/Si interface can be improved, for example with doping the GaP layer at the GaP/Si interface. In the case of the mastering of threading antiphase boundaries leading to a large conductivity in GaP (which can be seen as a “semimetal”), we maybe use their properties to drive the carriers from the pin top solar cell to the all-Si tunnel junction at the GaP/Si interface. Moreover, the study we have done in this thesis will also be useful to grow different materials like perovskites or CIGS as top-junction in tandem cells on silicon, through a GaP intermediate layer.

Concerning hot carrier solar cells, a set of InGaAs/InP solar cells with two different contacts (a semi-selective barrier and a selective single quantum well) are presented to study the extraction of carriers from the two contacts. Basic simulations using SimWindows gives the band diagrams of all structures both in the dark and under illumination. It helped to determine the p-cover (InGaAs), absorber thickness (50 nm InGaAs) and the doping levels (no doping for the AlInAs barrier). Samples have been grown through MBE, structural characteristics have been studied. With the opto-electrical results for both samples, we demonstrated the effect of selective and semi-selective contacts on solar cells characteristics. The bad shunt resistance prevented us to reach higher V_{OC} for the SQW sample. However, the photocurrent results obtained with different lasers showed a strong effect of the SQW, showing higher efficiency for both wavelengths. A next step is to adapt the confined level to hot carriers to allow higher V_{OC}. The first prospects of this work are those presented in the ICEMAN project: try to detect hot carriers in InGaAs/InP by using an calibrated hyperspectral PL set-up, in concentration condition (at IPVF) and adding a dielectric mirror in order to enhance the light absorption (at C2N). Moreover, we are developing the same heterostructures with a quaternary InGaAsP as the absorber. This will facilitate the analyses in a hot carrier regime.

Résumé

Cette thèse présente une contribution au développement de deux types de cellules solaires de troisième génération. L’objectif principal de cette recherche est de produire des cellules solaires plus efficaces et à moindre coût. Contrairement aux cellules couteuses de la première génération ou aux matériaux polluants et limités utilisés dans la seconde génération, la troisième génération de cellules solaires comprend les technologies les plus avancées et prometteuses de nos jours.

La première cellule solaire étudiée dans cette thèse est une cellule III-V GaP sur Silicium.

De nos jours, les meilleurs rendements ont été obtenu avec des cellules solaires multijonctions composées d’un empilement de semi-conducteurs III-V monojonction sur des substrats de GaAs ou Ge. Malgré leur fort rendement, ces cellules présentent un coût très élevé du fait des substrats utilisés. C’est pourquoi, l’une des stratégies est de développer une cellule tandem sur silicium pour bénéficier à la fois du bas coût du substrat et de la maturité de la technologie silicium, tout en obtenant des rendements supérieurs à ceux d’une cellule silicium seule. En effet, des études théoriques ont montré qu’une cellule tandem comportant une couche à large bande interdite (idéalement 1.7eV) sur une couche de silicium de band interdite à 1.1eV pourrait atteindre un rendement de 37%[1]. C’est pourquoi, on utilise les composés à base de GaP, par épitaxie par jets molécylaires (EJM), dont la maille est en quasi accord de paramètre cristallin sur le silicium et qui possède un gap élevé (2.2eV).

Dans un premier temps, on étudie une photodiode GaP n-i-p épitaxiée par EJM sur un substrat de Si (001). Une couche de 20nm de GaAsP p++ permet d’obtenir des contacts ohmiques sur la couche de GaP de type p en utilisant du Ti/Pt/Au. Deux configurations de contacts électriques ont été étudiées : une configuration top-top dans laquelle le courant ne traverse pas l’interface GaP/Si et une configuration top-bottom dans laquelle le courant la traverse. Pour cela, deux types de contacts ont été utilisés : un contact de surface sur le GaP type n en Ni-Au-Ge et un contact arrière sur le Silicium. Dans la configuration top-bottom, une implantation ionique de Phosphore a été réalisée pour doper le substrat de Silicium en type n après la croissance MBE et des contact Aluminium ont été utilisés. La figure 1 montre la structure de la diode.

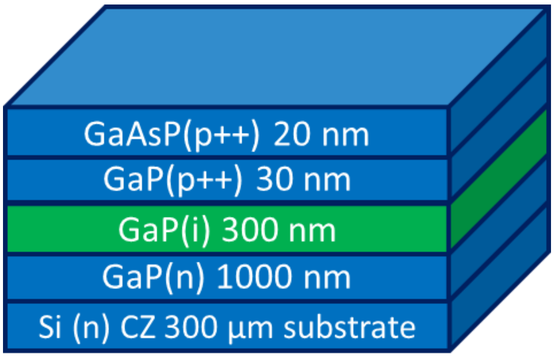

Fig 1 : Structure de la cellule solaire III-V GaP sur Silicium, avant la fabrication des contacts métalliques.

L'optimisation de la croissance de la couche de GaP sur Silicium et des analyses de l'épitaxie GaP ont été réalisées durant la thèse de Yanping Wang[2] et Ang Zhou[3]. Dans la figure 2, une coupe TEM montre la quasi absence de défauts type micro-macles et de domaines d'anti-phase, qui s'annihilent à l'interface GaP/Silicium.

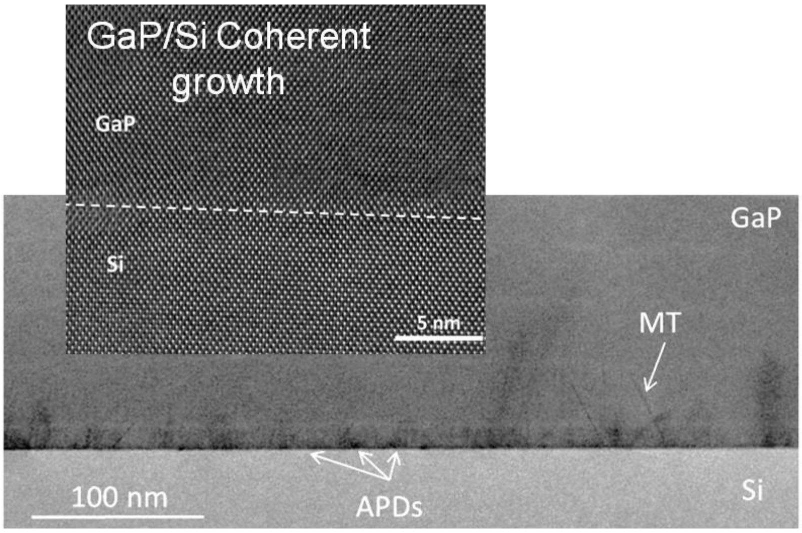

Fig 2 : Coupe TEM typique montrant l'absence de défauts à l'interface GaP/Silicium.

Nous avons ensuite étudié les diodes présentant les deux types de contacts (top-top et top-bottom). Leurs configurations optiques diffèrent (Figure 3).

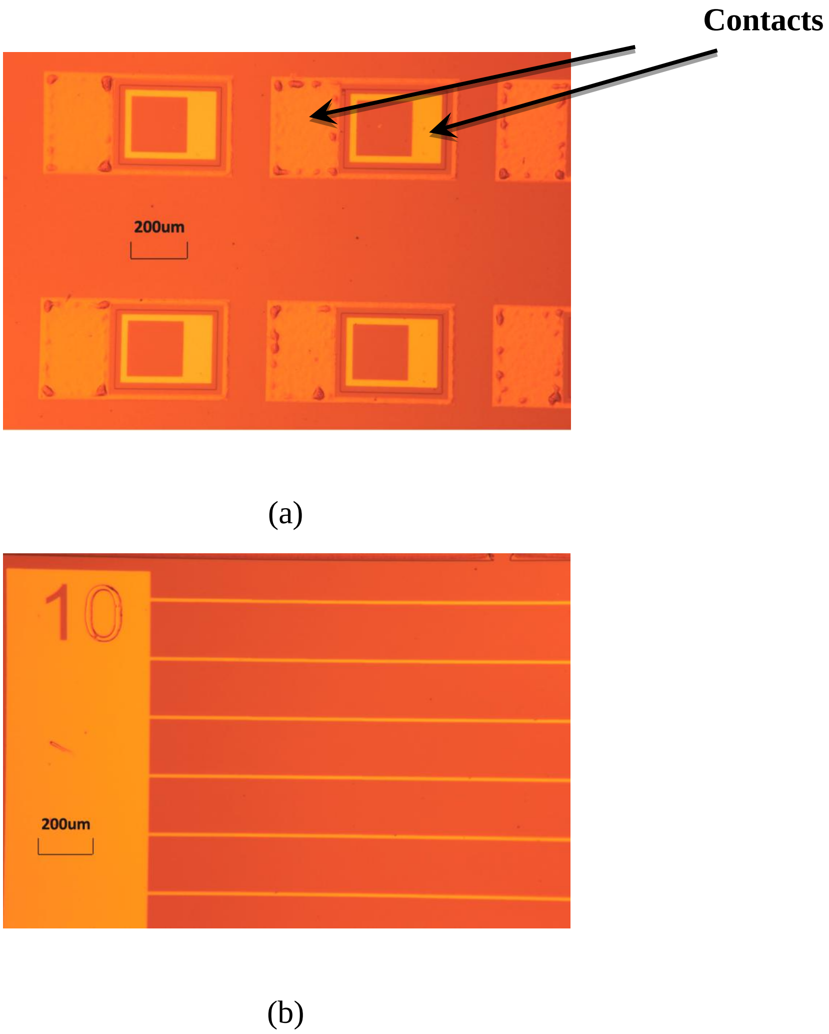

Fig 3 : Photo de : (a) contacts face avant dans le cas top-top d'une cellule GaP et (b) contacts face avant dans le cas top-bottom d'une cellule GaP.

Pour étudier les propriétés électro-optiques des cellules solaires GaP, des mesures de rendement quantique externe (EQE) ont été réalisées. La figure 4 présente une comparaison des mesures EQE sur les deux configurations. L'absorption commence à 2.25eV (bandgap indirect) et augmente à 2.8eV, ce qui correspond au bandgap du GaP. L'utilisation de contacts top-bottom montre un EQE légèrement plus faible qu'avec des contacts top-top. Ceci est probablement dû à une longueur de diffusion plus faible des porteurs sur fait de l'interface GaP/Si. La valeur d'EQE de la configuration top-bottom à 3.3eV (réponse bleue) est la même que dans la configuration top-top. Dans l'EQE à 3.3eV (réponse rouge), la réponse est plus faible pour la configuration top-bottom (40% contre 55% pour la configuration top-top). Comme l'EQE à basse énergie (grandes longueurs d'onde) est plus sensible à l'absorption à plus grande épaisseur, cela pourrait indiquer que l'extraction des porteurs est plus difficile sous l'absorbeur de GaP dans la configuration top-bottom, c'est-à-dire quand les porteurs traversent l'empilement constitué de la couche de GaP type n puis intrinsèque de 1µm d'épaisseur, et l'interface GaP/Si. Cependant, le résultat de l'EQE de la configuration top-bottom et encourageante pour le développement de cellules tandem GaP/Si.

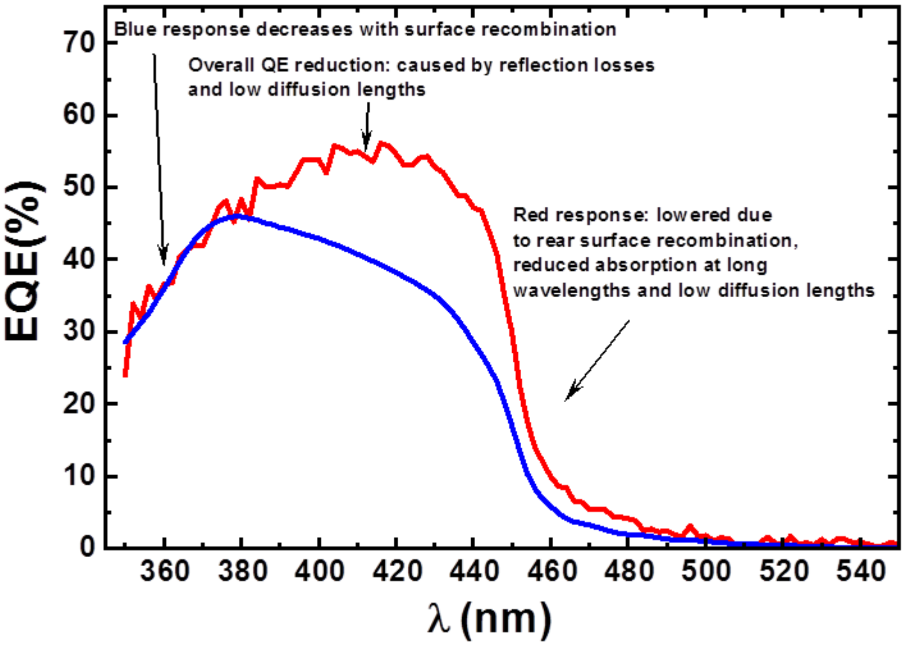

Fig 4 : Comparaison entre les réponses EQE de la configuration top-top (rouge) et la configuration top-bottom (bleu).

Les mesures I-V sous obscurité et sous éclairement des deux configurations ont été réalisées. La figure 5 présente les courbes obtenues en échelle logarithmique.

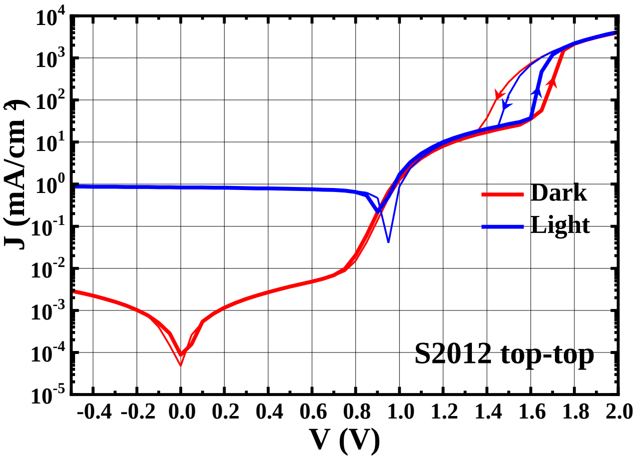

(a)

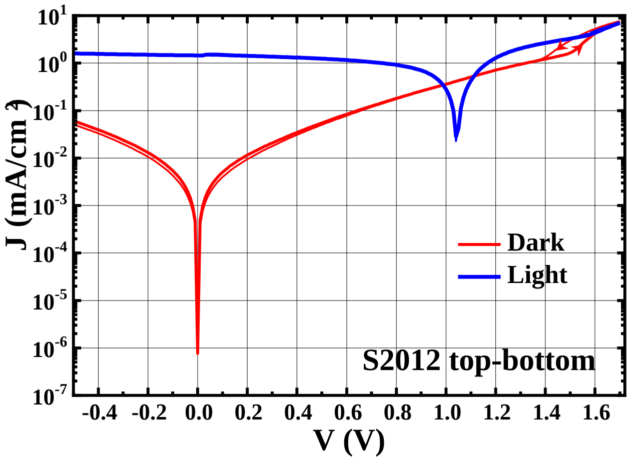

(b)

Fig. 5: Courbes L-I-V et D-I-V en échelle logarithmique : (a) en configuration top-top ; (b) en configuration top-bottom.

La comparaison des résultats des mesures électriques entre la configuration top-top et top-bottom sont résumés dans le tableau 1. Les différentes mesures semblent indiquer que le passage à travers l'interface GaP/Si dégrade probablement légèrement les caractéristiques des cellules solaires, notamment sur le facteur de remplissage (dégradation des résistances séries et parallèles). En effet, les échantillons avec des contacts top-top ont un facteur de remplissage de 0.68, plus élevé que pour les échantillons à contacts top-bottom dont le facteur de remplissage est de 0.48. Une explication est que les contacts top-top ont une résistance série plus faible comme indiqué par la caractéristique I-V sous éclairement. La résistance série plus élevée est probablement due à des défauts structurels à l'interface GaP/Si et peuvent expliquer la valeur d'EQE plus faible à grandes longueurs d'onde.

Cependant, les résultats obtenus dans la configuration top-bottom sont suffisants pour envisager le développement de cellules tandem III-V/Si.

	V_{OC} (V)	J_{SC} (mA/cm^2)	V_{max} (V)	J_{max} (mA/cm^2)	FF	η	$\eta_{theoretical}$
Top Top	0.95	0.837	0.80	0.680	0.68	0.54%	8%
Top Bottom	1.043	1.493	0.74	1.004	0.48	0.77%	8%

	D-I-V R_s (Ω.cm^2)	L-I-V R_s (Ω.cm^2)	D-I-V R_{sh} (Ω.cm^2)	L-I-V R_{sh} (Ω.cm^2)
Top Top	53	34	$1.8\text{x}10^5$	$1.1\text{x}10^4$
Top Bottom	308	120	$1.0\text{x}10^4$	$3.33\text{x}10^3$

Tableau 1 : Comparaison des mesures électriques entre les contacts top-top et top-bottom sur des cellules solaires GaP.

La deuxième type de cellules solaires étudiées dans cette thèse consiste en une cellule à porteurs chauds. Il s’agit de concevoir et d’élaborer une hétérostructure III-V sur substrat InP pour le développement de cellules solaires à porteurs chauds (Hot Carriers Solar Cell ou HCSC) à contacts sélectifs ou semi-sélectifs efficaces.
Les cellules solaires à porteurs chauds font également partie de la troisième génération de cellules solaires, ce qui donne l’opportunité de récolter plus d’énergie solaire que la limite donnée par le modèle de Shockley-Queisser (33%)[4]. Contrairement aux cellules photovoltaïques classiques, les cellules solaires à porteurs chauds convertissent l’énergie cinétique excédentaire en puissance électrique utile et ne la dissipent pas par des mécanismes de thermalisation. Pour extraire les porteurs lorsqu’ils sont encore « chauds », il faut développer des contacts électriques très sélectifs. Dans cette thèse, nous avons étudié une série de HCSC avec différents contacts (une barrière semi-sélective et un puits quantique unique sélectif) afin de comparer l’extraction des porteurs chauds au travers ces deux types de contacts sélectifs. Les échantillons ont été fabriqués sur des substrats InP (001). Les contacts semi-sélectifs sont en AlInAs tandis que les puits quantiques uniques (Single Quantum Well ou SQW) pour les contacts sélectifs sont composés d’une hétérostructure en AlInAs-InGaAs-AlInAs. Les structures des deux échantillons sont illustrées ci-dessous dans la figure 6 et la figure 7. Les deux échantillons sont des diodes PIN épitaxiés à l’aide d’une MBE à source gazeuse RIBER32 en utilisant du Si pour le dopage de type n et du Be pour le dopage de type p, et en accord de paramètre cristallin sur le substrat d’InP (001).

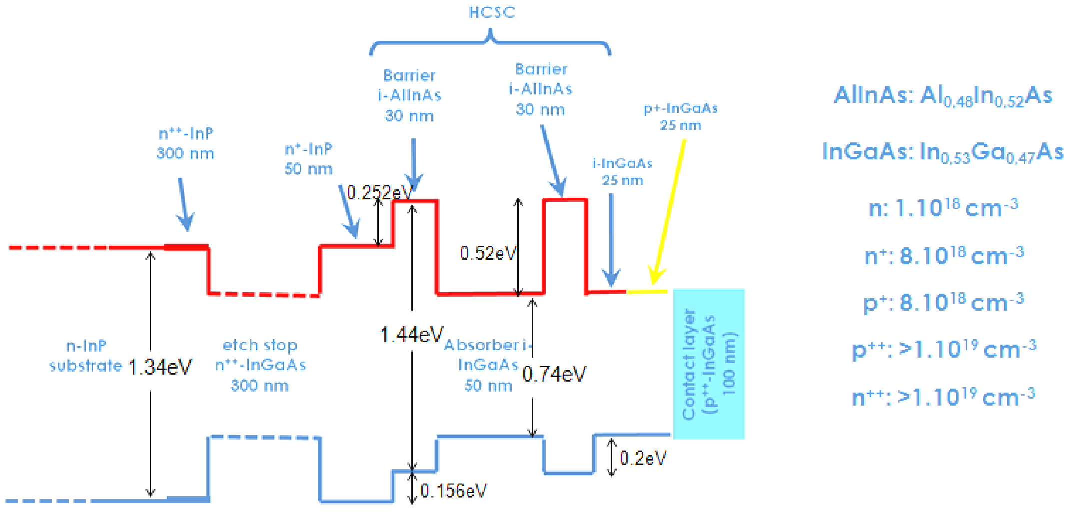

Fig. 6 : Alignement des bandes de l'échantillon HCSC-Barrier, avec une barrière AlInAs de 30 nm d'épaisseur comme contact semi-sélectif du côté n.

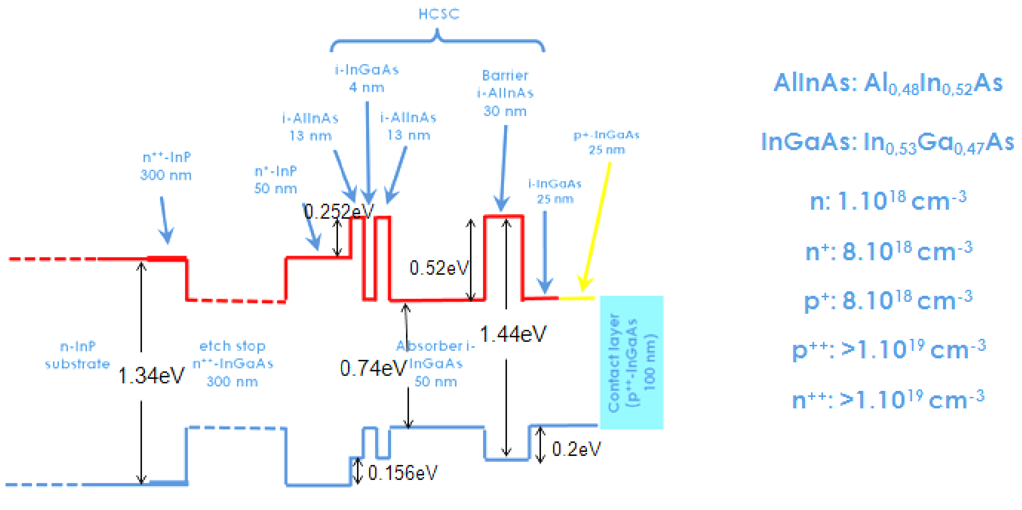

Fig. 7 : Alignement des bandes de l'échantillon HCSC-SQW, avec un puits quantique unique AlInAs-InGaAs-AlInAs de 13 nm-4 nm-13 nm et le contact sélectif de type N.

Cette étude est un premier pas vers le développement de cellules HCSC. Tout d'abord, on a réalisé des simulations sur les deux types de contacts sélectifs pour obtenir leur diagramme de bande sous obscurité et sous éclairement à AM1.5G (Figure. 8).

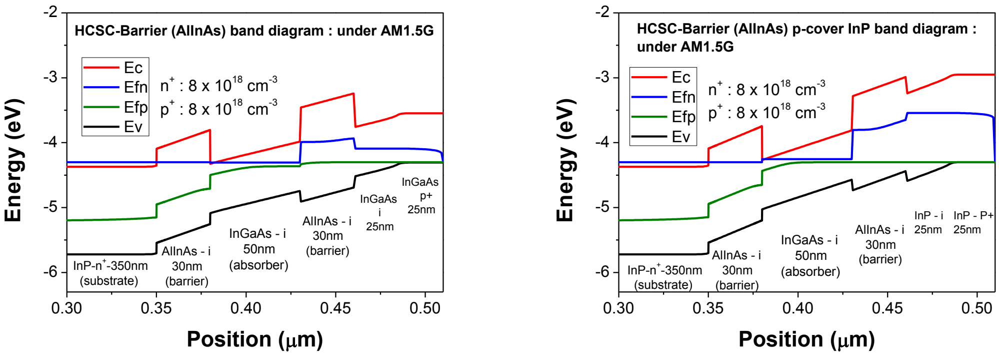

(a) (b)

Fig. 8 : Diagramme de bande électronique de la structure HCSC simplifiée avec une (a) Barrière / (b) SQW sous éclairage AM 1.5G à l'équilibre, sans contact.

Ensuite, nous avons étudié les deux structures épitaxiées. En particulier, la diffraction aux rayons X a mis en évidence la bonne concordance de paramètre cristallin entre la barrière AlInAs sur le substrat InP. La figure 9 montre la comparaison des résultats de diffraction des rayons X entre l'échantillon HCSC-Barrier et l'échantillon HCSC-SQW.

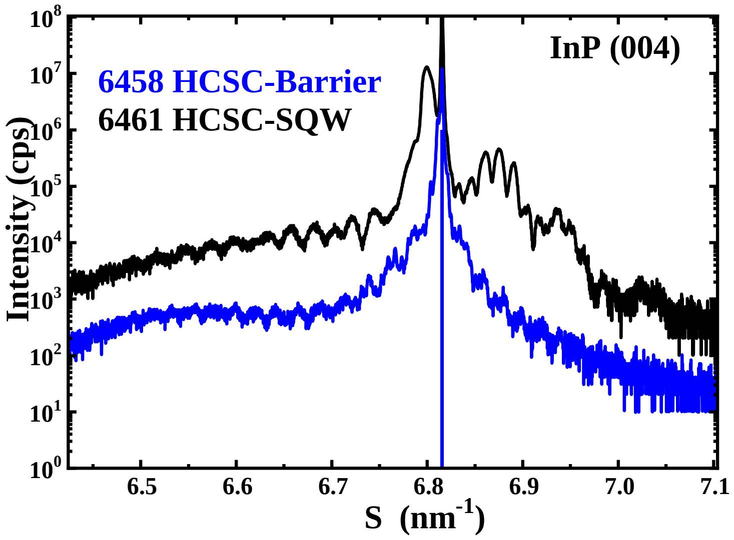

Fig. 9 : Comparaison des résultats de diffraction des rayons X entre l'échantillon HCSC-Barrier et l'échantillon HCSC-SQW.

Pour les deux échantillons, les principaux pics de diffraction provenant des couches InGaAs et AlInAs sont très proches du pic de diffraction du substrat InP (004) (la ligne bleue sur la figure), ce qui signifie que l'hétérostructure est presque adaptée au réseau comme prévu.

Enfin, nous avons réalisé les étapes technologiques pour fabriquer des cellules HCSC. Les résultats de ces travaux sur la conception et l'élaboration des HCSC sont présentés dans ce manuscrit. Afin d'explorer les effets des puits quantiques de InGaAs sur les propriétés électro-optiques des photodiodes ; des mesures électro-optiques ont été réalisées sur deux diodes circulaires de 75 µm de diamètre. Les caractéristiques électriques obtenues sous simulateur solaire sont présentées dans la figure 10 et le Tableau 2.

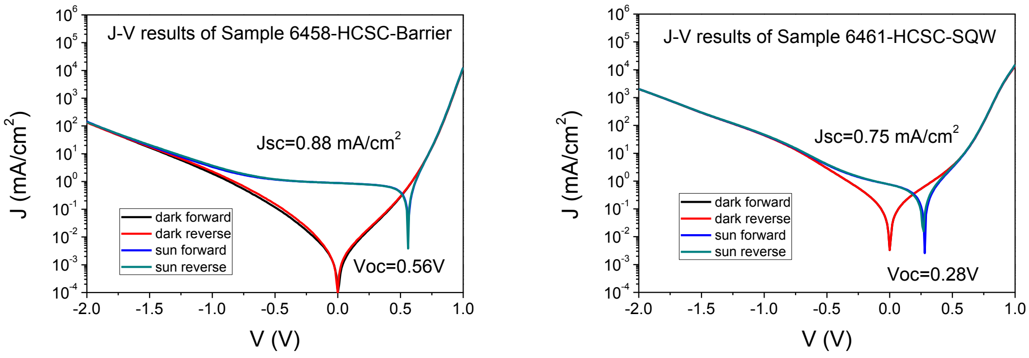

(a) (b)

Fig 10 : Caractéristiques I-V sous spectre solaire (AM1.5G). Tension en échelle logarithmique. (a) Echantillon HCSC avec barrière ; (b) Echantillon HCSC avec SQW

	V_{OC} (V)	I_{SC} (mA)	J_{SC} (mA/cm^2)	FF	P_{max} (mW)	η	Surface area (cm^2)
Barrier	0.56	3.87x10^{-5}	0.88	53.07%	1.15x10^{-5}	0.27%	4.42x10^{-5}
SQW	0.28	3.30x10^{-5}	0.75	32.79%	3.03x10^{-6}	0.072%	4.42x10^{-5}

Tableau 2 : Caractéristiques électriques des diodes

Enfin, pour mieux comprendre le rôle des SQW dans la barrière, des mesures de photo-courant ont été réalisées en utilisant une excitation laser à deux longueurs d'onde : 532nm correspondant à une énergie de 2.33eV et 1064nm correspondant à une énergie de 1.16eV à température ambiante. Les résultats sont présentés dans les figures 11 et 12.

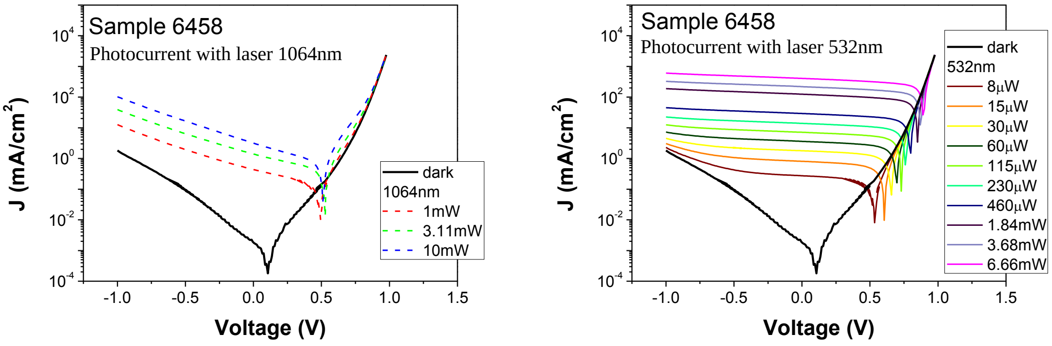

(a) (b)

Fig 11 : Echantillon HCSC avec barrière (6458) : caractéristiques I-V sous obscurité et sous excitation laser à deux longueurs d'onde pour différentes puissances incidentes : (a) longueurs d'onde = 1064 nm; (b): longueurs d'onde = 532 nm.

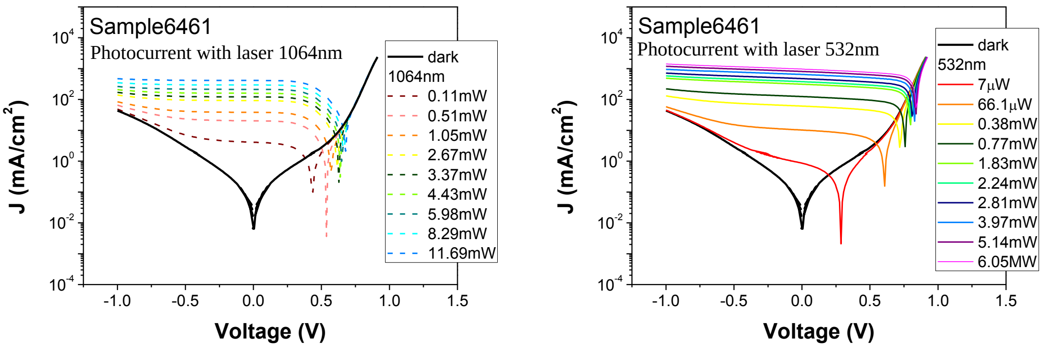

(a) (b)

Fig 12 : Echantillon HCSC avec SQW (6461) ; caractéristiques I-V sous obscurité et sous excitation laser à deux longueurs d'onde pour différentes puissances incidentes.

Le détail de ces analyses est présenté dans le manuscrit au chapitre 4.

A l'aide des des analyses opto-électriques précédentes, nous avons démontré l'effet des contacts sélectifs et semi-sélectifs sur les caractéristiques des cellules solaires. Une résistance shunt trop basse a limité la tension de sortie V_{OC} pour l'échantillon avec SQW et a rendu difficile l'obtention de la signature d'une cellule à porteurs chauds. Néanmoins, les photo-courants obtenus ont montré que le SQW augmentait le rendement sous différentes puissances laser pour les deux longueurs d'onde testées. Une amélioration possible serait d'adapter le niveau de confinement des porteurs chauds afin d'augmenter le V_{OC}.

References :

[1] S. Almosni *et al.*, "Correlations between electrical and optical properties in lattice-matched GaAsPN/GaP solar cells," *Sol. Energy Mater. Sol. Cells*, vol. 147, pp. 53–60, Apr. 2016, doi: 10.1016/j.solmat.2015.11.036.

[2] Y. Wang, "Structural analyses by advanced X-ray scattering on GaP layer epitaxially grown on silicon for integrated photonic applications," Ph.D., INSA Rennes, 2016.

[3] A. Zhou, "Structural analysis of GaP/Si platform and CIGS/GaP/Si heterostructures for photovoltaic applications," Ph.D., INSA Rennes, 2019.

[4] R. T. Ross and A. J. Nozik, "Efficiency of hot ‐ carrier solar energy converters," *J. Appl. Phys.*, vol. 53, no. 5, pp. 3813–3818, May 1982, doi: 10.1063/1.331124.

Titre : Développement de cellules solaires avancées - Contribution aux cellules à porteurs chauds sur InP et aux cellules tandem monolithiques III-V sur Si

Mots clés : : GaP / Si, MBE, Cellules solaires à porteurs chauds, hétérostructures III-V / InP, cellules solaires tandem sur Si, technologies des matériaux III-V

Résumé : Cette thèse concerne la réalisation de deux types de cellules solaires innovantes et à haut rendement, les cellules tandem III-V/Si et les cellules à porteurs chauds (HCSC). Les cellules HCSC offrent la possibilité de récolter plus d'énergie solaire que la limite fixée par le modèle de Shockley-Queisser. Dans les HCSC, l'énergie cinétique excédentaire est convertie en énergie électrique utile plutôt que d'être perdue par des mécanismes de thermalisation. Pour extraire les porteurs pendant qu'ils sont encore "chauds", il faut développer des contacts sélectifs (en énergie) efficaces. Dans ce travail, nous étudions un ensemble de cellules HCSC avec deux contacts sélectifs différents (une barrière semi-sélective et un puits quantique unique sélectif) pour étudier l'extraction des porteurs chauds. Les échantillons ont été fabriqués sur substrat d'InP (001) par MBE. Cette étude est la première étape vers le développement de cellules HCSC.

Aujourd'hui, les meilleurs rendements sont atteints grâce à des cellules solaires multijonctions sur des substrats en GaAs ou en Ge. Bien que présentant des rendements de conversion élevés, ces cellules solaires souffrent du coût élevé de ces substrats. Notre stratégie consiste donc à développer une cellule tandem sur silicium. De plus, cette voie permettrait de dépasser la limite d'efficacité théorique des cellules individuelles en silicium. Dans ce but, nous utilisons le GaP, épitaxié par MBE sur Si, comme première étape vers l'utilisation d'absorbeurs en nitrures dilués GaAsPN possédant la bande interdite requise de 1,7 eV. En particulier, nous avons étudié des photodiodes GaP n-i-p épitaxiées sur substrat de Si, et avec deux types de contacts électriques : des contacts top-top (non sensible à l'interface GaP/Si) et des contacts top-bottom (photocourant à travers l'interface GaP/Si).

Title : Development of advanced solar cells - Contribution to the HCSC on InP and to the III-V onto Si monolithic tandem cells

Keywords : GaP / Si, MBE, hot carrier solar cells, III-V / InP heterostructures, tandem solar cells on Si, III-V materials technologies

Abstract : This thesis subject concerns the realization of two types of innovative and high efficiency photovoltaic solar cells, the III-V/Si tandem cells and the hot carrier cells (HCSC). HCSC offer the possibility to harvest more solar energy than the limit set by the Shockley-Queisser model. In the HCSC the excess kinetic energy is converted into useful electric power rather than being lost through thermalization mechanisms. To extract the carriers while they are still "hot", one needs to develop energy selective contacts. In this work, we investigate a set of HCSC with two different contacts (a semi-selective barrier and a selective single quantum well) to study the extraction of the hot carriers from these contacts. The samples were made on InP (001) substrate by MBE. We present our work in the whole picture of design and elaboration of HCSC.

Nowadays, the best efficiencies are reached thanks to multijunction solar cells on GaAs or Ge substrates. While displaying high conversion efficiencies, these solar cells suffer from the high cost of such substrates. Therefore, our strategy is to develop a tandem cell on silicon. Furthermore, this route would surpass the theoretical efficiency limit of the Si single cells. To this aim, we use GaP epitaxially grown on Si, as a first step towards the use of dilute-nitrides GaAsPN absorbers displaying the required1.7 eV bandgap. In particular, we have studied GaP n-i-p photodiodes grown on silicon substrate, with two kinds of electrical contacts: top-top (not sensitive to the GaP/Si interface) one and bottom one (photocurrent through the GaP/Si interface).